Lancaster Environment Centre | Lancaster University

Lie-ins or early bedtimes: Do either affect how grasses perform in solar parks?

Nicole Owston

This thesis is submitted in fulfilment of the requirements for the MSc by research in Plant Sciences at the University of Lancaster.

December 2025

Lie-ins or early bedtimes: Do either affect how grasses perform in solar parks?

Abstract

Agrivoltaics combines solar infrastructure with agriculture. Fixed bifacial, north–south oriented panel rows expose plants to temporally structured morning or afternoon shade. Whether plants benefit from a "lie-in" (morning shade) or an "early bedtime" (afternoon shade) is unknown, despite contrasting physiological demands. A trait-based approach using glasshouse and field experiments investigated whether forage species outcomes differ under temporally structured shade.

Glasshouse experiments characterised photosynthetic induction, hydraulic, stomatal, and leaf structural traits of eight temperate forage species: Timothy (*Phleum pratense*); Cocksfoot (Dactylis glomerata); Meadow fescue (*Festuca pratensis*); Tall fescue (*Festuca arundinacea*); Perennial ryegrass (*Lolium perenne*); Italian ryegrass (*Lolium multiflorum*); Hybrid ryegrass (*Lolium × hybridum*), and White Clover (*Trifolium repens*). Stomatal opening time varied eightfold; stomatal limitation ninefold. Maximum contrasts were between Timothy (fast) and Clover (slow stomata). Principal component analysis explained 80.6% of variation and was dominated by contrasts between grasses and the sole dicot, Clover. When Clover was excluded, stomatal size and density, leaf mass per area (LMA), and leaf hydraulic conductance predicted dynamic performance among grasses.

Field experiments examined four species (Timothy, Clover, Italian ryegrass and Perennial ryegrass) under morning and afternoon shade treatments reducing daily light integrals by c. 26%. Species explained 88% of multivariate trait variation, and treatment effects 4%. Timothy produced 69% more biomass under afternoon shade despite minimal plasticity in leaf traits. Clover showed no biomass gains but high plasticity in LMA.

Jointly, experiments revealed kinetic speed alone did not predict biomass responses: Perennial ryegrass showed fast opening (6.3 min) but no biomass gain, whereas Italian ryegrass achieved +24% despite intermediate kinetics (11.5 min). This first trait-based framework for forage species selection in temperate agrivoltaic systems demonstrates that an 'early bedtime' benefits species whose stomatal kinetics, hydraulic traits, and leaf structure are coordinated for exploiting concentrated morning light, while a 'lie-in' offers no comparable advantage.

Contents List

List of Figures

List of Tables

Acknowledgements

This thesis would not have been possible without the support of several people to whom I owe my thanks:

I am grateful to Amy Bellis, the undergraduate intern, for her meticulous work capturing and measuring the stomatal images. The hours spent on the microscope were invaluable to this research, and I am not sure it would have been possible without her work.

To my supervisor, Dr. Samuel Taylor, for his willingness to provide feedback at the eleventh hour. Your last-minute reviews were much appreciated.

To my husband, Jeremy, thank you for your unwavering support. When my resilience wore thin, and I could do nothing but focus on the work in front of me, you quietly took care of everything else; the 'adulting', the daily tasks, the dog walking, all the things I quite couldn't carry, despite your own challenges and business endeavours. Your support carried me through the more difficult moments. I would be remiss not to acknowledge that this has been one of the more challenging endeavours in my life. But here it is, finished at last, and I am grateful for what it has taught me along the way.

Author's Declaration

I declare that this thesis is my own work and has not been submitted in substantially the same for the award of a higher degree elsewhere and that the word count is 32,523.

The ideas presented in this thesis are my own, as is the writing. However, I wish to be transparent about my use of artificial intelligence and digital tools during the preparation of this work:

- ChatGPT (5.1) and Claude (Opus 4.5) were used to generate summaries of research articles to aid comprehension during the literature review process, to assist with planning the structure of this thesis and to help debug code used in data analysis.
- Typeset.io (SciSpace) was used to summarise and interrogate research papers.
- Grammarly (v1.2.215.1793) was used to assist with sentence structure, grammar and spelling.

In all cases, the tools were used to support the research and writing process. The intellectual content, analysis and interpretation and conclusions presented in this thesis remain entirely my own. All sources have been appropriately cited, and I have verified the accuracy of any AI-generated summaries against the original texts.

1 Introduction

1.1 Grasslands and Global Food Security

Grasslands are one of the largest terrestrial biomes on the planet, covering around 40% of the Earth's land area and supporting around 38% of the human population (Liu et al., 2023). They provide valuable ecosystem services such as carbon sequestration, biodiversity conservation, and climate regulation, whilst also providing resources for livestock production (Bengtsson et al., 2019; Liu et al., 2023). Temperate improved grasslands play a vital role in livestock farming worldwide, with significant percentages of global milk (27%) and beef (23%) coming from grassland-based systems (Sere et al., 1995, cited in Conant et al., 2001).

The global transition toward renewable energy infrastructure is creating competition for land between energy and food production at an unprecedented rate (Dupraz et al., 2011; Kruitwagen et al., 2021). By 2050, the world's population is estimated to reach 10 billion, with demands for food and global energy requirements rising simultaneously (Akbar et al., 2024). Solar photovoltaic (PV) technology and agriculture have comparable land requirements: relatively flat terrain that receives sufficient sunlight, which means that land most suitable for solar installations is often identified as having high agricultural potential (Neesham-McTiernan et al., 2025).

Agrivoltaics, the co-location of solar energy collection with agricultural production, offers a potential solution to this land-use conflict. Goetzberger and Zastrow (1982) first proposed this idea, demonstrating mathematically that elevated solar panels could permit approximately two-thirds of solar radiation to reach underlying crops, suggesting that C_3 species could coexist successfully with solar infrastructure. However, it wasn't until 2011 that Dupraz et al. introduced the Land Equivalent Ratio framework, predicting 35–73% increases in global land productivity through this complementary resource use. Interestingly, Sekiyama and Nagashima (2019) found that under low-density panel configurations, even shade-intolerant crops could perform adequately, with corn biomass increasing

by 4.9% compared to controls. Since then, the global installed agrivoltaic capacity grew from 5 MW to 2.8 GW between 2012 and 2020 (Kumpanalaisatit et al., 2022), whilst Neesham-McTiernan et al. (2025) suggest that 127,087 km² of Great Britain has high spatial suitability for agrivoltaics. Whilst agrivoltaics can potentially increase total land productivity, understanding which species thrive under panel-created shade and the mechanisms underlying their responses remains incomplete.

1.2 The Agrivoltaic Light Environment

The light environment beneath photovoltaic arrays differs fundamentally from natural shade or uniform light reduction. Solar panels create complex spatial and temporal patterns of irradiance that vary with panel configuration, orientation, and diurnal sun angle (Dupraz et al., 2011; Sturchio and Knapp, 2023). The design of PV panels influences the temporal distribution of shade over time: fixed-tilt arrays create fairly static patterns, creating areas of deep shade beneath panels, and sunlit zones between rows; while single-axis tracking systems create dynamic light environments where plants beneath panels receive periods of direct sunlight as panels rotate throughout the day (Sturchio and Knapp, 2023). Beneath fixed-tilt panels, the light availability is significantly heterogeneous across both space and time. During the summer months, inter-row spaces can receive photosynthetic photon flux density (PPFD) values above 450 µmol m^{-2} s^{-1} at solar noon, whereas irradiance is generally reduced to less than 100 µmol m^{-2} s^{-1}, approaching the light compensation point for numerous plant species, during the winter (Dhlamini and Brent, 2025). Beyond light reduction, photovoltaic infrastructure modifies the microclimate in ways that may benefit or inhibit crop function. Modifications in temperature are one of the most consistent findings across studies, although the magnitude varies with latitude. In Mediterranean systems, mean daily soil temperatures beneath panels were reduced by 1–1.2 °C, whilst mean air temperatures were not significantly modified (Marrou et al., 2013b). In contrast, Barron-Gafford et al. (2019) found that panels reduced mean air temperature by 1.9–2.3 °C in drylands. However, in the UK's temperate climate, substantially larger effects on soil temperature have been documented in the summer, with average reductions of

5.2°C and maximum decreases up to 7.6 °C in the daily temperatures compared with open areas. However, air temperature showed no significant difference in daily average, although diurnal variation was less pronounced. By contrast, in the winter months, soil temperatures were up to 1.7 °C cooler in the gap areas compared to areas underneath the panels, which acted as a thermal buffer (Armstrong et al., 2016). In dryland environments, vapour pressure deficit (VPD) is consistently 0.5 ± 0.15 kPa lower beneath arrays (Barron-Gafford et al., 2019), with reduced actual evapotranspiration (10–30% lower) resulting primarily from reduced climatic demand rather than stomatal closure (Marrou et al., 2013a). For plant physiology, this difference is mechanistically important because plants can maintain stomatal conductance while experiencing lower transpirational demand, potentially enabling higher water use efficiency without forgoing carbon gain (Marrou et al., 2013a; 2013b).

Despite the environmental heterogeneity found within agrivoltaic environments, most studies have evaluated crop responses in terms of total shade intensity rather than temporal structure. A meta-analysis of 58 studies found nonlinear relationships between solar radiation reduction (RSR) and crop yield, indicating that most crops can maintain productivity with reductions up to 15% (Laub et al., 2022). Forages were classified as shade-tolerant and maintained 103% of control yield at 20% RSR and 93% at 40% RSR, although with substantial uncertainty (Confidence Interval: 75–117%). In contrast, a 40% RSR reduced the photosynthetic efficiency of maize (C_4), resulting in significant yield losses (45%) (Laub et al., 2022). Cool-season C_3 forages generally perform better under moderate shade than warm-season C_4 species, with American orchard grass (*Dactylis glomerata*) and Tall fescue (*Festuca arundinacea)* maintaining yields at 50% shade due to reduced heat stress and photoinhibition during summer (Lin et al., 1999). Additionally, morphological plasticity allowed lettuce to maintain yields by compensating for reduced light through an increase in specific leaf area (SLA), despite having fewer leaves (Marrou et al., 2013c). Similar plastic responses were observed in grass-Clover mixtures, where shade altered the species composition, with White Clover proportions increasing relative to Perennial ryegrass under reduced light (Weselek et al., 2021).

Agrivoltaic field studies conducted within semi-arid grasslands have hinted at the importance of temporal light dynamics, demonstrating interesting spatial patterns. In a single-axis tracking system, aboveground net primary productivity (ANPP) was consistently highest at eastern panel edges, exceeding the productivity of western edges by 33% (Sturchio et al., 2022). The authors attributed this asymmetry to diurnal timing benefits: plants at eastern edges received morning sun when air temperatures and VPD were low, followed by afternoon shade when conditions become unfavourable for C_3 photosynthesis. Subsequent work confirmed that plants exposed primarily to morning light maintained consistently higher stomatal conductance (115% higher than controls) and leaf water potential throughout the growing season, with the eastern edge microsite consistently the most productive across all management treatments (Sturchio et al., 2024a; 2024b).

These findings suggest that the timing of light exposure may be as important as total light quantity for determining plant productivity. Nevertheless, the temporal structure of shade and whether plants experience morning light followed by afternoon shade, or morning shade followed by afternoon light, has not been scientifically studied, despite fundamentally different physiological demands. Morning periods are characterised by low VPD and maximum stomatal responsiveness (Sturchio et al., 2024b), which may be advantageous for species that can rapidly initiate photosynthesis. Afternoon periods bring high VPD and potential hydraulic stress (Barron-Gafford et al., 2019), which may disadvantage species that cannot quickly close their stomata to conserve water. The limited understanding of how species respond to these features of agrivoltaic configurations inhibits evidence-based design of solar parks to sustain agricultural productivity.

1.3 Photosynthesis Under Fluctuating Light

1.3.1 The Problem of Non-Steady-State Photosynthesis

Plants in natural habitat and agrivoltaic environments experience constant light fluctuations; however, most of our understanding of photosynthesis has been built primarily on steady-state

measurements that assume instantaneous adjustment to light conditions (Kaiser et al., 2018). To accurately predict yield, we need to understand how plants respond to dynamic light. In forest understories, sunflecks have been shown to contribute 20–80% of daily carbon exchange (Pearcy, 1990), while crop canopies experience comparable dynamics as leaves move, clouds pass, and self-shading patterns shift (Kaiser et al., 2018). However, photosynthesis does not respond immediately; when light levels increase after a period of shade, CO_2 assimilation rises gradually over several minutes, a phenomenon termed photosynthetic induction (Tanaka et al., 2019). Consequently, models based on steady-state photosynthesis can therefore overestimate daily carbon gain by 20–30% (Way and Pearcy, 2012). These impacts on plant productivity are significant. In wheat, Taylor and Long (2017) demonstrated that slow induction may cost at least 21% of potential productivity, with calculated losses ranging from 10–40% during light fluctuations (Long et al., 2022). As Kaiser et al. (2018) remark, fluctuating light effectively takes crop photosynthesis on a "rollercoaster ride" where regulatory processes struggle to keep pace with environmental change.

1.3.2 Processes Limiting Photosynthetic Induction

Photosynthetic induction is influenced by a series of processes operating at different timescales (Kaiser et al., 2015; Pearcy, 1990). The fastest involves Ribulose 1,5-bisphosphate (RuBP) regeneration, recovering within seconds as electron transport rates increase (Sassenrath-Cole and Pearcy, 1994). The second limitation involves Rubisco activation via Rubisco activase (Rca), which typically required between 1–10 minutes (Mott and Woodrow, 2000). Species differ in induction speed; for example, tobacco shows faster induction than Arabidopsis or camelina, which has been attributed to Rca regulatory properties (Carmo-Silva and Salvucci, 2013). However, the slowest process is stomatal opening, typically requiring 10–30 minutes or longer, an order of magnitude slower than biochemical responses (Kaiser et al., 2015; Lawson and Vialet-Chabrand, 2019). This temporal hierarchy means slow RuBP regeneration limits until approximately 60 seconds; Rubisco activation dominates until approximately 10 minutes; thereafter, stomatal opening becomes the primary

limitation (Kaiser et al., 2016). This balance can change during induction: in Brassica crops, biochemical limitation was greatest immediately after light increased, while stomatal limitation became more important as carboxylation capacity recovered (Taylor et al., 2020). Additionally, an analysis across 15 species found that forgone assimilation was strongly correlated with stomatal opening time, highlighting stomatal kinetics as the dominant source of interspecific variation in dynamic performance (Deans et al., 2019a).

1.3.3 De-induction and Carbon Costs

When light levels decrease, a temporal asymmetry emerges. Stomatal closure often lags behind biochemical down-regulation, allowing continued water loss when carbon gain is constrained (Vialet-Chabrand et al., 2017). The slow relaxation of non-photochemical quenching (NPQ) represents another carbon cost, with theoretical losses estimated to be between 13–32%, depending on temperature (Zhu et al., 2004). However, accelerating NPQ relaxation has been shown to increase field biomass by approximately 15% in tobacco, demonstrating that alleviating a single dynamic bottleneck can yield substantial productivity gains (Kromdijk et al., 2016). Furthermore, non-steady-state modelling reveals that delayed stomatal opening limits morning assimilation, while delayed closure causes afternoon water loss when carbon gain is constrained by declining light (Liu et al., 2024). Therefore, whether plants experience morning shade versus afternoon shade may have fundamentally different consequences depending on the kinetic traits of the species.

1.3.4 Interspecific Variation in Dynamic Responses

Substantial interspecific variation exists in dynamic responses. Across 15 species, the time constant for stomatal opening ranged from 0.9 minutes in rice to 23 minutes in faba bean, a 25-fold variation, although species with dumbbell-shaped guard cells (grasses) were on average 10 minutes faster than those with elliptical guard cells (dicots) (McAusland et al., 2016). Such variation is not limited to interspecific comparisons; within soybean, induction time constants ranged from 1.2 to 13.8

minutes across 37 genotypes (Soleh et al., 2017; 2016). Model simulations suggest that substituting slow kinetics with fast kinetics would reduce daily carbon loss from 21.2% to 11.5% (Tanaka et al., 2019). In rice, small dense stomata contributed to faster responses, and plants with faster stomatal opening showed higher biomass accumulation (Xiong et al., 2022).

In forage species, research on dynamic responses remains limited. In Cocksfoot (*Dactylis glomerata*), the rate at which stomatal conductance changes was slower than that of photosynthesis both entering shade and during subsequent induction, with time to full induction ranging from 15 minutes after brief shade to 37 minutes after extended shade (Peri et al., 2002a). Although it remains unclear how other temperate forages respond within a temporally shaded environment.

While interspecific and intraspecific variation in photosynthetic induction is documented in major crops, the mechanistic basis for this variation, particularly the roles of stomatal anatomy and hydraulic traits, remains poorly characterised in forage species. Whether kinetic properties predict field performance under temporally structured agrivoltaic shade has also not been studied.

1.4 Stomatal Anatomy and Kinetics

Guard cell morphology differs fundamentally between major plant groups, with consequences for dynamic performance. Stomata occur in two principal forms: kidney-shaped guard cells characteristic of dicots, and dumbbell-shaped guard cells found in grasses (Franks and Farquhar, 2007). These morphologies differ not only in appearance, but also in their mechanical operation. In kidney or elliptical-shaped stomata, guard cell swelling against the surrounding epidermal cells generates the force required to open the pore and it is the mechanical advantage of the epidermis that constrains maximum aperture (Franks and Farquhar, 2007). On the other hand, dumbbell-shaped stomata found in grasses operate through a different mechanism. The guard cells are flanked by specialised subsidiary cells that function as osmotic reservoirs (Franks and Farquhar, 2007; Lawson and Blatt, 2014). When stomata open, osmotically active solutes, principally potassium, chloride, and

malate, shuttle rapidly between guard cells and subsidiary cells in a "see-sawing" of turgor pressure, enabling what Franks and Farquhar (2007) described as "greatly accelerated stomatal opening and closure." Across fifteen species, McAusland et al. (2016) found that the opening speed of dumbbell-shaped stomata was, on average, ten minutes faster in reaching maximum conductance than elliptical stomata, a functional group effect representing a fundamental constraint.

The type of guard cell type combined with the size of the stomata influences the speed of response. Smaller stomata possess greater surface-area-to-volume ratios, which may facilitate rapid ion fluxes (Bertolino et al., 2019; Lawson and Blatt, 2014). Across taxonomically diverse rainforest species, Kardiman and Ræbild (2018) demonstrated that stomatal size correlated negatively with opening speed, with these kinetic differences translating to biomass accumulation. Conversely, Elliott-Kingston et al. (2016) found that the closing rate was not correlated with size across an evolutionarily diverse species (ferns, cycads, conifers, and angiosperms); instead, the timing of species diversification relative to historical atmospheric CO_2 concentrations emerged as a stronger predictor. This apparent contradiction may be understood by considering how size-speed relationships operate differently within versus across guard cell types. McAusland et al. (2016) found that among dumbbell-shaped stomata, size significantly impacted speed, whereas among elliptical stomata, physiological processes were considered more important factors than anatomical features, with the type of photosynthesis (C_3 versus C_4) also deemed as being particularly significant.

The distribution of stomata across leaf surfaces varies substantially among species. Approximately 90% of plant species in some communities are hypostomatous, possessing stomata exclusively on the abaxial surface (Muir, 2015). However, grasses represent an exception, often exhibiting equal or higher stomatal density on the adaxial surface (Wall et al., 2022). Amphistomaty, the presence of stomata on both surfaces, may be advantageous because the distance for CO_2 diffusion between substomatal cavities and chloroplasts is reduced (Drake et al., 2019; Muir, 2015).

Wall et al. (2022) demonstrated that adaxial and abaxial stomata operate semi-independently, with each surface contributing to the total conductance differently, whilst Hõrak (2025) showed that adaxial and abaxial stomata exhibit different light sensitivities, which is mediated by different potassium channel complements, differences that may translate to distinct kinetic properties on each surface.

Stomatal density can change in response to environmental conditions during leaf formation, and is therefore considered a developmentally plastic trait (Casson and Gray, 2008). Additionally, it has been suggested that higher stomatal density may enhance dynamic performance: Sakoda et al. (2020) demonstrated that Arabidopsis lines with higher stomatal densities exhibited faster photosynthetic induction, with a 46.5% increase in density achieving 25.6% higher biomass under fluctuating light. This occurred because species with greater stomatal densities had higher initial conductances under low light, reducing stomatal limitation when irradiance increases (Sakoda et al., 2020). However, it is important to note that stomatal anatomy is determined during early leaf development before expansion is complete, whereas structural traits such as leaf area continue to adjust through differential cell expansion (Carins Murphy et al., 2014; Pantin et al., 2011). Furthermore, unified changes in cell size coordinate functionally linked traits: guard cell length correlates with vein density and hydraulic architecture across diverse taxa (Brodribb et al., 2013), suggesting that anatomical, kinetic, and hydraulic traits may be mechanistically linked.

Whether anatomical traits that predict kinetics in controlled studies translate to performance advantages in temporally heterogeneous field environments remains untested. The grass-dicot divide in guard cell morphology suggests fundamentally different structure-kinetics relationships may exist, but direct comparison within realistic agrivoltaic light environments has not been conducted.

1.5 Hydraulic-Photosynthetic Co-ordination

Leaf hydraulic conductance (K_{leaf}), which measures the efficiency with which water moves from the petiole to sites of evaporation, varies more than 65-fold across species. This variance can be attributed to differences in venation architecture, petiole anatomy, and outside-xylem pathways through living tissues (Sack and Holbrook, 2006). The leaves account for at least 30% of whole-plant hydraulic resistance, positioning leaf hydraulics as a major bottleneck in the plant water transport system (Sack and Holbrook, 2006). This resistance comprises xylem conductance through veins and outside-xylem conductance through bundle sheath and mesophyll cells operating in series (Sack and Scoffoni, 2013).

Across species, K_{leaf} shows strong positive coordination with maximum stomatal conductance (g_{max}) and photosynthetic rates. Across eight species, including tree dicots, ferns and grassy monocots, Brodribb and Jordan (2008) demonstrated that K_{leaf} and g_{max} are strongly linearly correlated ($r^2 = 0.80$), whilst Brodribb et al. (2007) used a quadratic regression and found an even tighter coupling between K_{leaf} and maximum assimilation rates (A_{max}; $r^2 = 0.94$) across 43 taxonomically diverse species. This coordination reflects the sequential positioning of xylem and stomata in the water flow path, and stomatal conductance cannot sustainably exceed what the hydraulic supply supports. Additionally, Brodribb and Jordan (2008) found that the ratio between g_{max} and K_{leaf} determines the sensitivity of stomata to VPD, with species having higher K_{leaf} relative to g_{max} being less responsive to increases in VPD. More generally, it is acknowledged that leaf hydraulic conductance and leaf water potential are recognised as major controls on guard cell turgor responses to VPD changes (Grossiord et al., 2020).

Beyond maintaining steady-state coordination, K_{leaf} adapts to environmental changes dynamically within minutes (Sack and Holbrook, 2006). The intensity and quality of light adjust the K_{leaf} through signal transduction in bundle sheath cells, which act as hydraulic "gatekeepers" (Grunwald et al., 2024). Blue light increases K_{leaf} via phototropin signalling, which increases aquaporin activity in

bundle sheath cells; in the absence of blue light, K_{leaf} can decline by 60–70%. This response to light occurs more rapidly than changes in stomatal conductance, which effectively prepares the leaves hydraulically prior to stomatal opening (Grunwald et al., 2024), which may be important in dynamic light environments.

Temperate forage grasses exhibit distinctive hydraulic strategies. Holloway-Phillips and Brodribb (2011b) demonstrated that *Lolium perenne* (Perennial ryegrass) operates with a "water-spending" strategy characterised by extremely vulnerable xylem (P_{50} at −1 MPa) and a negative hydraulic safety margin of −1.35 MPa. Despite operating beyond their hydraulic safety threshold, these grasses can maintain high assimilation rates until >70% of hydraulic conductivity is lost and recover rapidly upon rewatering. Even closely related forage species show contrasting regulation: *Lolium multiflorum* (Italian ryegrass) has a higher maximum leaf hydraulic conductance (K_{max}) and maintains conservative stomatal control, while *Festuca arundinacea* (Tall fescue) exhibits reduced stomatal sensitivity and accepts greater hydraulic risk (Holloway-Phillips and Brodribb, 2011a).

Emerging evidence directly links hydraulic strategy to stomatal kinetics. Meinzer et al. (2017) found that the time it takes for stomata to open is about five times longer in isohydric plants (those that conserve water) compared to anisohydric plants (which use water more freely), while the activation of photosynthesis in isohydric species can take roughly 14 times longer. Additionally, anisohydric species possessed higher stomatal densities, smaller guard cells and faster kinetics. This coordination along the isohydry-anisohydry continuum, now recognised as a spectrum rather than a dichotomy (Ratzmann et al., 2019) suggests that hydraulic strategy may predict dynamic performance: if anisohydric species open their stomata faster, they should be able to exploit transient high-light periods more effectively.

1.6 Phenotypic Plasticity and Shade Acclimation

Phenotypic plasticity is the ability of a genotype to produce different phenotypes in response to environmental variation and presents a potential mechanism for shade acclimation (Bradshaw, 1965; Stearns, 1989). In a comprehensive meta-analysis of 500 experiments spanning 760 species Poorter et al. (2019) identified that most leaf traits respond to daily light integral (DLI) in a saturating manner, with specific leaf area (SLA) exhibiting a plasticity index of approximately 2.6 and leaf mass per area (LMA) showing corresponding increases with irradiance. Among all traits examined, tillering displayed the highest plasticity index, as the only trait increasing more than linearly with light availability (Poorter et al., 2019). LMA is the combination of leaf thickness and tissue density, which effect photosynthetic capacity in opposing ways: leaf thickness increases the accumulation of photosynthetic proteins, whereas increases in density reduce the allocation of nitrogen to assimilative compounds and increase mesophyll CO_2 transfer resistance (Niinemets, 2001; 2002).

The expression of plasticity is not cost-free. DeWitt et al. (1998) proposed two types of plasticity costs; fitness reductions while producing the same phenotype, and plasticity limits, which is the inability to produce the optimal phenotype. Their framework identifies five costs (maintenance, production, information acquisition, developmental instability, genetic) and four limits (information reliability, lag-time, developmental range, epiphenotype). For example, when plants respond to shade, the lag-time limit is particularly relevant because morphological changes depend on developmental time to detect signals, interpret information, and generate new tissue, a process that can take days to weeks. If conditions shift more rapidly than these changes can occur, the ability to adapt becomes ineffective (DeWitt et al., 1998). Ecological factors further constrain plasticity expression; importantly, the most plastic species in response to light exhibited highest seedling mortality in deep shade (Valladares et al., 2007).

Not all plasticity improves fitness. Ghalambor et al. (2007) emphasised that only adaptive plasticity, responses placing organisms closer to the phenotypic optimum, predictably enhances fitness; non-adaptive plasticity may shift phenotypes further from the optimum. A meta-analysis of 280 species directly tested whether SLA plasticity contributes to shade tolerance finding that plants increased SLA by 55.4% under shade, whereas biomass decreased by 59.9%. Shade tolerance depended on having high SLA from the start, not on adjusting it (Liu et al., 2016). Meanwhile, acclimation to fluctuating light produces characteristic shifts; lightfleck-grown leaves have been shown to exhibit SLA 12% higher than the constant light control, although the maximum photosynthetic capacity was unaffected, while stomatal kinetics changed with acclimation (Morales and Kaiser, 2020). This suggests physiological adjustment matters more than structural change for dynamic performance.

Species differ significantly in their plasticity, and these differences typically exceed treatment effects. According to global meta-analyses, intraspecific trait variation accounts for only 25% of variation within communities and 32% among communities, meaning approximately 70% occurs among species (Funk et al., 2017; Siefert et al., 2015). Shade-tolerant species are generally less plastic compared to light-demanding species, with reduced plasticity appearing to be part of a conservative resource-use strategy (Valladares and Niinemets, 2008). Notable differences have been observed between functional groups: grasses can maintain better relative feed values under shade, whereas legumes show greater resilience in crude protein content, likely reflecting Nitrogen-fixation feedback mechanisms (Pang et al., 2017).

Whether morphological plasticity or kinetic specialisation determines performance under diurnal shade regimes has not been directly studied. Theory predicts that structural plasticity should help plants acclimate to changing light; however, Liu et al. (2016) found that plasticity did not improve biomass under shade. When light changes diurnally and on timescales of minutes to hours,

morphological adjustments may simply be too slow. Therefore, in diurnally shaded environments, fast kinetic responses may matter more than structural traits that take days or weeks to develop.

2 Knowledge Gaps

While theory on induction kinetics, hydraulics, and plasticity is well developed, significant gaps remain in how these processes interact, especially for forage species in bifacial agrivoltaic systems.

Temporal versus intensity effects: Agrivoltaic research has focused on total light reduction rather than diurnal shade timing. Meta-analyses quantify yield responses to shade intensity, forages maintain productivity under moderate shade (Laub et al., 2022); however, the physiological effects of morning versus afternoon shade remain unexplored. Field observations suggest eastern panel edges receiving morning light show higher productivity (Sturchio et al., 2024a; 2022), coinciding with lower VPD (Barron-Gafford et al., 2019; Marrou et al., 2013b). Whether this reflects kinetic advantages, hydraulic supply, or microclimate interactions remains unknown.

Kinetic mechanisms in forages: While interspecific variation in photosynthetic induction is documented, opening time constants ranging from 0.9 to 23 minutes (McAusland et al., 2016), with productivity costs potentially exceeding 21% (Taylor and Long, 2017), the mechanisms in temperate forages remain uncharacterised. Grass stomata possess subsidiary cells enabling rapid turgor "see-sawing" (Franks and Farquhar, 2007), but whether this translates to faster kinetics in temperate forage grasses and compared to Clover has not been directly compared.

Structure-kinetics relationships: Anatomical traits predict kinetics in controlled studies; smaller guard cells should open faster (Kardiman and Ræbild, 2018), but size-speed relationships may differ between guard cell morphologies (Elliott-Kingston et al., 2016; McAusland et al., 2016). Higher stomatal densities are known to accelerate induction speeds (Sakoda et al., 2020), and K_{leaf} coordinates with g_{max} (Brodribb and Jordan, 2008; Sack and Holbrook, 2006), but whether these predictions translate to field performance of temperate forage species under diurnal shade regimes is unknown.

Plasticity versus kinetics: Species exhibiting greater SLA plasticity show worse biomass maintenance (Liu et al., 2016), while shade-tolerant species exhibit lower plasticity (Valladares and Niinemets, 2008) and morphological adjustments may be too slow for diurnal shade patterns (DeWitt et al., 1998), making kinetic traits more important. Whether morphological plasticity or the inherent kinetic properties determine the performance of forage species under temporally structured shade has not been tested.

Field translation: Laboratory trait measurements show only modest correlation with field performance (median $r^2 = 0.26$; Poorter et al., 2016). Whether the kinetic properties obtained within controlled glasshouse experiments predict the performance of temperate forage species under realistic agrivoltaic conditions remains untested.

3 Aims and Hypotheses

3.1 Overall Aim

The overall aim of this thesis is to determine how forage species differ in their structural, hydraulic, and dynamic photosynthetic traits, and how these traits shape their phenotypic responses to diurnal shading under bifacial agrivoltaic conditions.

This aim is addressed through two complementary components: (1) a controlled glasshouse experiment quantifying dynamic photosynthetic responses and leaf traits across eight temperate forage species, and (2) a field shading experiment testing how shade timing influences plasticity and biomass in four species covering the kinetic spectrum identified in the glasshouse.

3.2 Glasshouse Experimental Aims and Hypotheses

- GH1: Quantify interspecific variation in photosynthetic induction and de-induction dynamics across eight temperate forage species.
- GH2: Characterise structural (LMA, stomatal anatomy) and hydraulic (K_{leaf}, ψ_{leaf}) traits.
- GH3: Evaluate whether structural and hydraulic traits explain variation in dynamic gas-exchange performance.
- GH4: Identify coordinated trait syndromes through multivariate analysis.

3.2.1 Hypotheses

- GH H1: During step-changes in irradiance, stomatal conductance will adjust more slowly than biochemical processes, generating transient stomatal limitations. *Rationale:* The three-phase limitation hierarchy places stomatal opening as the slowest process, typically requiring 10–60 minutes compared to seconds for RuBP regeneration (Kaiser et al., 2015; Lawson and Vialet-Chabrand, 2019; Pearcy, 1990).

- GH H2: Forage species will exhibit significant interspecific variation in both the magnitude and rate of gas-exchange adjustments. *Rationale:* Opening time constants range from 0.9 to 23 minutes across species (McAusland et al., 2016), with t_{90} varying more than 18-fold (Deans et al., 2019a).
- GH H3: Interspecific differences in photosynthetic capacity will be more pronounced under high irradiance than low irradiance. *Rationale:* Under low irradiance, photon supply limits assimilation uniformly; under high irradiance, species express greater differences in carboxylation capacity (Jaikumar et al., 2021; Pons and Poorter, 2014).
- GH H4: Structural traits (guard cell length, stomatal density) will correlate with stomatal kinetics, with smaller guard cells associated with faster opening. *Rationale:* Smaller stomata have greater surface-area-to-volume ratios, enabling faster ion fluxes (Kardiman and Ræbild, 2018; Lawson and Blatt, 2014), although this relationship may hold within but not across guard cell types (McAusland et al., 2016).
- GH H5: K_{leaf} will positively correlate with g_{max} and potentially with stomatal kinetics. *Rationale:* K_{leaf} and g_{max} show strong coordination ($r^2 = 0.80$; Brodribb and Jordan, 2008).
- GH H6: Multivariate analysis will identify coordinated trait syndromes defined by species grouping of kinetic, structural, and hydraulic traits. *Rationale:* Global analyses demonstrate trait space is constrained along major axes reflecting fundamental trade-offs (Diaz et al., 2016; Reich, 2014; Wright et al., 2004).

3.3 Field Experimental Aims and Hypotheses

- F1: Determine how shade timing (morning versus afternoon) influences diurnal microclimate.
- F2: Quantify phenotypic plasticity in structural and stomatal traits under contrasting temporal shading regimes.
- F3: Test whether species differ in plasticity magnitude and direction.
- F4: Assess whether shade timing influences final biomass accumulation.

- F5: Evaluate whether glasshouse-characterised kinetics predict field performance.
- Species selection: Four species covering the kinetic spectrum, representing fast and slow stomatal kinetics, contrasting functional groups (grass versus legume), and different structural strategies.

3.3.1 Hypotheses

- F H1: Morning and afternoon shading will create contrasting diurnal profiles for photosynthetically active radiation (PAR), temperature, and VPD. *Rationale:* Panel shade reduces both irradiance and VPD simultaneously; timing determines when plants experience high light with high evaporative demand (Marrou et al., 2013b).
- F H2: Forage species will show phenotypic plasticity in response to shade timing. *Rationale:* Plasticity indices reach 2.6 for LMA and 5.0 for tillering under varying light (Poorter et al., 2019).
- F H3: Species will differ in plasticity magnitude, reflecting different functional strategies. *Rationale:* Shade-tolerant species typically exhibit lower plasticity as part of a conservative resource-use strategy (Nicotra et al., 2010; Valladares and Niinemets, 2008).
- F H4: Structural traits will be more plastic than stomatal anatomical traits, which are developmentally constrained. *Rationale:* Stomatal anatomy is determined during early leaf development and remains fixed thereafter (Carins Murphy et al., 2014; Haworth et al., 2021).
- F H5: Shade timing will alter the final biomass, with effects depending on species identity. *Rationale:* Eastern panel edges receiving morning light produce higher ANPP than western edges (Sturchio et al., 2024a; 2022), suggesting temporal light distribution affects productivity.
- F H6: Species with faster kinetics will show greater biomass benefits from shade regimes preserving morning high-light periods. *Rationale:* Circadian and time-integrated processes cause stomatal responsiveness to decline throughout the day (Suwannarut et al., 2023), while VPD is typically lowest early in the day (Marrou et al., 2013b). Species capable of rapid induction may

therefore be able to exploit morning conditions when both stomatal responsiveness and external conditions remain favourable for gas-exchange.

4 Glasshouse materials and methods

4.1 Plant material and growth conditions

Two consecutive glasshouse experiments were conducted within an environmentally controlled facility at Lancaster University to investigate (i) the kinetics of photosynthetic induction and de-induction and (ii) the structural, hydraulic, and anatomical traits underpinning these dynamic responses in eight forage species (seven grasses and the legume, White Clover; Table 1). Seeds were obtained from Cotswold Grass Seeds Ltd. (Moreton-in-Marsh, UK). The selected species represent common constituents of temperate improved grassland mixtures and reflect the functional diversity typically included in UK solar-compatible sward formulations. Timothy (*Phleum pratense*), Perennial ryegrass (*Lolium perenne*), and White Clover (*Trifolium repens*) are included in Cotswold Seeds "Solar Park Permanent Grassland and Long Term Grazing" mixtures (Cotswold Grass Seeds, 2025b), because of their tolerance of partial shade, while the remaining grasses encompass complementary rooting depths and growth forms used to enhance sward resilience and resource capture (Hopkins and Wilkins, 2006). Together, these species span the major agronomic functional types of UK forage systems and provide a suitable comparative framework for agrivoltaic contexts (Andrew et al., 2021; Mason et al., 2016).

All plants were cultivated in 4 L pots (22 cm depth, 16.5 cm diameter) filled with nutrient-rich Petersfield PPC compost (Petersfield Growing Mediums, Leicester, UK). Sowing rates followed supplier recommendations (kg $acre^{-1}$) converted to grams per square metre (g m^{-2}) and scaled to pot surface area (A = 0.0214 m^2). This maintained agronomically realistic sowing densities among species while ensuring uniform canopy development.

Table 1. Forage grass and Clover species used within the experiment, including sowing rates. Note: Sowing rates based on Cotswold Seeds recommendations. Seeds per 4L pot calculated from g/m² rate.

Common name	Latin name	Cultivar	Sowing rate (kg/acre)	Sowing rate (g/m²)	Seeds per 4L pot (g)
Perennial ryegrass	*Lolium perenne*	Aberbann	14	3.46	0.07
Italian ryegrass	*Lolium multiflorum*	Danergo	14	3.46	0.07
Hybrid ryegrass	*Lolium × hybridum*	Aberedge	14	3.46	0.07
Meadow fescue	*Festuca pratensis*	Pardus	12	2.97	0.06
Tall fescue	*Festuca arundinacea*	Elodie	10	2.47	0.05
Timothy	*Phleum pratense*	Dolina	8	1.98	0.04
Cocksfoot	*Dactylis glomerata*	Donata	8	1.98	0.04
White Clover	*Trifolium repens*	Aberswan	4	2.47	0.02

For the photosynthetic induction experiment, pots were arranged in a randomised complete-block design with six blocks. Each block (0.84 m²) contained one replicate of each species positioned within a 3 × 3 grid of eight pots and one intentionally empty position. The space was included to maintain a regular square grid, thus providing consistent spacing to account for variations in microclimate (Hartung et al., 2019). Additionally, pots were spaced 15 cm apart to minimise shading between individuals and provide a homogenous light environment (Brien et al., 2013). Blocks were sown sequentially in three two-block sets (Blocks 1–2, 3–4, 5–6) at two-week intervals, enabling gas-exchange measurements to be taken in succession while maintaining equivalent plant age within each set. Measurements for each set commenced when plants reached six weeks after sowing and required approximately one week to complete.

Following completion of the gas-exchange measurements, a second experiment was established under identical environmental conditions to quantify hydraulic and anatomical traits. This experiment used the same randomised complete-block layout, block positions, and pot spacing as the photosynthetic induction experiment, ensuring that all measurements were made within the same

spatial configuration. For this phase, pots were sown one block at a time and again measured when plants reached six weeks after sowing, ensuring developmental equivalence between cohorts.

Both experiments were maintained under a 16-hour photoperiod, with daylight supplemented by 400 W Philips SON-T high-pressure sodium lamps controlled by a timer and ambient light sensors. Lamps were programmed to switch on at the start of the photoperiod and switch off when ambient irradiance exceeded 500 W m^{-2}, resuming when irradiance dropped below 450 W m^{-2}. Lamps also switched off when the glasshouse temperature exceeded 30 °C to prevent overheating. When operating, supplementary lighting provided 120 ± 17 W m^{-2} (photosynthetic photon flux density, PPFD ≈ 553 µmol m^{-2} s^{-1}) at canopy height. Continuous light-sensor data showed a realised mean photoperiod of 17.1 ± 1.9 h (n = 177 days). Temperature set-points were 21 °C (day) and 11 °C (night). Realised mean ± SD conditions were 24.1 ± 1.9 °C (day) and 14.3 ± 1.2 °C (night), with relative humidity 39 ± 4% (day) and 46 ± 4% (night). Pots were maintained well-watered throughout the experiment, and yellow sticky boards (Catch-It™) were installed for pest control.

4.2 Leaf gaseous exchange measurements

Gas-exchange measurements were conducted between 09:00 and 15:00 h to minimise circadian influences on photosynthetic capacity (Dodd et al., 2005). During measurement, plants were placed within a temporary light rig that provided a uniform background PPFD of approximately 500 µmol m^{-2} s^{-1} at canopy height, verified using a handheld photosynthetically active radiation (PAR) meter (MQ-200, Apogee Instruments, Logan, UT, USA). The rig comprised four dimmable ASRM-II LED grow lights (Speciality Lighting Holland BV) mounted on a steel frame and enclosed on three sides by highly reflective MCPET M4 panels (Furukawa Electric Europe Ltd). This provided constant environmental illumination to stabilise plant microclimate; the measured leaves acclimated inside the LI-6800 chamber, and all programmed light transitions were generated and controlled by the LI-6800's internal light source (LI-COR, Lincoln, NE, USA).

Leaf net CO_2 assimilation rate (*A*) and stomatal conductance to water vapour (g_{sw}) were quantified using a portable open gas-exchange system (LI-6800F, LI-COR, Lincoln, NE, USA; Bluestem v2.1.11, Scripts v2023.02). Before each measurement series, reference and sample analysers were matched using the system's automated Head Match CO_2/H_2O routine. For Clover, the central leaflet was enclosed within a 2 cm^2 aperture; for grasses, a 6 cm^2 aperture enclosed several parallel blades aligned adaxially upward and secured with silicone tape to prevent overlap (Busch, 2018). The cuvette was filled with leaves to avoid estimating leaf area.

Cuvette conditions were standardised: CO_2 reference, 440 µmol mol^{-1}; air temperature, 25 °C; flow rate, 600 µmol s^{-1}; and relative humidity, 65 ± 3 %, yielding a vapour-pressure deficit of ≈ 1.0 kPa at 25 °C. During the high-light phase, sample CO_2 (Ca) stabilised at ~420 µmol mol^{-1}, effectively matching current atmospheric concentrations (NOAA Global Monitoring Laboratory, 2025).

Leaves were equilibrated at 150 µmol m^{-2} s^{-1} PPFD until both *A* and g_{sw} varied by < 2 % over 5 min, indicating steady state (Long and Bernacchi, 2003). The selected light levels (150 µmol m^{-2} s^{-1} for low light and 1000 µmol m^{-2} s^{-1} for high light) were chosen to simulate realistic irradiance fluctuations encountered beneath bifacial solar arrays. The low-light intensity represents the mean shade level recorded in a mock agrivoltaics experiment in the field (Taylor, 2024, unpublished), while 1000 µmol m^{-2} s^{-1} provided saturating but non-photoinhibitory conditions across species (Kaiser et al., 2017). The programmed light sequence comprised 150 µmol m^{-2} s^{-1} for 15 min, 1000 µmol m^{-2} s^{-1} for 60 min, then 150 µmol m^{-2} s^{-1} for 45 mins, and commenced once steady-state was achieved (typically 30–60 min). Values for *A* and g_{sw} were logged every 30 s throughout.

4.3 Photosynthetic dynamics and stomatal conductance kinetics

4.3.1 Calculation of photosynthetic induction and de-induction time constants

The time constants describing photosynthetic induction and de-induction were derived directly from the observed gas-exchange traces following controlled step changes in irradiance. Although photosynthetic responses are often modelled as first-order exponential functions (Acevedo-Siaca et al., 2020; Kaiser et al., 2015) preliminary fitting of the de-induction data indicated that the recorded data did not consistently conform to this assumption. Consequently, a threshold-based method was adopted, following the empirical framework established by Chazdon and Pearcy (1986).

For each light transition, the instantaneous rate of CO_2 assimilation (A_t) was normalised between its initial and final steady-state values (A_i and A_f, respectively) to calculate the time-dependent induction state (IS_t), representing the fractional progression toward the new steady-state (Equation 1).

Equation 1. Induction-state calculation (Chazdon and Pearcy, 1986).

$$IS_{\mathrm{t}} = \frac{(A_{\mathrm{t}} - A_{\mathrm{i}})}{(A_f - A_{\mathrm{i}})}$$

For the induction phase, A_i represented the mean assimilation rate during the preceding low-light steady state, and A_f represented the mean rate under the subsequent high-light steady state. The time constant $t_{90}(A)$ was defined as the elapsed time from the onset of the light increase (t_o) to the first time point at which $IS_t = 0.9$, corresponding to 90% completion of the transition between the two steady states. The 90% threshold (t_{90}) was selected because it provides a robust descriptor of the speed of induction that captures the physiologically relevant later phases of the transition, which strongly influence realised carbon gain under fluctuating light (Lawson and Vialet-Chabrand, 2019; Way and Pearcy, 2012), and because t_{90} is now routinely used as a comparative metric of induction speed across species (Zhang et al., 2022).

For the de-induction phase (DS_t), the same normalisation approach was applied (Equation 1), with A_i representing the steady-state assimilation under high light and A_f representing the subsequent low-light steady state. Under this formulation, DS_t increased from 0 immediately after the light decrease to 1 once *A* stabilised at the new low-light steady state. All species displayed a brief, reproducible transient undershoot in *A* immediately following the light reduction, where *A* temporarily dropped below A_f before recovering (Figure 1). This undershoot reflects the slower kinetics of stomatal closure relative to the down-regulation of photosynthetic biochemistry, transiently limiting CO_2 supply (Lawson and Vialet-Chabrand, 2019; Vico et al., 2011). The DS_t was therefore initiated from the minimum *A* value following this undershoot, when *A* began its monotonic progression toward A_f. The DS_t constant $t_{90}(A)$ was defined as the elapsed time from this point to the first occurrence of $DS_t = 0.9$, ensuring that the estimated time constant captured the true relaxation dynamics rather than the short-lived physiological transient immediately after the light decrease.

4.3.2 Modelling of stomatal conductance kinetics

Dynamic responses of g_{sw} to irradiance transitions were modelled to quantify the speed of stomatal response. Four models were evaluated following Vialet-Chabrand et al. (2013, 2017), comprising two sigmoidal (Equation 2 and Equation 3) and two exponential (Equation 4 and Equation 5) formulations. The sigmoidal models describe asymmetric responses with explicit lag (λ) and curvature (k) parameters, whereas the exponential models describe monotonic responses governed by a single time constant (τ). All additional definitions used in the calculation of t_{63} (Equation 6 and Equation 7) follow the same Vialet-Chabrand et al. (2017) framework.

Equation 2. Sigmoidal model for induction (low-to-high light)

$$g_s(t) = (G_{max} - G_{min}) \cdot e^{-e^{\left(\frac{\lambda - t}{k_i} + 1\right)}} + G_{min}$$

Equation 3. Sigmoidal model for de-induction (high-to-low light)

$$g_s(t) = (G_{min} - G_{max}) \cdot e^{-e^{\left(\frac{\lambda - t}{k_d} + 1\right)}} + G_{max}$$

Equation 4. Exponential induction model

$$g_s(t) = G_{max} + (G_{min} - G_{max}) \cdot e^{-\frac{t}{\tau_i}}$$

Equation 5. Exponential de-induction model

$$g_s(t) = G_{min} + (G_{max} - G_{min}) \cdot e^{-\frac{t}{\tau_d}}$$

The time required to reach 63% of the total transition (t_{63}) was used as a standardised index of stomatal kinetics. For exponential models, t_{63} is equal to the model time constant τ (Equation 6).

Equation 6. Exponential time constant

$$t_{63} = \tau$$

For sigmoidal models, t_{63} was obtained by numerically solving the normalised form in Equation 7 (Vialet-Chabrand et al., 2017).

Equation 7. Definition of t_{63} for sigmoidal models

$$\frac{g_s(t) - G_{\min}}{G_{\max} - G_{\min}} = 1 - e^{-1} \approx 0.63$$

This framework enabled the extraction of the key dynamic parameters (G_{min}, G_{max} and t_{63}) for subsequent multivariate analysis.

4.3.2.1 *Non-linear model fitting and model selection for stomatal kinetics*

Time-series trajectories of stomatal conductance during induction and de-induction were analysed using a multi-model information-theoretic approach. For each plant and each phase of the light transition, both the single-exponential and Gompertz-type sigmoid models were fit using non-linear least squares with the Levenberg–Marquardt algorithm implemented in the nlsLM function of the minpack.lm package in R (Moré, 1978). Time series of g_{sw} were obtained from LI-6800 measurements following transitions from low to high irradiance (150 → 1000 µmol m^{-2} s^{-1}; induction) and from high to low irradiance (1000 → 150 µmol m^{-2} s^{-1}; de-induction), using the time after the light change (s) as the predictor.

In all fits, parameters were constrained to biologically meaningful values (non-negative conductances and time constants) by setting lower bounds of 0 on the minimum and maximum stomatal conductance (G_{min}, G_{max}), λ, and k/τ. The same biologically plausible starting values (G_{min} = 0.05 mol m^{-2} s^{-1}, G_{max} = 0.4 mol m^{-2} s^{-1}, λ = 20 s, k_i = k_d = 5 s), were supplied to nlsLM to aid convergence and maintain comparability across plants. However, final parameter estimates were free to vary according to each plant-level time series, and a maximum of 500 iterations was allowed for convergence. Fits were only attempted for plant × phase combinations with at least three time points and non-missing g_{sw} values.

For each successful fit: (i) parameter estimates (G_{min}, G_{max}, λ, τ or k_i/k_d), (ii) the root mean square error (RMSE) between observed and predicted g_{sw} (Chai and Draxler, 2014), and (iii) the Akaike information criterion (AIC) and its small-sample correction AICc (Akaike, 1974; Hurvich and Tsai, 1989), were extracted. Although AIC was recorded for completeness, all model selection was based solely on AICc, following recommended information-theoretic practice for small sample sizes (Burnham and Anderson, 2002). For the exponential models, the fitted time constant τ, is the time to achieve 63% of the transition between G_{min} and G_{max} and was therefore taken directly as t_{63}. For the Gompertz-type

sigmoid models, an effective response time t_{63} was approximated as ln(100)·k, which captures the dominant portion of the sigmoidal change from near-initial to near-final conductance (Vialet-Chabrand et al., 2017)

Non-convergent fits or fits that yielded non-finite parameter estimates were flagged as unsuccessful and excluded from subsequent summaries but retained in a fitting log for transparency ("Failed" or "Insufficient data"). Model selection followed an information-theoretic framework (Burnham and Anderson, 2002). Plant-level AICc values were first summarised as species means for each candidate model and phase. Within each species × phase combination, mean AICc then ranked models, and ΔAICc values and corresponding Akaike weights (w_m) were calculated using Equation 8.

Equation 8. ΔAICc and Akaike weights for model selection

$$\Delta AICc_{\mathrm{m}} = AICc_{\mathrm{m}} - \min(AICc)$$

$$w_{\mathrm{m}} = \frac{exp(-0.5 \cdot \Delta AICc_{\mathrm{m}})}{\sum_i exp(-0.5 \cdot \Delta AICc_i)},$$

where *m* indexes the model being evaluated and *i* indexes all candidate models in the set, so that Akaike weights represent the relative support for each model normalised across the full model set. The model with the lowest mean AICc (ΔAICc = 0, highest Akaike weight) was taken as the best-supported description of g_{sw} kinetics for that species and phase. Final stomatal kinetic traits (G_{min}, G_{max}, λ, τ or k, t_{63}, RMSE, AICc) were compiled exclusively from these best-supported models and summarised at the species level as mean ± standard error for integration into the univariate and multivariate analyses described below.

4.4 Steady-state intrinsic water-use efficiency (iWUE)

Steady-state intrinsic water-use efficiency (iWUE) was calculated as A/g_{sw} at the low-light and high-light steady states of the induction–de-induction protocol. These values quantify species-level

carbon–water trade-offs under stable conditions and were incorporated as independent traits in the univariate and multivariate analyses.

4.5 C_i-correction and cumulative CO_2 losses

To quantify the integrated carbon penalties arising during the transient phases of photosynthetic induction and de-induction, assimilation rates were normalised for variation in intercellular CO_2 concentration (C_i) to calculate a C_i-corrected potential assimilation rate, $A^*(t)$. This follows an approach used in earlier induction studies Soleh et al. (2016) and Acevedo-Siaca et al. (2020), in which the measured assimilation rate $A(t)$ is rescaled according to the ratio between a reference steady-state C_i and the instantaneous $C_i(t)$ (Equation 9). Thus, at each time step:

Equation 9. C_i-corrected potential assimilation

$$A^*(t) = \max\left[A(t), A(t) \times \frac{C_{i,\text{steady}}}{C_i(t)}\right],$$

where $A(t)$ is the measured assimilation rate, $C_i(t)$ is the instantaneous intercellular CO_2 concentration, and $C_{i,\,\text{steady}}$ is the steady-state C_i for the relevant light phase, defined as the mean of the final three minutes after <2% stabilisation. The use of the maximum ensures that $A^*(t)$ does not fall below the measured value when short-lived C_i excursions cause the ratio $C_{i,\text{steady}}/C_i(t)$ to exceed unity, this prevents artificial negative limitation values and preserves the interpretation of $A^*(t)$ as the assimilation expected under constant C_i.

Cumulative forgone assimilation was then calculated by integrating the difference between potential (A^*) and realised (A) assimilation over each transition period, following the cumulative-loss framework established by Tomimatsu and Tang (2012) and Acevedo-Siaca et al. (2020) (Equation 10-Equation 13). Forgone assimilation was partitioned into stomatal (F_s) and biochemical (F) components. Stomatal forgone assimilation (F_s) represents CO_2 uptake prevented by incomplete stomatal opening

or delayed closure, while biochemical forgone assimilation (*F*) represents CO_2 uptake prevented by incomplete activation or relaxation of photosynthetic biochemistry (Deans et al., 2019b; Kaiser et al., 2015).

Stomatal forgone assimilation during induction (low to high light, ↑) was calculated using Equation 10.

Equation 10. Forgone assimilation due to stomatal limitation on induction

$$\uparrow F_s = \sum_{induction} max\,(0, A^*(t) - A(t))\Delta t,$$

Stomatal forgone assimilation during de-induction (high to low light, ↓) was computed using Equation 11.

Equation 11. Forgone assimilation due to stomatal limitation during de-induction

$$\downarrow F_s = \sum_{de-induction} max\left(0, A^*(t) - A(t)\right)\Delta t.$$

Biochemical forgone assimilation (*F*) was estimated by comparing *A**(t) with the appropriate steady-state potential assimilation for each phase. During induction, *F* reflects the lag in biochemical machinery activation relative to the attained high-light steady state; during de-induction, it reflects the delay in down-regulation towards the low-light steady state (Deans et al., 2019b; Kaiser et al., 2018; Kaiser et al., 2015). For the induction phase, biochemical forgone assimilation was defined relative to the high-light steady-state potential assimilation, $A^*_{\mathrm{ss,HL}}$, as shown in Equation 12.

Equation 12. Forgone assimilation due to biochemical limitation during induction

$$\uparrow F = \sum_{induction} max\left(0, \quad A^{*}_{\mathrm{ss,HL}} - A^{*}(t)\right)\Delta t$$

For the de-induction phase, *F* was defined relative to the low-light steady-state potential assimilation, $A^{*}_{\mathrm{ss},LL}$, as shown in Equation 13.

Equation 13. Forgone assimilation due to biochemical limitation during de-induction

$$\downarrow F = \sum_{induction} max\left(0, \quad A^{*}_{\mathrm{ss,LL}} - A^{*}(t)\right)\Delta t$$

All integrations used the finite-difference time step:

$$\Delta t = 30\ seconds.$$

These integrals yield cumulative forgone assimilation (µmol CO_2 m^{-2}) for each species and light phase, representing the total CO_2 uptake that was prevented by delayed stomatal adjustment or biochemical acclimation. For de-induction, integration began at the start of the programmed light reduction and included the immediate, reproducible transient undershoot in A, ensuring that the full relaxation trajectory was captured.

4.6 Measurement of leaf hydraulic conductance, water potential, leaf area and dry mass

Maximum leaf hydraulic conductance (K_{leaf}) was measured using the evaporative flux method (EFM) described by Sack and Scoffoni (2012). Tillers were harvested in the evening, excised at the soil surface, and immediately placed in water before overnight rehydration in darkness. Measurements were performed between 09:00 and 15:00 hours the following day.

For grasses, the youngest fully expanded leaf was excised under water at the base of the ligule to avoid air entry. A short plastic rod pre-wrapped in Parafilm was submerged; the leaf blade was

wrapped around the rod under water and sealed with additional Parafilm. The rod–leaf assembly was inserted under water into silicone tubing connected to a reservoir of deionised water positioned on an analytical balance (Apollo GX-A series; A&D Company Ltd, Tokyo, Japan). For Clover, the excised petioles were inserted directly into the silicone tubing under water and sealed with Parafilm. Mass loss was logged into a Microsoft Excel worksheet every 10 s with RsKey software (WinCT; A&D Company Ltd, Tokyo, Japan). Leaves were mounted adaxial side up on a wooden frame strung with fishing line, parallel to the reservoir meniscus, and illuminated uniformly with two LI-COR 6400-18 RGB light sources (LI-COR Biosciences, Lincoln, NE, USA) driven by an LI-6400XT console and delivering c. 1,000 µmol m^{-2} s^{-1} PPFD using equal parts red, green and blue; gentle air movement was provided by a desk fan.

Leaves were allowed to transpire for at least 30 min before steady-state was assessed. Steady-state was defined as a coefficient of variation (CV) < 10% in the transpiration signal computed over a 5-minute window (30 consecutive 10-second readings); after this criterion was met, logging continued, and the fifth qualifying value was taken as the steady-state estimate. For each record, the 2-minute mean mass-loss rate (µg s^{-1}) was used and converted to a molar flow (mmol s^{-1}) using the molar mass of water (18.015 g mol^{-1}). This rate, normalised by leaf area, defined the steady-state transpiration rate (E, mmol m^{-2} s^{-1}). This flux represents the rate of water loss through transpiration under steady-state conditions and provides the basis for calculating K_{leaf}.

Leaf temperature was measured using a fine-wire thermocouple at the start and end of each measurement; the mean of the two readings (typical range 23–27 °C) was used as the measurement temperature (T) for viscosity correction. Immediately after measurement, leaves were enclosed in plastic bags that had been pre-exhaled into to halt transpiration and equilibrated for 20 min. Leaf water potential (Ψ_{leaf}) was then measured with a 3000 Series pressure chamber (Soilmoisture Corp, Santa Barbara, CA, USA) equipped with a suitable compression gland. Leaf hydraulic conductance was

calculated using Equation 14 (Sack and Scoffoni, 2012), where *E* is steady-state transpiration (mmol m^{-2} s^{-1}) and $\Delta\psi_{leaf}$ is the difference between the leaf water potential and the water potential at the leaf base. Because the leaf and the water reservoir were maintained at the same vertical height, gravitational effects were negligible, and the water potential at the leaf base was assumed to be 0 MPa. Thus, $\Delta\Psi_{\text{leaf}} = \Psi_{\text{leaf}} - 0$, where Ψ_{leaf} is the leaf water potential measured immediately after sealing the transpiring leaf to halt water loss. This formulation yields conductance values standardised to the driving force for water movement through the leaf.

Equation 14. Leaf hydraulic conductance

$$K_{leaf} = \frac{E}{-\Delta\psi_{leaf}}$$

To standardise leaf hydraulic conductance to 25 °C, the Sack and Scoffoni (2012) viscosity correction (Equation 15) was applied exactly as specified in their EFM protocol, using the mean leaf temperature (T, °C) from the start–end thermocouple readings.

Equation 15: Viscosity correction for leaf hydraulic conductance

$$K_{leaf}(25°C) = \frac{K_{leaf}(T)}{\left(0.88862 \times \left(\frac{1}{10^{\left(1.3272 \times (20-t) - 0.001053 \times (T-20)^2 / (T+105)\right)}}\right)\right)}$$

Leaf area was measured for the same leaf used for the K_{leaf} using an LI-3100C area meter (LI-COR Biosciences, Lincoln, NE, USA). Leaves were oven-dried (70 °C, 48 h) to determine dry mass. Leaf mass per area (LMA) was calculated as dry mass divided by fresh leaf area (g m^{-2}).

4.7 Stomatal anatomy and derived indices

Stomatal traits were measured on the youngest fully expanded, intact leaves of the second experimental cohort. Stomatal impressions were taken from the mid-section of both the adaxial (upper) and abaxial (lower) leaf surfaces using dental putty (President Plus, Coltène/Whaledent Ltd, Burgess Hill, UK). Transparent nail varnish peels were subsequently made from the hardened impressions, mounted on glass microscope slides, and imaged using an Olympus IMT-2 inverted microscope fitted with a GXCAM-U3-5 camera. Stomatal density (SD) was determined at 100× magnification from five non-overlapping fields of view per leaf surface. Guard cell length (GCL) was measured at 400× magnification for a subset of stomata from each surface. All microscopy was calibrated using a stage micrometer (0.01 mm divisions), and all image analysis was performed using ImageJ v1.54g (Schneider et al., 2012).

To capture anatomical determinants of stomatal function, stomatal density (SD) and guard cell length (GCL) were quantified on both the adaxial and abaxial leaf surfaces. Total stomatal density (SD_{tot}) was calculated as the sum of adaxial and abaxial counts, and mean GCL as the arithmetic mean across both surfaces.

In addition to these primary traits, a composite index characterising stomatal distribution between leaf surfaces was derived for this study, adapting the conceptual framework of Muir et al. (2014): the normalised stomatal distribution (NSD) index. Muir et al. (2014) used stomatal ratio (SR = SD_{ad} / SD_{tot}) to quantify stomatal allocation across species. However, for the present study, which aimed to compare species with fundamentally different stomatal distributions (hypostomatous Clover versus amphistomatous grasses) within multivariate analyses, a normalised difference formulation was developed (Equation 16).

Equation 16. Normalised Stomatal Distribution

$$NSD = \frac{SD_{ad} - SD_{ab}}{SD_{ad} + SD_{ab}},$$

where SD_{ad} and SD_{ab} are stomatal densities on the adaxial and abaxial surfaces, respectively. This formulation offers several advantages for comparative analysis: (1) NSD ranges from –1 (entirely abaxial, hypostomatous) to +1 (entirely adaxial, hyperstomatous), with values near 0 indicating approximately equal allocation between surfaces (amphistomatous), centering the amphistomatous condition at zero and facilitating interpretation in principal component analysis; (2) the symmetric scale around zero treats deviations from amphistomy equivalently regardless of direction, making it suitable for detecting variation in stomatal allocation strategy among amphistomatous species; and (3) for Clover, which lacks adaxial stomata (SD_{ad} = 0), NSD = -1 accurately reflects its hypostomatous anatomy without requiring imputation or arbitrary assignments. This composite trait complemented the surface-specific SD and GCL measurements by characterising stomatal deployment strategy as a higher-order functional trait relevant to whole-leaf gas exchange capacity.

4.8 Plant Biomass

At the end of the second glasshouse experiment, all above-ground material from each pot was cut at the soil surface, oven-dried at 70 °C for 72 hours and weighed to determine total biomass.

4.9 Statistical Analysis

4.9.1 Overview and software

All statistical analyses were conducted in R version 4.4.1 (R Core Team, 2024) within the RStudio integrated development environment (Posit Team, 2024). Data manipulation and visualisation were performed using the `tidyverse` suite of packages (Wickham et al., 2019). The analysis was structured into two distinct components to address the hierarchical nature of the data and research

questions: univariate analysis of individual traits, and multivariate analysis of species strategies using the integrated suite of traits.

4.9.2 Univariate analysis

4.9.2.1 *Data screening and assumption checking*

Prior to inference, all trait distributions were inspected for completeness and potential outliers. The assumptions of normality and homogeneity of variances, required for parametric tests like ANOVA, were formally assessed. Normality was evaluated using the Shapiro–Wilk test (Shapiro and Wilk, 1965) applied to each species group and also looked at the overall dataset for each trait across. Homogeneity of variances was assessed using Levene's test (Levene, 1960). As several traits violated one or both of these assumptions, all formal hypothesis testing followed non-parametric approaches.

To complement statistical significance testing and quantify the magnitude of species differences, effect sizes were calculated for all Kruskal-Wallis tests and are reported as eta-squared (η^2), calculated as H/(N-1), where H is the Kruskal-Wallis test statistic, and N is the total sample size. This represents the proportion of variance in each trait explained by species differences. Following traditional benchmarks for ecological data (Fritz et al., 2012), effect sizes were categorised as: negligible ($\eta^2 < 0.01$), small ($\eta^2 \geq 0.01$), medium ($\eta^2 \geq 0.06$), and large ($\eta^2 \geq 0.14$).

4.9.2.2 *Hypothesis testing and post-hoc analysis*

Species differences for each individual trait were tested using the Kruskal–Wallis rank-sum test (Kruskal and Wallis, 1952). For traits where a significant differences among species was detected, post-hoc pairwise comparisons were performed using the Conover–Iman procedure (Conover and Iman, 1979). This test was selected because it is robust to non-normality, heteroscedasticity, and unbalanced group sizes. To control the false discovery rate across the multiple pairwise contrasts for

each trait, Benjamini–Hochberg (BH) correction was applied to the resulting p-values (Benjamini and Hochberg, 1995). The results of these comparisons were summarised using compact letter displays to identify statistically homogeneous groups, generated using the algorithm of Piepho (2004). Descriptive statistics (mean ± SE, median ± IQR, n) were computed for all traits.

4.9.3 Multivariate analysis of greenhouse trait coordination

To analyse the coordination among traits and identify multivariate functional strategies, a combination of principal component analysis (PCA) and permutational multivariate analysis of variance (PERMANOVA) were employed. Analyses were carried out using the packages FactoMineR (Lê et al., 2008) and vegan (Oksanen et al., 2025). Four a priori trait sets were defined to address specific hypotheses.

4.9.3.1 *Trait Sets and Hypotheses*

The four a priori trait sets defined to address the hypotheses outlined in Section 3.2.1 were:

1. Transition magnitude and speed: ↑ΔA, ↑Δg_{sw}, ↑t_{90}(A), ↓t_{90}(A), ↑$t_{63}(g_{sw})$, ↓$t_{63}(g_{sw})$, $t_{63}(g_{sw})$ ↑:↓ (where, up and down arrows indicate induction and de-induction respectively). This set was designed to test the multivariate integration of dynamic traits and identify coordinated physiological strategies.
2. Efficiency vs anatomy, and hydraulics + anatomy: iWUE, CO_2 loss, K_{leaf} ψ_{leaf}, SD_{tot}, GCL, NSD, LMA. These sets were integrated to reveal the architectural basis of photosynthetic strategies and test for relationships between hydraulic anatomy and photosynthetic efficiency.
3. Greenhouse–Field Alignment: leaf area, leaf biomass, plant biomass, LMA, SD_{tot}, abaxial GCL, ↑g_{max}. This set was used to justify species selection for field trials based on the continuum of trait variation observable in the greenhouse.

All analyses were performed on the complete-case individual-plant dataset. Analysis included all available data, with most species having 6 replicates and one species having 5 replicates for some measurements.

4.9.3.2 *Principal component analysis on scaled traits*

For each trait set, a PCA was performed on the correlation matrix to eliminate the influence of differing measurement units (Jolliffe, 2002). We used the PCA function in FactoMineR with scale.unit = TRUE. For each analysis, eigenvalues, the percentage of variance explained, and the loadings of traits on the principal components were extracted. Trait loadings (correlations between traits and PCs) were used to interpret the biological meaning of each axis. The suitability of the data for PCA was confirmed using the Kaiser–Meyer–Olkin (KMO) measure of sampling adequacy and Bartlett's test of sphericity (Bartlett, 1954; Kaiser, 1974).

4.9.3.3 *Testing for multivariate group differences (PERMANOVA)*

Formal tests of multivariate differences among species were conducted using PERMANOVA (Anderson, 2001). For each trait set, a Euclidean distance matrix was constructed from the same z-standardised trait matrix used for PCA. A one-factor PERMANOVA model (species) was fitted using adonis2() in the vegan package. To respect the randomised block design, permutations were constrained within blocks using the strata argument. Each model was run with 9,999 permutations. The pseudo-F statistic, the proportion of variance explained (R^2), and the permutation-based p-value are reported. To ensure that significant PERMANOVA results were due to differences in group centroids (location) and not group dispersions (spread), homogeneity of multivariate dispersions were tested using betadisper() followed by a permutation test (Anderson, 2006).

4.9.3.4 *Pairwise Species Contrasts*

Where the global PERMANOVA was significant, pairwise comparisons were conducted to identify which species pairs drove the overall effect. For each pair, a separate PERMANOVA was run on the z-standardised traits for those two species, with 9,999 permutations. The resulting p-values for all pairs within a trait set were adjusted using the Benjamini–Hochberg false discovery rate procedure. The results are presented as heatmaps of pairwise R^2 values and adjusted p-values.

Together, this framework quantifies (i) the main axes of trait coordination and (ii) the extent of multivariate divergence between species, providing an integrated view of plant functional strategy.

5 Glasshouse Results

5.1 Experimental System Captures Fundamental Kinetic Decoupling

The greenhouse experiment was designed to recreate, under controlled conditions, the light transitions that occur within a bifacial agrivoltaic system, where plants transition between diffuse shade cast by solar panels and full sunlight. The aim was to quantify interspecific differences in how forage species coordinate photosynthesis and stomatal conductance during transient irradiance changes. The hypothesis tested was that physiological regulation, particularly stomatal kinetics, constrains dynamic photosynthetic efficiency and thereby limits potential productivity under fluctuating light.

To test for impacts of light transitions, plants were exposed to a standardised, three-step light sequence: an initial period under low diffuse irradiance (150 µmol m^{-2} s^{-1}; simulating morning shade), a sudden step to high irradiance (1000 µmol m^{-2} s^{-1}; representing unshaded midday sun), and a subsequent return to the original low-light level. Although this protocol does not replicate the full diurnal asymmetry of morning and afternoon shading, it isolates the essential irradiance step changes that drive photosynthetic induction (from shade) and de-induction (when shaded). This controlled sequence provides a mechanistic window into the processes governing carbon–water dynamics within diurnally part-shaded agrivoltaic light environments.

The protocol was applied identically across all replicates (n = 6 plants per species, except n = 5 for Perennial ryegrass), ensuring consistent exposure histories. Gas-exchange traces revealed a pronounced temporal decoupling between assimilation (*A*) and stomatal conductance (g_{sw}) in all species (Figure 1). Following the step increase to high-light, *A* rose steeply and typically reached a new steady state within approximately ten minutes. By contrast, g_{sw} continued to rise for several minutes after photosynthesis had stabilised. During the subsequent return to low light, the pattern reversed: *A* fell almost immediately, often with a brief transient increase before reaching steady state, while g_{sw}

declined more slowly, remaining elevated for an extended period. This created a distinct window of water loss without concomitant carbon gain. The consistent temporal offset between *A* and g_{sw} provides foundational evidence for the overarching hypothesis that stomatal kinetics are the primary constraint on dynamic carbon gain and water use efficiency.

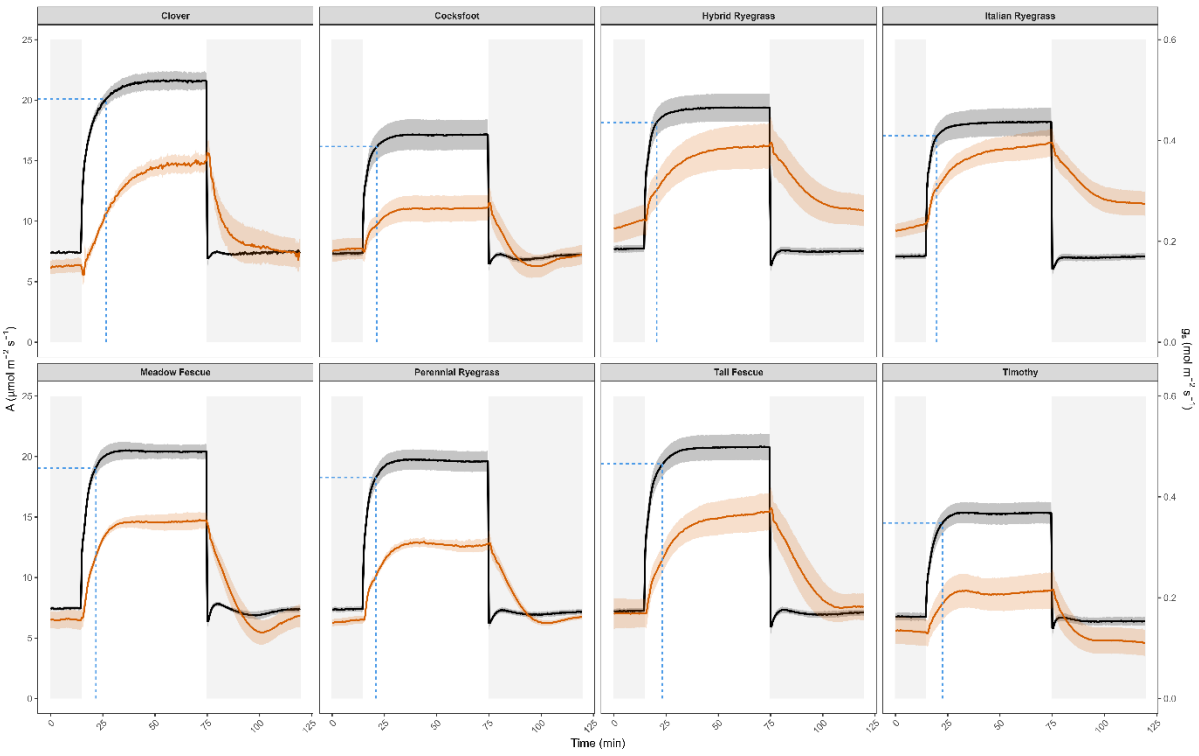

Figure 1. Temporal responses of net photosynthesis and stomatal conductance during controlled light transitions for eight forage species. Net photosynthesis (*A*, black) and stomatal conductance (g_{sw}, red) were recorded at 30-s intervals during a light sequence comprising a 15-min low-light phase (150 µmol m^{-2} s^{-1}), a 60-min high-light phase (1000 µmol m^{-2} s^{-1}), and a 45-min return to low light. Grey shading indicates low-light periods. The blue dashed crosshair marks the modelled photosynthetic induction time constant $T_{90}(A)$, defined as the time at which the normalised induction state ($I_t = (A_t - A_i)/(Af - A_i)$) reached 0.9, corresponding to 90 % completion of the transition to the high-light steady state. Lines show species means with shaded ribbons representing the standard error (± SE; n = 5–6 biological replicates). The figure illustrates the faster biochemical activation of photosynthesis relative to the slower stomatal adjustment during light induction and de-induction.

5.2 Steady-State Performance Establishes a Clear Species Hierarchy

Before examining response dynamics, steady-state photosynthetic capacity was compared under both light extremes to define the operating range for each species. These steady-state measurements establish a reference framework for testing whether variation in the magnitude of dynamic responses reflects underlying differences in photosynthetic capacity and hydraulic supply.

Steady-state assimilation under high irradiance ($A_{SS,HL}$) differed significantly among species ($H_7 = 18.83$, $p < 0.05$, $\eta^2 = 0.41$; Figure 2A). Values ranged from 15.4 ± 0.9 µmol m^{-2} s^{-1} in Timothy to 21.6 ± 0.7 µmol m^{-2} s^{-1} in Clover. Expressed relative to Timothy, Clover assimilated approximately 40% more CO_2 on a leaf area basis at the photosynthetic steady-state. Post-hoc comparisons revealed that Timothy showed significantly lower $A_{SS,HL}$ than Clover, Meadow fescue, and Tall fescue ($p < 0.05$). The three ryegrass species (Italian, Hybrid, and Perennial) and Cocksfoot formed an intermediate group showing no significant differences from either the high-assimilating or low-assimilating species. Among grasses, the fescues consistently occupied the upper range of photosynthetic capacity, while Timothy defined the conservative lower extreme.

Steady-state assimilation under low irradiance ($A_{SS,LL}$) varied over a much narrower range (6.4–7.5 µmol m^{-2} s^{-1}) than $A_{SS,HL}$, and did not differ significantly among species ($H_7 = 9.16$, $p > 0.05$, $\eta^2 = 0.20$; Figure 2B). Thus, all species converged on a similar photosynthetic baseline in shade but diverged strongly under full sun. This asymmetry suggests that interspecific differentiation primarily arises at high irradiance, consistent with the expectation that species differ most in their ability to exploit transient high-light opportunities while maintaining comparable performance in shade.

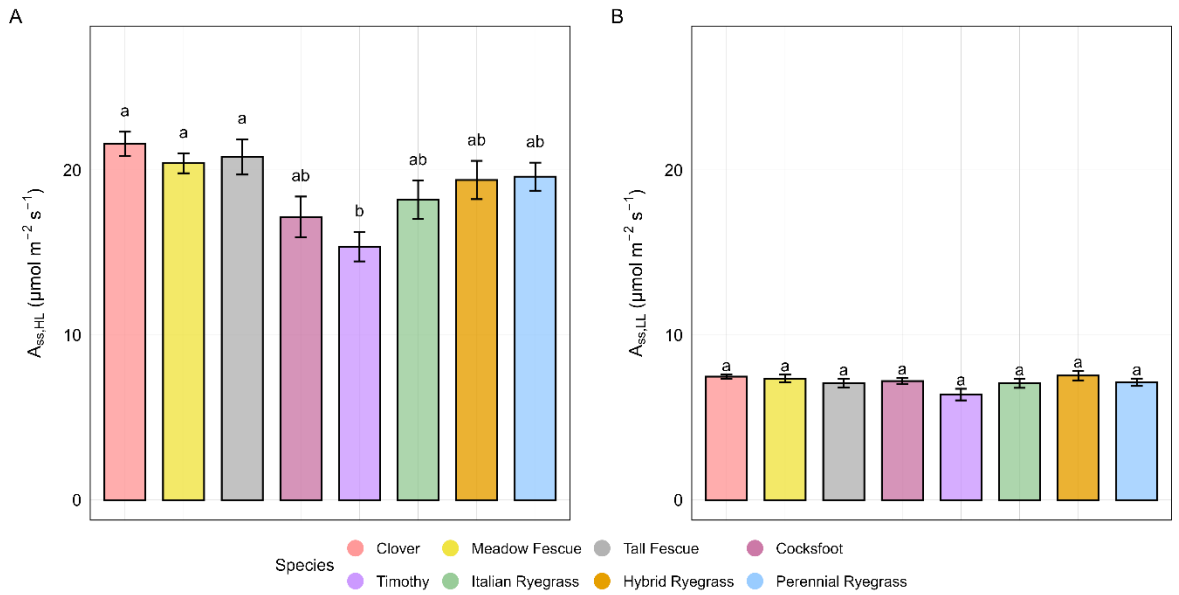

Figure 2. Steady-state photosynthetic capacity of eight forage species under contrasting irradiance conditions. Mean steady-state assimilation rates (*A*) of eight forage species measured under (A) high irradiance ($A_{SS,HL}$, 1000 µmol m^{-2} s^{-1}; $H_7 = 18.83$, $p < 0.05$, $\eta^2 = 0.41$) and (B) low irradiance ($A_{SS,LL}$, 150 µmol m^{-2} s^{-1}; $H_7 = 9.16$, $p > 0.05$, $\eta^2 = 0.20$). Bars represent mean ± standard error (n = 5–6 biological replicates per species). Compact letter displays indicate statistically different groups based on Conover–Iman pairwise comparisons with Benjamini–Hochberg adjustment following a Kruskal–Wallis test ($p < 0.05$); species sharing the same letter were not significantly different.

5.3 Dynamic Responses Reveal a Fundamental Trade-Off Between Speed and Gain

The following analyses test whether species differ in the magnitude and speed of photosynthetic induction and relaxation. First, changes in assimilation and stomatal conductance are quantified. Second, time constants describing induction and de-induction kinetics are compared among species. Third, multivariate analysis evaluates whether magnitude and timing form coordinated response patterns.

Within this framework, the magnitude of change in *A* and g_{sw} represents each species' capacity for adjustment, whereas the temporal parameters (t_{63} and t_{90}) describe the speed with which these adjustments occur.

5.3.1 Magnitude of Induction and the Coordination of A and g_{sw}

The magnitude of photosynthetic induction ($\uparrow \Delta A = A_{SS,HL} - A_{SS,LL}$) differed significantly among species ($H_7 = 22.69$, $p < 0.01$, $\eta^2 = 0.49$; Figure 3A). Clover achieved the largest increase (14.2 ± 0.7 µmol m^{-2} s^{-1}), while Timothy showed the smallest (8.6 ± 0.6 µmol m^{-2} s^{-1}), indicating a 65 % greater induction gain in Clover. Tall fescue and Meadow fescue also achieved significantly larger Δ*A* than Timothy ($p < 0.05$). The fescues, therefore, aligned with Clover at the high-gain end of the spectrum, whereas Timothy and Cocksfoot exhibited more conservative, low-gain behaviour.

The corresponding change in stomatal conductance on induction ($\uparrow \Delta g_{SW}$) exhibited even stronger interspecific differentiation ($H_7 = 33.76$, $p < 0.001$, $\eta^2 = 0.73$; Figure 3B) than was observed for ↑ΔA. Clover increased g_{sw} by 0.2168 ± 0.0199 mol m^{-2} s^{-1}, compared with 0.0851 ± 0.0071 mol m^{-2} s^{-1} in Cocksfoot and 0.0882 ± 0.0102 mol m^{-2} s^{-1} in Timothy. Clover's g_{sw} was therefore 2.4-fold larger than that of the most conservative grasses. Across all replicates, the increases in *A* and g_{sw} upon induction were tightly correlated ($\rho = 0.78$, $p < 0.001$; Figure 3C), indicating that plants with higher stomatal conductance consistently achieved proportionally larger photosynthetic gains. This tight correlation between the magnitudes of change in *A* and g_{sw} demonstrates a coordinated capacity for adjustment of photosynthetic CO_2 assimilation and water use across species.

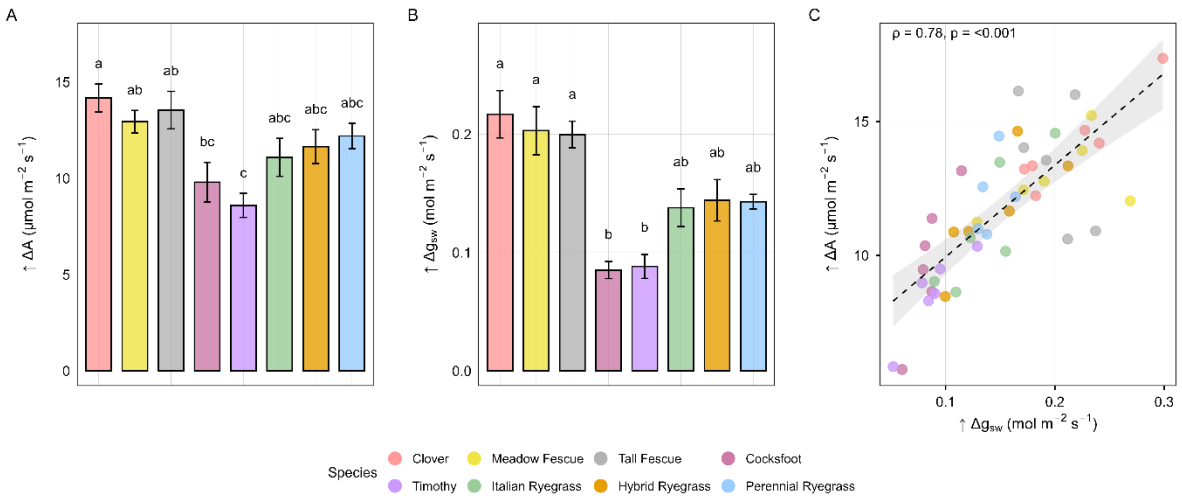

Figure 3. Species differences in the magnitude and coordination of photosynthesis on induction. Mean changes in (A) assimilation rate (↑ΔA) and (B) stomatal conductance (↑Δg_{sw}) following transition from low to high light (150 - 1000 µmol m^{-2} s^{-1}), and (C) their cross-trait relationship across species. Bars represent mean ± standard error (n = 5–6 biological replicates per species). Compact letter displays denote statistically distinct groups after a Kruskal–Wallis analysis with Conover-Iman pairwise comparisons and a Benjamini–Hochberg adjustment. Species differed significantly in both traits (↑ΔA: H_7 = 22.69, $p < 0.01$; ↑Δg_{sw}: H_7 = 33.76, $p < 0.001$), and responses were positively correlated (ρ = 0.78, $p < 0.001$), indicating coordinated increases in photosynthetic and stomatal capacity during induction.

5.3.2 Stomatal Opening Lags Behind Photosynthetic Activation

Stomatal opening times (↑$t_{63}(g_{sw})$) differed almost eightfold among species (H_7 = 27.78, $p < 0.001$, η^2 = 0.60; Figure 4A); Timothy achieved 63% of its final g_{sw} in 5.0 ± 0.5 min, whereas Clover required 40.0 ± 5.4 min. Tall fescue exhibited a slow opening rate similar to Clover, while Italian and Hybrid ryegrass were intermediate, and Cocksfoot and Timothy were consistently fast. Across species, Δg_{sw} was moderately positively related to ↑$t_{63}(g_{sw})$ (ρ = 0.46, $p < 0.01$; Figure 4D), indicating that species with greater stomatal capacity required longer opening times, a capacity–speed trade-off spanning the dicot-monocot divide and grass functional types.

Photosynthetic induction times (↑$t_{90}(A)$) differed significantly among species (H_7 = 28.50, $p < 0.001$, η^2 = 0.62; Figure 4B), although they were universally shorter than ↑$t_{63}(g_{sw})$ for stomata.

Induction was fastest in Italian ryegrass (4.9 ± 0.4 min) and slowest in Clover (11.4 ± 0.7 min). Given that $\uparrow t_{63}(g_{sw})$ were much longer than $\uparrow t_{90}(A)$, and that the two parameters were positively correlated ($\rho = 0.37$, $p < 0.01$; Figure 4C), stomatal kinetics appear to be the primary limitation to photosynthetic induction. However, this correlation was driven primarily by Clover and became non-significant among grasses alone ($\rho = 0.07$, $p > 0.05$; Table 2), indicating that the apparent coordination reflects the dicot–monocot contrast rather than a general coupling mechanism. Photosynthetic induction time ($\uparrow t_{90}(A)$) was not correlated with the magnitude of the assimilation response ($\uparrow \Delta A$; $\rho = 0.24$, $p > 0.05$), nor was there strong evidence for a stomatal capacity–speed trade-off ($\uparrow \Delta g_{sw}$ vs $\uparrow t_{63}(g_{sw})$: $\rho = 0.46$, $p < 0.01$ across all species, weakening to $\rho = 0.32$, $p < 0.05$ among grasses; Table 2). Nevertheless, the primary evidence for stomatal limitation lies in the timescale separation between stomatal and biochemical processes. Direct comparison of $\uparrow t_{63}(g_{sw})$ and $\uparrow t_{90}(A)$ revealed that for most species, stomatal opening remained incomplete well after photosynthetic activation had finished. However, this pattern was not universal. Timothy completed stomatal opening 2.3 minutes before reaching 90% photosynthetic activation, indicating that for this fast-opening species, mesophyll factors such as Rubisco activation, rather than stomatal conductance, represent the kinetic bottleneck. Cocksfoot showed a similar pattern, with stomatal and biochemical processes completing near-simultaneously. These species-specific differences in limitation hierarchy have important implications for the partitioning of forgone assimilation examined in Section 5.4.

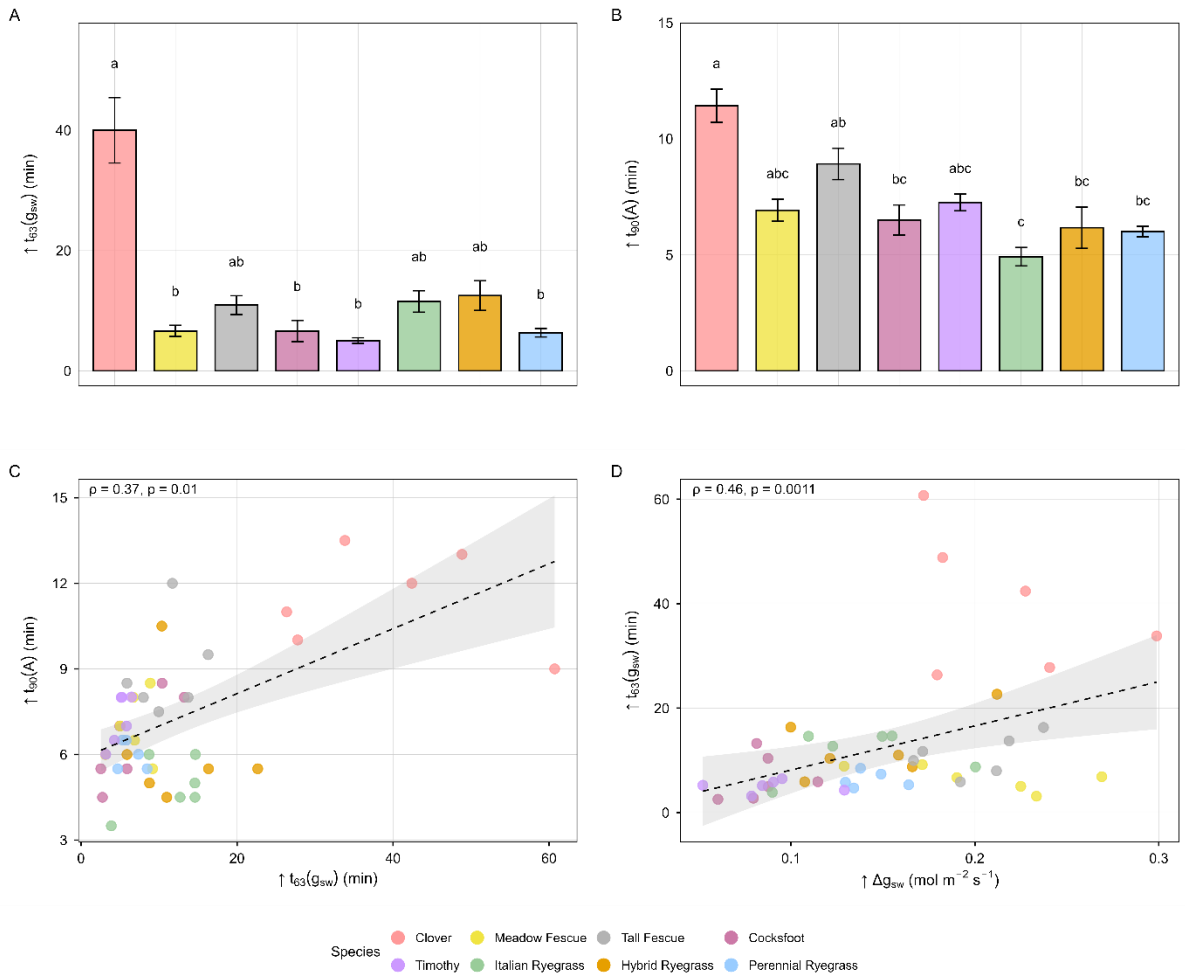

Figure 4. Species differences in the timing and coordination of photosynthetic induction. Mean modelled time constants describing (A) stomatal opening ($\uparrow t_{63}(g_{sw})$; $H_7 = 27.78$, $p < 0.001$, $\eta^2 = 0.60$) and (B) photosynthetic activation ($\uparrow t_{90}(A)$; $H_7 = 19.84$, $p < 0.01$, $\eta^2 = 0.44$) during transition from low to high light (150–1000 µmol m^{-2} s^{-1}). Bars represent mean ± standard error (n = 5–6 biological replicates per species). Compact letter displays indicate statistically distinct groups based on Conover–Iman pairwise comparisons with Benjamini–Hochberg adjustment following a Kruskal–Wallis test ($p < 0.05$). (C) Relationship between $\uparrow t_{90}(A)$ and $\uparrow t_{63}(g_{sw})$, showing moderate positive correlation ($\rho = 0.37$, $p = 0.01$), indicating that species with slower stomatal responses also tended to exhibit slower biochemical activation, though the two processes were not tightly coordinated. (D) Relationship between stomatal opening time ($\uparrow t_{63}(g_{sw})$) and the magnitude of g_{sw} response ($\uparrow \Delta g_{sw}$) on induction, ($\rho = 0.46$, $p = 0.001$).

During light reduction, photosynthetic and stomatal de-induction diverged sharply (Figure 5). Photosynthetic relaxation ($\downarrow t_{90}(A)$) was rapid (2–5 min) and differed significantly among species ($H_7 = 19.61$, $p < 0.01$, $\eta^2 = 0.43$; Figure 5B). It was fastest in Timothy (2.0 ± 0.3 min) and slowest in Italian ryegrass (5.3 ± 0.7 min). Stomatal closure ($\downarrow t_{63}(g_{sw})$) was substantially slower and more variable ($H_7 = 22.32$, $p < 0.01$, $\eta^2 = 0.49$; Figure 5A). Post-hoc analysis found that Italian ryegrass (13.3 ± 1.1 min) was the fastest-closing species, while Tall fescue (34.4 ± 5.0 min) and Hybrid ryegrass (36.7 ± 7.2 min) were significantly slower. The other five species formed a statistically intermediate group (16.7–24.7 min) that did not differ from either extreme. The time constants for stomatal closure and photosynthetic relaxation during de-induction showed no significant relationship ($\rho = 0.28$, $p > 0.05$; Figure 5C), indicating that the two processes were not coordinated. Likewise, stomatal opening and closure were independent ($\rho = 0.16$, $p > 0.05$; Figure 6A). However, sensitivity analysis revealed a significant positive correlation among grasses alone ($\rho = 0.39$, $p < 0.05$; Table 2), indicating coordinated stomatal behaviour within the monocot functional group that is masked by Clover's asymmetric kinetics. The opening:closure ratio ($t_{63}(g_{sw})$ ↑:↓) differed significantly among species ($H_7 = 25.84$, $p < 0.001$; Figure 6B), revealing marked asymmetry in stomatal dynamics, with Clover, Timothy, and Cocksfoot tending towards faster closure relative to opening. A side-by-side comparison of opening and closing times is provided in Figure S1. These asymmetric kinetics highlight that stomatal and photosynthetic adjustments operate on different timescales, defining distinct species strategies for managing gas exchange during light transitions.

Table 2. Pairwise Spearman correlations for induction and de-induction kinetics comparing all eight species versus grasses only (Clover excluded). This analysis examines the robustness of kinetic correlations within the grass group versus those influenced by Clover. Significance: * $p < 0.05$, ** $p < 0.01$, *** $p < 0.001$, NS = not significant. Interpretation categories: Robust = significant in both analyses; Weaker = significant in both but reduced strength in grasses; Clover-driven = significant only with Clover included; Masked by Clover = significant only among grasses (Clover obscures the relationship); No relationship = not significant in either analysis. Trait abbreviations: $\uparrow \Delta A$ = induction magnitude (assimilation); $\uparrow \Delta g_{sw}$ = induction magnitude (conductance); $\uparrow t_{63}(g_{sw})$ = stomatal opening time; $\uparrow t90(A)$ = photosynthetic induction time; $\downarrow F$ = forgone assimilation (biochemical, de-induction); $\downarrow Fs$ = forgone assimilation (stomatal, de-induction); $\downarrow t63(g_{sw})$ = stomatal closing time; $\downarrow t_{90}(A)$ = photosynthetic de-induction time; $t_{63}(g_{sw})$ $\uparrow$:$\downarrow$ ratio = ratio of stomatal opening to closing rate constants.

Trait X	Trait Y	All species ρ	Sig.	Grasses only ρ	Sig.	Interpretation
Induction kinetics						
$\uparrow \Delta A$	$\uparrow \Delta g_{sw}$	0.78	***	0.76	***	Robust
$\uparrow \Delta g_{sw}$	$\uparrow t_{63}(g_{sw})$	0.46	**	0.32	*	Weaker
$\uparrow t_{90}(A)$	$\uparrow t_{63}(g_{sw})$	0.37	*	0.07	NS	Clover-driven
$\uparrow \Delta A$	$\uparrow t_{90}(A)$	0.24	NS	0.04	NS	No relationship
De-induction kinetics						
$\downarrow t_{63}(g_{sw})$	$\downarrow t_{90}(A)$	0.28	NS	0.03	NS	No relationship
Kinetic coordination						
$\uparrow t_{63}(g_{sw})$	$\downarrow t_{63}(g_{sw})$	0.16	NS	0.39	*	Masked by Clover
$t_{63}(g_{sw})$ $\uparrow$:$\downarrow$ ratio	$\uparrow t_{63}(g_{sw})$	−0.30	*	0.05	NS	Clover-driven
Δg_{sw} $\uparrow$:$\downarrow$ ratio	$\uparrow \Delta g_{sw}$	−0.05	NS	0.28	NS	No relationship

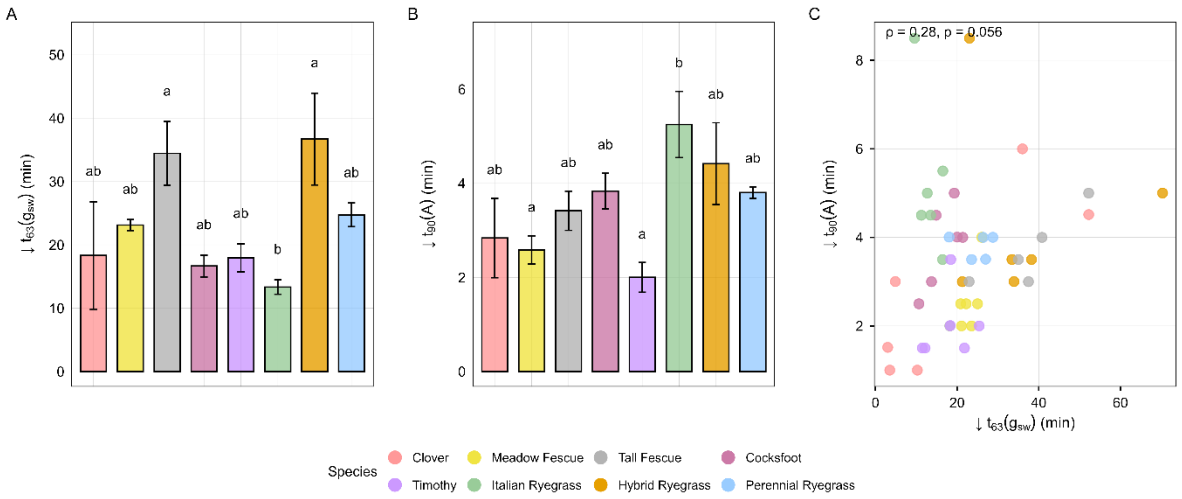

Figure 5. Species differences in the timing and coordination of photosynthetic and stomatal de-induction. Mean modelled time constants describing (A) stomatal closure ($\downarrow t_{63}(g_{sw})$; $H_7 = 22.32$, $p < 0.01$, $\eta^2 = 0.49$), (B) photosynthetic relaxation ($\downarrow t_{90}(A)$; $H_7 = 19.61$, $p < 0.01$, $\eta^2 = 0.43$), and (C) their cross-trait relationship during transition from high to low light (1000 → 150 µmol m^{-2} s^{-1}). Bars represent mean ± 1 standard error (n = 5–6 biological replicates per species). Compact letter displays indicate statistically distinct groups after Kruskal–Wallis analysis with Dunn pairwise tests and Benjamini–Hochberg adjustment ($p < 0.05$). The time constants for stomatal closure and photosynthetic relaxation were not significantly correlated ($\rho = 0.28$, $p > 0.05$), showing that these processes were not coordinated during de-induction.

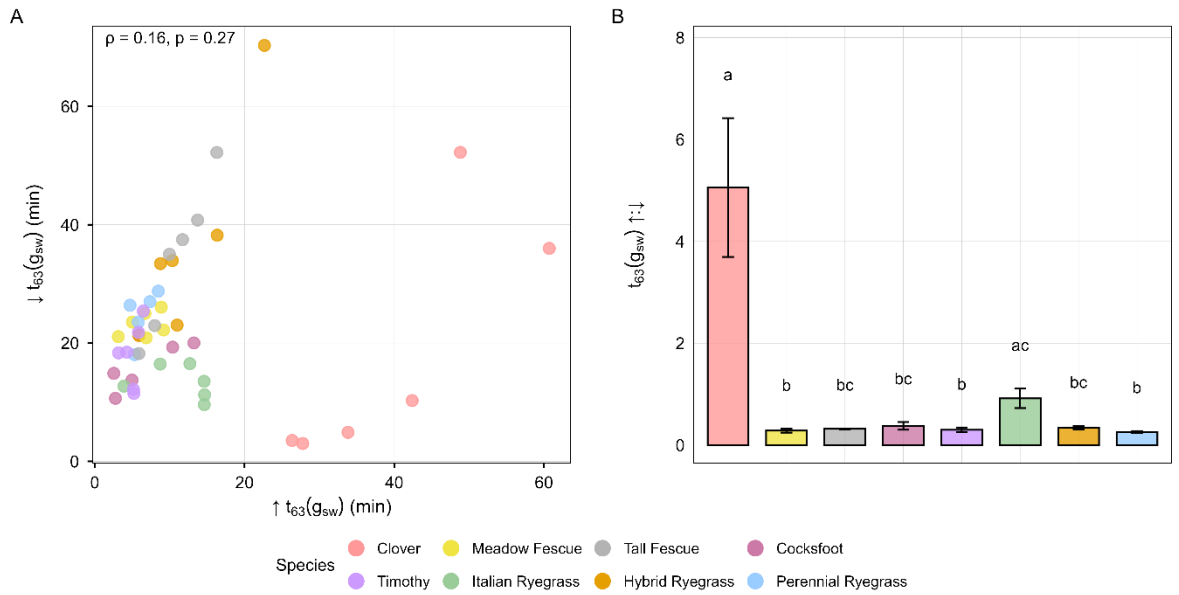

Figure 6. Asymmetry in stomatal opening and closure dynamics across species. (A) Relationship between stomatal opening ($\uparrow t_{63}(g_{sw})$) and closure ($\downarrow t_{63}(g_{sw})$) time constants, and (B) interspecific differences in the opening:closure ratio ($t_{63}(gsw)$ ↑:↓) Bars represent mean ± standard error (n = 5–6 biological replicates per species). Compact letter displays indicate statistically distinct groups based on Conover–Iman pairwise comparisons with Benjamini–Hochberg adjustment following a Kruskal–Wallis test ($p < 0.05$). Opening and closure speeds were not significantly correlated ($\rho = 0.16$, $p > 0.05$), while the $t_{63}(g_{sw})$↑:↓ differed markedly among species ($H_7 = 25.84$, $p < 0.001$), revealing pronounced asymmetry in stomatal kinetics, with Clover tending towards faster closure relative to opening.

5.3.3 Multivariate Integration of Dynamic Traits Identifies Coordinated Physiological Strategies

To determine whether the univariate kinetic traits correspond with higher-order strategies, a principal component analysis (PCA) was performed on the combined set of induction and de-induction magnitudes and timings (↑ΔA, ↑Δg_{sw}, ↑t_{90}(A), ↓t_{90}(A), ↑$t_{63}(g_{sw})$, ↓$t_{63}(g_{sw})$, $t_{63}(g_{sw})$ ↑:↓Figure 7A). Sampling adequacy was moderate (KMO = 0.45) but sufficient (Bartlett's $\chi^2 = 110.46$, $p < 0.001$), and homogeneity of multivariate dispersion was confirmed (PERMDISP $F_{7,39} = 1.41$, $p > 0.05$).

The PCA revealed pronounced multivariate separation, with PC1 and PC2 together explaining 57.1% of total variance. PC1 (35.4%) represented an induction kinetics syndrome: species with slow stomatal opening ($\uparrow t_{63}(g_{sw})$, +0.85) also exhibited slow photosynthetic induction ($\uparrow t_{90}(A)$, +0.81),

large stomatal adjustments (↑Δg_{sw}, −0.57), and prolonged opening relative to closing (t_{63} ↑:↓, −0.73). Trait contributions confirmed that ↑$t_{63}(g_{sw})$ (28.9%), ↑$t_{90}(A)$ (26.7%), and $t_{63}(g_{sw})$ ↑:↓ (21.2%) were the primary drivers of PC1, together accounting for 77% of axis variance, while induction magnitudes contributed less (↑Δg_{sw} = 13.0%, ↑ΔA = 9.4%). PC2 (21.6%) captured a de-induction kinetics axis, defined primarily by stomatal closing time (↓$t_{63}(g_{sw})$, +0.77) and photosynthetic de-induction time (↓$t_{90}(A)$, +0.72), which together contributed 73% of PC2 variance (Figure 7A).

Species identity explained 52% of the multivariate variation (PERMANOVA $F_{7,39}$ = 5.95, R^2 = 0.52, $p < 0.001$), confirming that the eight forage species possess distinct kinetic strategies rather than differing in isolated traits. Clover occupied the positive extreme of PC1 (mean = +3.66, range +3.33 to +4.48), separated from all grasses by more than three standard deviations, reflecting its combination of slow stomatal opening, slow photosynthetic induction, and large stomatal adjustment capacity. The grasses clustered in the negative-to-neutral region of PC1 (means −0.93 to +0.31), consistent with faster induction kinetics and smaller adjustments. Within this cluster, Tall fescue showed the highest PC1 scores among grasses (mean = +0.31), indicating relatively slower induction, while Perennial ryegrass (−0.93), Timothy (−0.81), and Cocksfoot (−0.81) exhibited the fastest responses. PC2 further discriminated species by relaxation behaviour: Hybrid ryegrass showed the highest scores (mean = +1.12), indicating slow stomatal closure, while Timothy exhibited the lowest (mean = −1.23), indicating rapid closure.

Pairwise PERMANOVA confirmed that the primary axis of differentiation was between Clover and all grass species (R^2 = 0.40–0.50, $p < 0.01$; Figure 7B). Within grasses, Italian ryegrass showed the strongest differentiation, differing significantly from all other grasses (R^2 = 0.37–0.44, $p < 0.01$), while Tall fescue and Timothy represented opposing ends of the grass kinetic spectrum (R^2 = 0.38, $p < 0.01$). Several grass pairings showed non-significant differentiation (e.g., Cocksfoot vs Timothy, R^2 = 0.13, $p > 0.05$), indicating overlapping multivariate strategies among some species.

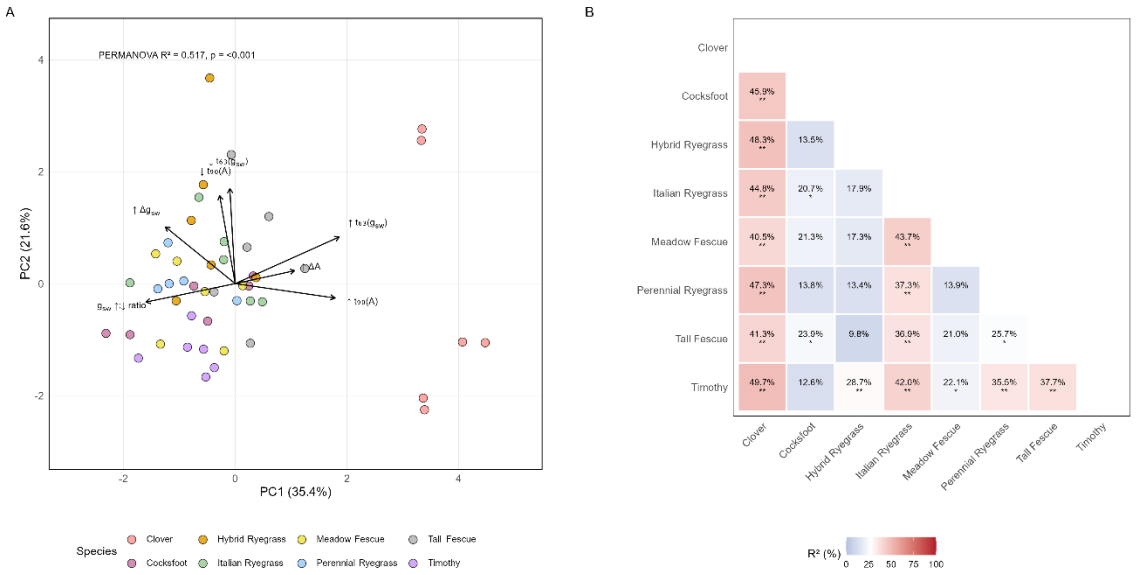

Figure 7. Principal component and pairwise analyses of coordination in gas exchange kinetics across species. (A) Principal component analysis (PCA) summarises seven kinetic traits that describe the magnitude and timing of photosynthetic and stomatal adjustments (↑Δ*A*, ↑Δg_{sw}, ↑t_{90}(*A*), ↓t_{90}(*A*), ↑t_{63}(g_{sw}), ↓t_{63}(g_{sw}), and the t_{63}(g_{sw}) ↑:↓). The first two components together explained 57.1% of the total variance (PC1 = 35.4%, PC2 = 21.6%), representing the induction and de-induction dimensions, respectively. Species differed significantly in multivariate trait space (PERMANOVA $F_{7,39}$ = 5.95, R^2 = 0.52, $p < 0.001$) with homogeneous dispersion (PERMDISP $F_{7,39}$ = 1.41, $p > 0.05$). (B) Pairwise PERMANOVA heatmap showing interspecific Euclidean distances (R^2 %), where darker red cells indicate greater dissimilarity. Pairwise PERMANOVA p-values were adjusted for multiple comparisons using the Benjamini–Hochberg false discovery rate (FDR) procedure. Together, these analyses reveal a coordinated multivariate gradient defined primarily by induction kinetics, with Clover exhibiting slow stomatal and photosynthetic responses at one extreme and Timothy and Cocksfoot exhibiting fast responses at the other.

5.4 Stomatal Kinetics Are the Dominant Constraint on Transient Carbon Gain

To estimate the transient carbon cost during light increase and decrease for each species the forgone CO_2 (µmol m^{-2}) relative to C_i-corrected potential assimilation (*A**) was partitioned into stomatal and biochemical components. These metrics capture the impact of transient inefficiency and allow direct comparison of diffusional versus biochemical constraints across species.

During induction, forgone assimilation due to stomatal limitation during induction (↑F_s) exhibited the largest absolute differences among species and was a significant component of transient

photosynthetic inefficiency (H_7 = 31.09, $p < 0.001$, $\eta^2 = 0.68$; Figure 8A). Clover incurred the greatest F_s (3,238 ± 263 µmol m^{-2}), whereas Cocksfoot lost only 349 ± 142 µmol m^{-2}, representing more than a ninefold difference between the species incurring the greatest and smallest transient carbon costs. Tall fescue exhibited losses comparable to Clover, while Timothy and Cocksfoot experienced the smallest penalties.

Across species, F_s on induction ($\uparrow F_s$) was closely associated with both the time to 63% stomatal opening ($\uparrow t_{63}(g_{sw})$; $\rho = 0.77$, $p < 0.001$; Figure 8B) and the change in stomatal conductance between light and shade (Δg_{sw}; $\rho = 0.76$, $p < 0.001$), confirming that slow and extensive stomatal responses directly amplified the transient carbon cost. Both correlations remained significant when Clover was excluded ($\rho = 0.65$ and $\rho = 0.72$, respectively;), confirming that these relationships are robust within grasses and not solely driven by the Clover outlier. Species with slower and larger stomatal adjustments incurred proportionally greater transient inefficiency, identifying stomatal dynamics as the principal driver of interspecific variation in transient carbon cost during induction.

Although $\uparrow F_s$ explained the majority of interspecific variation in forgone assimilation during induction ($\eta^2 = 0.68$), the relative contribution of stomatal versus biochemical limitation differed among species (Table 3). For Clover and Tall fescue, stomatal costs exceeded biochemical costs by 1.5–4.5 fold, consistent with their slow stomatal opening constraining carbon gain. By contrast, Timothy and Cocksfoot exhibited the opposite pattern: biochemical limitation exceeded stomatal limitation by 2.7–3.0 fold. For these fast-opening species, stomata reached their operating conductance before non-stomatal processes (including Rubisco activation and mesophyll conductance), inverting the typical limitation hierarchy. This reveals that while stomatal kinetics explain most of the interspecific variation in transient carbon costs, the within-species bottleneck depends on position along the kinetic spectrum.

Table 3. Partitioning of forgone assimilation during induction (↑) and deinduction (↓) into stomatal (↑F_s) and biochemical (↑F) components. Values are mean ± SE (µmol m^{-2}; n = 5–6). The ratio indicates the relative contribution of each limitation type; values >1 indicate stomatal dominance, values <1 indicate biochemical dominance. Species are ordered by ratio to illustrate the spectrum from biochemical-limited (Timothy, Cocksfoot) to stomatal-limited (Clover).

Species	Induction				De-induction			
	↑F_s	↑F	↑F_s:↑F	Primary	↓F_s	↓F	↓F_s:↓F	Primary
Cocksfoot	349 ± 142	1035 ± 111	0.34	Biochemical	313 ± 119	411 ± 39	0.76	Biochemical
Timothy	440 ± 53	1185 ± 126	0.37	Biochemical	64 ± 11	519 ± 70	0.12	Biochemical
Meadow fescue	879 ± 124	1231 ± 156	0.71	Biochemical	316 ± 87	653 ± 68	0.48	Biochemical
Hybrid RG	791 ± 171	979 ± 156	0.81	Balanced	92 ± 7	498 ± 46	0.18	Biochemical
PRG	775 ± 220	881 ± 112	0.88	Balanced	141 ± 35	527 ± 36	0.27	Biochemical
IRG	800 ± 164	653 ± 62	1.23	Balanced	77 ± 8	431 ± 44	0.18	Biochemical
Tall fescue	1615 ± 180	1111 ± 99	1.45	Stomatal	178 ± 54	625 ± 57	0.28	Biochemical
Clover	3238 ± 263	723 ± 143	4.48	Stomatal	129 ± 32	607 ± 54	0.21	Biochemical
Fold range	**9.3×**	**1.9×**			**4.9×**	**1.6×**		

For ↑F, although smaller in interspecific effect sizes (H_7 = 15.48, $p < 0.05$, η^2 = 0.34; Figure 8C), comparisons still exhibited significant overall species differences, with mean values ranging from approximately 650 µmol m^{-2} in Italian ryegrass to more than 1,200 µmol m^{-2} in Meadow fescue. Despite the apparent separation of species means in the bar plots (Figure 8C), no pairwise differences remained significant after FDR correction. This combination of medium effect size and lack of post-hoc separation suggests that additional sampling to improve statistical power would be needed to establish certainty in whether there are detectable underlying differences among species. There was a weak correlation between ↑F and the time to 90% of the maximum A on induction (↑t_{90}(A); ρ = 0.30, $p < 0.05$; Figure 8D) across all species. However, this relationship strengthened substantially among grasses alone (ρ = 0.58, $p < 0.001$;Table 4), indicating that comparative biochemical kinetics are a stronger predictor of forgone assimilation within the grass functional group, where stomatal limitation is less dominant. Across all species, however, the large stomatal costs incurred by Clover obscured the contribution of biochemical activation to interspecific variation in transient carbon loss.

Table 4. Spearman correlations between forgone assimilation and kinetic parameters for all species (n=8) versus grasses only (Clover excluded). Sensitivity analysis tests whether relationships are robust within grasses or driven by the grass–Clover contrast. Significance: * p < 0.05, ** p < 0.01, *** p < 0.001, NS = not significant. Interpretation: Robust = significant in both analyses; Strengthens in grasses = stronger correlation when Clover is excluded. Abbreviations: ↑Fs, ↓Fs = forgone assimilation (stomatal, induction/de-induction); ↑F, ↓F = forgone assimilation (biochemical, induction/de-induction); ↑t63(g_{sw}), ↓t63(g_{sw}) = stomatal opening/closing time; ↑t90(A), ↓t90(*A*) = photosynthetic induction/de-induction time; ↑Δg_{sw} = conductance magnitude; $A_{SS,HL}$ = steady-state assimilation at high light.

Trait X	Trait Y	All species ρ	Sig.	Grasses only ρ	Sig.	Interpretation
Induction costs						
↑F_s	↑$t_{63}(g_{sw})$	0.77	***	0.65	***	Robust
↑F_s	↑Δg_{sw}	0.76	***	0.72	***	Robust
↑F_s	$A_{SS,HL}$	0.54	***	0.44	**	Robust
↑F	↑t_{90}(A)	0.30	*	0.58	***	Masked - Strengthens
De-induction costs						
↓F	↓t_{90}(A)	−0.47	***	−0.44	**	Robust
↓F_s	↓$t_{63}(g_{sw})$	0.02	NS	0.01	NS	No relationship

During de-induction, patterns of limitation affecting forgone assimilation differed in two important respects. First, both F_s and F decreased in magnitude relative to those identified during induction. Second, F exceeded F_s for most species, but showed smaller differences between species. F_s during de-induction remained significantly different between species ($H_7 = 23.09$, $p < 0.01$, $\eta^2 = 0.50$; Figure 8E). It was lowest in Timothy (63 ± 11 µmol m^{-2}) and highest in Cocksfoot and Meadow fescue (> 300 µmol m^{-2}). By contrast, F during de-induction was moderate, but consistently larger than F_s (approximately 410–650 µmol m^{-2} across species; $H_7 = 15.50$, $p < 0.05$, $\eta^2 = 0.34$; Figure 8F).

The contrast between induction and de-induction limitation patterns was striking (Table 3). During induction, ↑F_s varied 9.3-fold across species (349–3238 µmol m^{-2}), reflecting the strong influence of stomatal kinetics on transient carbon costs. During de-induction, however, ↓F varied only 1.6-fold (411–653 µmol m^{-2}), despite biochemical limitation exceeding stomatal limitation for all species.

For de-induction, similarly to induction, no pairwise contrasts remained significant after FDR correction, and neither F_s nor F were correlated with their corresponding kinetic parameters

($\downarrow t_{63}(g_{sw})$, $\downarrow t_{90}(A)$; $\rho < 0.2$, $p > 0.1$), indicating that interspecific variation in efficiency during de-induction was weakly governed by the dynamics quantified here.

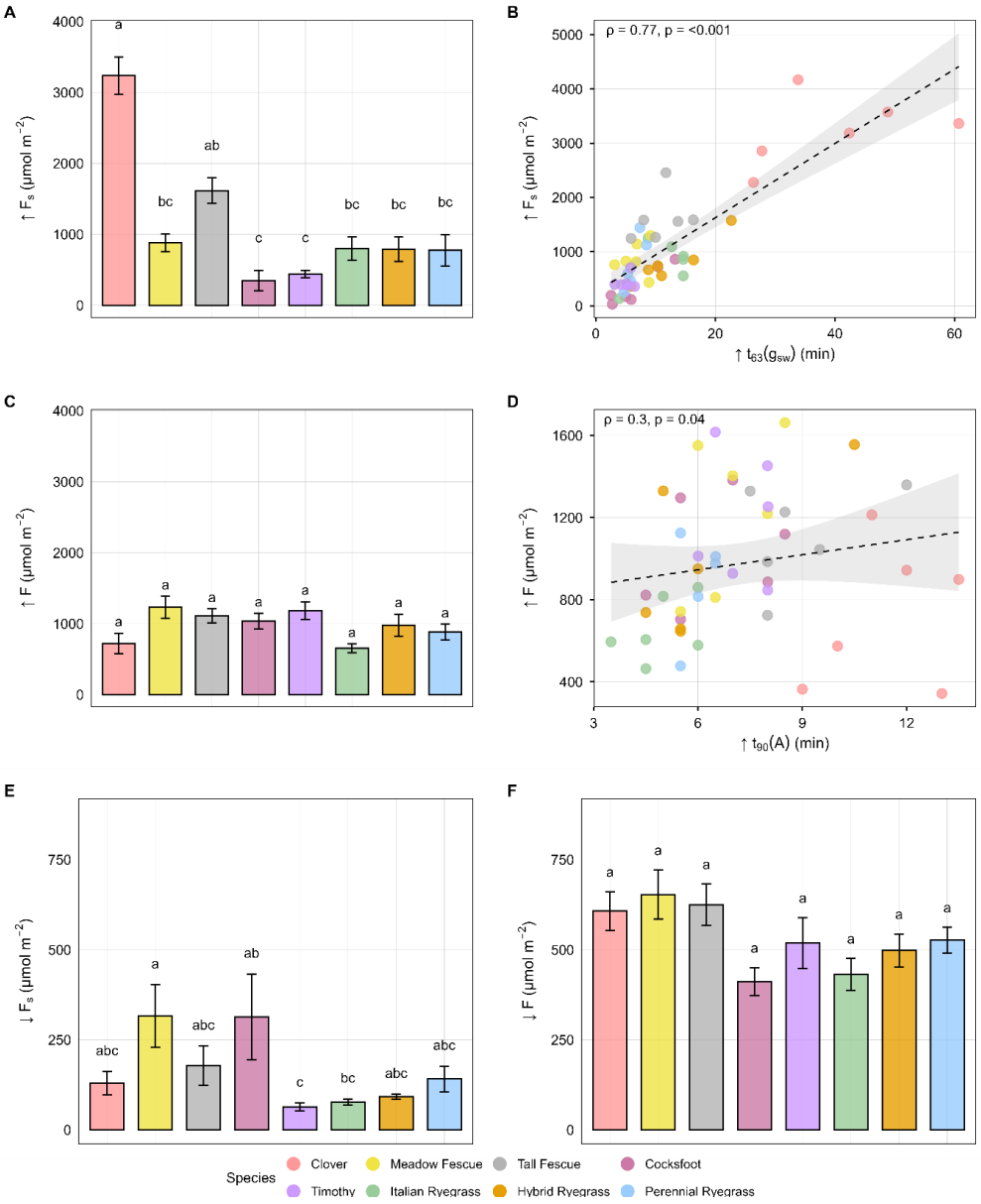

Figure 8. Forgone assimilation and its stomatal and biochemical determinants during light transitions. (A) Forgone assimilation due to stomatal limitation during induction ($\uparrow F_s$; H_7 = 31.09, $p < 0.001$, $\eta^2 = 0.68$); (B) relationship between $\uparrow F_s$ and stomatal opening time ($\uparrow t_{63}(g_{sw})$; $\rho = 0.77$, $p < 0.001$); (C) forgone assimilation due to biochemical limitation during induction ($\uparrow F$; $H_7 = 15.48$, $p < 0.05$, $\eta^2 = 0.34$); (D) relationship between $\uparrow F$ and photosynthetic induction time ($\uparrow t_{90}(A)$; $\rho = 0.30$, $p < 0.05$); (E) forgone assimilation due to stomatal limitation during de-induction ($\downarrow F_s$; $H_7 = 23.09$, $p < 0.01$, $\eta^2 = 0.50$); (F) forgone assimilation due to biochemical limitation during de-induction ($\downarrow F$; $H_7 = 15.50$, $p < 0.05$, $\eta^2 = 0.34$). Bars represent species means ± standard error (n = 5–6 biological replicates per species). Compact letter displays indicate statistically distinct groups based on Kruskal–Wallis analysis with Conover–Iman pairwise comparisons and Benjamini–Hochberg adjustment ($p < 0.05$).

5.5 Structural and Hydraulic Traits Underpin Dynamic Strategies

Species exhibited substantial variation in photosynthetic induction and de-induction kinetics (Figure 1 – Figure 8). This section examines the structural and hydraulic traits that may underpin these dynamic differences. First, interspecific variation in leaf mass per area (LMA), leaf hydraulic conductance (K_{leaf}), leaf water potential (ψ_{leaf}), and stomatal anatomy is quantified. Second, univariate correlations between these static traits and dynamic parameters are evaluated. Third, multivariate analyses test whether structural and hydraulic traits coordinate into integrated syndromes.

5.5.1 Structure–Kinetics Relationships Emerge Within Functional Groups

Six structural and hydraulic traits, leaf mass per area (LMA), leaf hydraulic conductance (K_{leaf}), leaf water potential (ψ_{leaf}), total stomatal density (SD_{tot}), guard cell length (GCL), and normalised stomatal distribution (NSD), provide the anatomical and physiological context for the physiological dynamics described in Sections 5.1 – 5.4. Significant interspecific variation was observed across all traits, confirming distinct leaf architectures among the eight species (Figure 9A–F).

LMA differed significantly among species ($H7 = 44.61$, $p < 0.001$, $\eta^2 = 0.97$; Figure 9A), ranging from 26.9 g m^{-2} in Hybrid ryegrass to 43.9 g m^{-2} in Tall fescue. K_{leaf} varied markedly ($H7 = 41.55$, $p < 0.001$, $\eta^2 = 0.90$; Figure 9B), spanning a fivefold range from 6.7 mmol m^{-2} s^{-1} MPa^{-1} in Tall fescue to 34.7 mmol m^{-2} s^{-1} MPa^{-1} in Clover. ψ_{leaf} showed more moderate but significant variation ($H7 = 19.91$, $p < 0.01$, $\eta^2 = 0.43$; Figure 9C), from −0.18 MPa in Clover to −0.57 MPa in Tall fescue.

Stomatal traits revealed equally strong contrasts. SD_{tot} varied almost fourfold ($H_7 = 41.36$, $p < 0.001$, $\eta^2 = 0.90$; Figure 9D), from approximately 47.5 mm^{-2} in Perennial ryegrass to 199 mm^{-2} in Clover. GCL ranged from 21.9 µm in Clover to 51.0 µm in Italian ryegrass ($H_7 = 42.98$, $p < 0.001$, $\eta^2 = 0.93$; Figure 9E). NSD ranged from −1.0 in the hypostomatous Clover to 0.26–0.87 in the amphistomatous grasses ($H_7 = 41.84$, $p < 0.001$, $\eta^2 = 0.91$; Figure 9F). These patterns reflect the

fundamental morphological divide between the dicot Clover and the monocot grasses, but also reveal notable divergence among grasses in stomatal allocation across leaf surfaces.

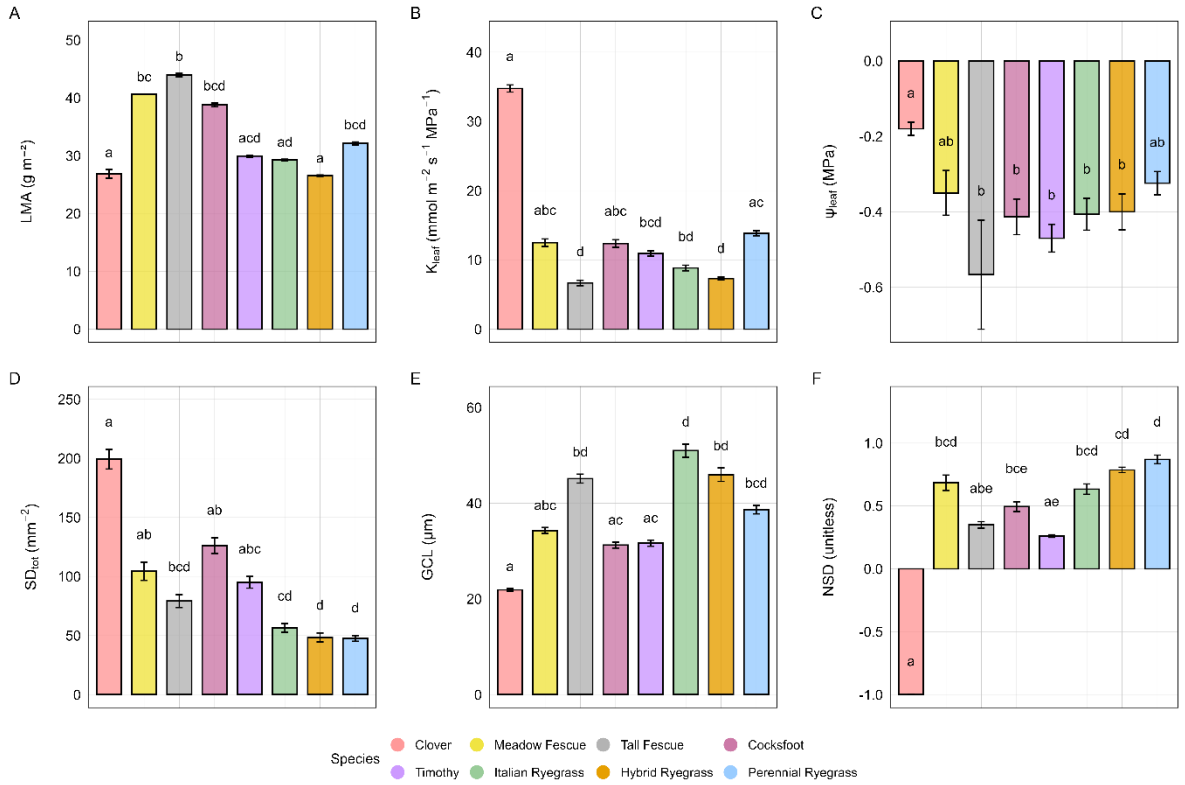

Figure 9. Structural, hydraulic, and stomatal traits defining species-level leaf construction strategies. (A) Leaf mass per area (LMA), (B) leaf hydraulic conductance (K_{leaf}), and (C) leaf water potential (ψ_{leaf}) quantify variation in structural investment and water transport capacity. (D) Total stomatal density (SD_{tot}), (E) guard-cell length (GCL), and (F) normalised stomatal distribution (NSD) describe stomatal deployment across adaxial and abaxial surfaces. Bars represent mean ± SE (n = 5–6 biological replicates per species). Compact letter displays indicate statistically distinct groups following Kruskal–Wallis and Conover-Iman and BH tests ($p < 0.05$).

Having established the presence of substantial interspecific trait variation, it was tested whether these static measurements predict dynamic performance. Pairwise correlations between structural–hydraulic traits and dynamic gas-exchange parameters revealed contrasting patterns depending on whether all species or grasses alone were analysed (Table 5).

Several structural–hydraulic relationships were robust across all species. Guard cell length was strongly negatively correlated with both K_{leaf} ($\rho = -0.75$, $p < 0.001$) and SD_{tot} ($\rho = -0.81$, $p < 0.001$), confirming a fundamental size–number trade-off that operated independently of functional group. Species with smaller, more numerous stomata possessed higher hydraulic conductance, while those with larger, sparser stomata showed lower hydraulic capacity. The correlation between K_{leaf} and SD_{tot} was significant across all species ($\rho = 0.55$, $p < 0.001$). However, it weakened among grasses alone ($\rho = 0.33$, $p < 0.05$), indicating that Clover's extreme trait values partially inflated the apparent hydraulic–anatomical coupling. Similarly, the correlation between K_{leaf} and ψ_{leaf} ($\rho = 0.39$, $p < 0.01$) became non-significant among grasses ($\rho = 0.10$, $p > 0.05$), suggesting that hydraulic–water status coordination is primarily a Clover-driven pattern rather than a general relationship.

In contrast to the structural–hydraulic correlations, relationships between anatomical traits and dynamic gas-exchange parameters were largely non-significant across all species but emerged strongly among grasses alone (Table 5). Stomatal opening time ($\uparrow t_{63}(g_{sw})$) showed no significant correlation with guard cell length ($\rho = 0.03$, $p > 0.05$), leaf hydraulic conductance ($\rho = 0.01$, $p > 0.05$), or total stomatal density ($\rho = 0.07$, $p > 0.05$) when considering Clover and the grasses in combination. However, sensitivity analysis excluding Clover revealed that these relationships were masked by the functional group contrast between monocots and the dicot. Within grasses, stomatal opening time was positively correlated with GCL ($\rho = 0.55$, $p < 0.001$) and negatively correlated with both K_{leaf} ($\rho = -0.49$, $p < 0.01$) and SD_{tot} ($\rho = -0.39$, $p < 0.05$): grasses with larger guard cells, lower hydraulic capacity, and fewer stomata opened more slowly.

Adaxial and abaxial stomatal densities showed contrasting relationships with stomatal kinetics. SD_{ad} was negatively correlated with stomatal opening time across all species ($\rho = -0.63$, $p < 0.001$), indicating that species with more stomata on the upper leaf surface opened faster. This relationship remained significant among grasses ($\rho = -0.45$, $p < 0.01$; Table 5), though it weakened

when the hypostomatous Clover was excluded because its extreme position (zero adaxial stomata combined with very slow opening) acted as a leverage point that inflated the all-species correlation. By contrast, SD_{ab} showed no significant relationship with opening time in either analysis ($\rho = 0.16$ and -0.26, respectively, both $p > 0.05$; Table 5). This asymmetry suggests that stomatal allocation to the adaxial surface specifically confers kinetic advantages, independent of total stomatal investment. Notably, K_{leaf} was positively correlated with adaxial stomatal density among grasses only ($\rho = 0.40$, $p < 0.01$), a relationship entirely masked by the hypostomatous Clover. By contrast, K_{leaf} showed no relationship with NSD in either analysis ($\rho = -0.22$ and $\rho = 0.18$, respectively, both $p > 0.05$), indicating that while hydraulic conductance relates to stomatal density on individual surfaces, it does not predict the distribution of stomata between adaxial and abaxial surfaces.

Stomatal conductance magnitude ($\uparrow \Delta g_{sw}$) was similarly uncorrelated with anatomical traits across all species but showed significant positive correlations with both guard cell length ($\rho = 0.44$, $p < 0.01$) and LMA ($\rho = 0.37$, $p < 0.05$) among grasses. Additionally, LMA was positively correlated with photosynthetic induction time among grasses ($\rho = 0.49$, $p < 0.01$), suggesting that leaves with greater structural investment activated photosynthesis more slowly. These masked relationships indicate that anatomical traits do constrain stomatal and photosynthetic kinetics within functional groups, but the pronounced Clover–grass contrast obscures these finer-scale patterns when all species are pooled.

Together, these analyses reveal a hierarchical structure in trait–function relationships. The fundamental size–number trade-off (GCL vs SD_{tot}) and its coordination with hydraulic capacity (K_{leaf} vs GCL) were robust across functional groups. However, the translation of anatomical variation into dynamic performance differed between dicots and monocots, such that structure–kinetics relationships emerged only when Clover was excluded. Clover, the only dicot in the sample, combined high SD, GCL, and high K_{leaf} with slow stomatal kinetics, a combination distinct from all grass species.

Whether this pattern reflects a broader grass–dicot divide or is specific to Clover cannot be determined from a single dicot species.

Table 5. Pairwise Spearman correlations between structural–hydraulic traits and dynamic gas-exchange parameters. Values show correlation coefficients (ρ) for all species (n = 47) and grasses only (n = 41, excluding Clover). Significance: * p < 0.05, ** p < 0.01, *** p < 0.001, NS = not significant. Interpretation categories: Robust = significant in both analyses with |Δρ| < 0.15; Weaker = significant in both but |Δρ| ≥ 0.15; Clover-driven = significant with all species but NS among grasses; Masked = NS with all species but significant among grasses.

Trait X	Trait Y	All species ρ	Sig.	Grasses ρ	Sig.	Interpretation
Structural–hydraulic coordination						
SD_{tot}	GCL	-0.81	***	-0.71	***	*Robust*
K_{leaf}	GCL	-0.75	***	-0.62	***	*Robust*
K_{leaf}	SD_{tot}	0.55	***	0.33	*	*Weaker*
K_{leaf}	ψ_{leaf}	0.39	**	0.10	NS	*Clover-driven*
K_{leaf}	SD_{ab}	0.37	**	0.06	NS	*Clover-driven*
K_{leaf}	SD_{ad}	-0.07	NS	0.40	**	*Masked*
K_{leaf}	NSD	-0.22	NS	0.18	NS	*No relationship*
Structure–kinetics relationships						
SD_{ad}	$\uparrow t_{63}(g_{sw})$	-0.63	***	-0.45	**	*Weaker*
SD_{ab}	$\uparrow t_{63}(g_{sw})$	0.16	NS	-0.26	NS	*No relationship*
LMA	$\uparrow t_{63}(g_{sw})$	-0.37	*	-0.11	NS	*Clover-driven*
NSD	$\uparrow t_{63}(g_{sw})$	-0.30	*	0.05	NS	*Clover-driven*
$A_{SS,HL}$	$\uparrow t_{63}(g_{sw})$	0.33	*	0.18	NS	*Clover-driven*
GCL	$\uparrow t_{63}(g_{sw})$	0.03	NS	0.55	***	*Masked*
K_{leaf}	$\uparrow t_{63}(g_{sw})$	0.01	NS	-0.49	**	*Masked*
SD_{tot}	$\uparrow t_{63}(g_{sw})$	0.07	NS	-0.39	*	*Masked*
LMA	$\uparrow t_{90}(A)$	0.09	NS	0.49	**	*Masked*
GCL	$\uparrow \Delta g_{sw}$	0.07	NS	0.44	**	*Masked*
LMA	$\uparrow \Delta g_{sw}$	0.07	NS	0.37	*	*Masked*
LMA	$\uparrow \Delta A$	0.06	NS	0.33	*	*Masked*
K_{leaf}	$\uparrow \Delta g_{sw}$	0.04	NS	-0.27	NS	*No relationship*
SD_{tot}	$\uparrow \Delta g_{sw}$	0.07	NS	-0.22	NS	*No relationship*

5.5.2 Multivariate analysis of trait syndromes

To test whether the observed univariate differences in leaf anatomy coordinate as functional syndromes, principal component analyses were performed on two trait sets: a structural–hydraulic set (K_{leaf}, ψ_{leaf}, SD_{tot}, NSD, GCL, LMA) and an expanded efficiency–anatomical set incorporating water-use efficiency and dynamic carbon costs (Section 5.5.4). Sampling adequacy was acceptable for the structural–hydraulic analysis (KMO = 0.74; Bartlett's $\chi^2 = 215.28$, df = 15, $p < 0.001$), which also showed marginally significant heterogeneity (PERMDISP $F_{7,39} = 2.03$, $p = 0.045$); however, PERMANOVA is

robust to moderate heterogeneity when group sizes are similar, and the strong species separation observed (R^2 = 0.86) suggests minimal impact on inference. . Sampling adequacy for the efficiency–anatomical analysis was acceptable (KMO = 0.68; Bartlett's χ^2 = 421.09, df = 55, $p < 0.001$), and homogeneity of multivariate dispersion was confirmed (PERMDISP $p > 0.05$). Summary statistics for both PCAs are provided in Table 6.

Table 6. Summary of principal component analyses examining multivariate trait coordination across eight forage species. *Note:* R^2 and F-statistics from PERMANOVA with 999 permutations. All pairwise species comparisons were significant ($p < 0.01$) in both analyses.

Analysis	Traits	PC1 (%)	PC2 (%)	R^2	F	*p*
Structural–Hydraulic (Figure 10)	6	61.3	19.3	0.86	35.63	< 0.001
Efficiency–Anatomical (Figure 11)	11	39.0	25.1	0.69	12.53	< 0.001

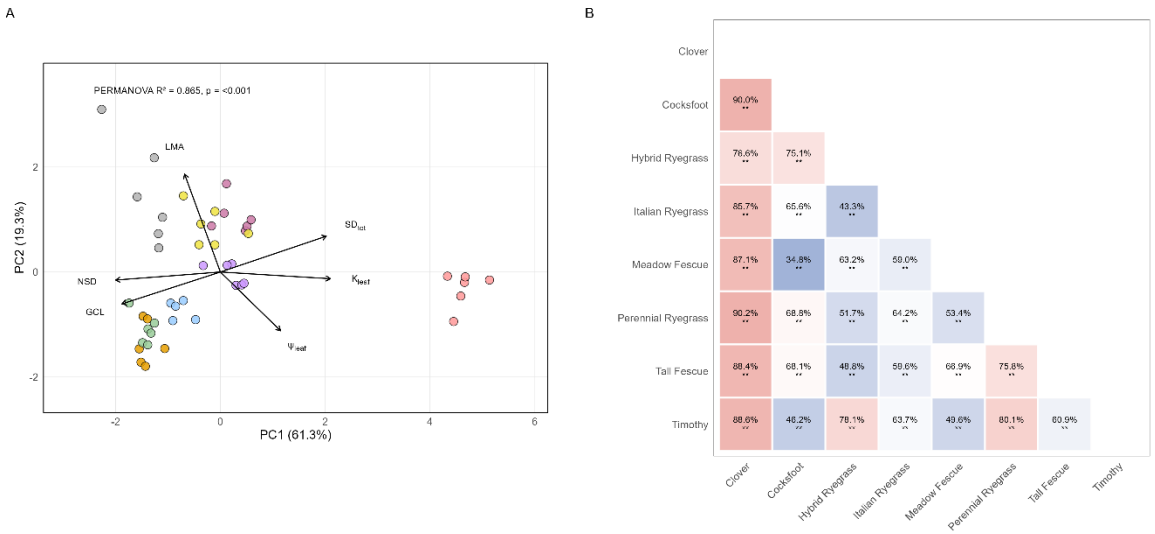

Figure 10. Principal component and pairwise analyses of species multivariate differentiation in structural–hydraulic trait space. (A) Principal component analysis of six foundational traits, with PC1 representing a hydraulic–anatomical syndrome and PC2 capturing leaf construction strategy, explaining 80.6 % of total variance. (B) Corresponding pairwise PERMANOVA heatmap confirming strong species differentiation ($F_{7,39}$ = 35.63, R^2 = 0.86, $p < 0.001$; PERMDISP $F_{7,39}$ = 2.03, $p > 0.05$).

5.5.3 Integration of structural and hydraulic traits

The structural–hydraulic PCA revealed pronounced multivariate separation, with PC1 accounting for 61.3% of variance alone (Figure 10A). This dominant axis represented a hydraulic–anatomical syndrome: species with high leaf hydraulic conductance (K_{leaf}, loading +0.96) also possessed dense stomata (SD_{tot}, +0.92) and less negative water potentials (ψ_{leaf}, +0.52) while exhibiting a hypostomatous distribution (NSD, −0.91) and smaller guard cells (GCL, −0.85). Species with the opposite trait combination, amphistomatous distributions, larger guard cells, and lower hydraulic conductance, occupied the negative end of PC1. Trait contributions confirmed that K_{leaf} (24.8%), SD_{tot} (23.0%), NSD (22.4%), and GCL (19.8%) were the primary drivers of PC1, together accounting for 90% of the axis variance, while ψ_{leaf} (7.4%) and LMA (2.6%) contributed minimally. By contrast, PC2 (19.3%) captured additional variation in leaf construction strategy, reflecting differences in leaf mass per area (LMA, loading +0.85, contribution 62.1%) and water status (ψ_{leaf}, −0.51, 22.3%), with stomatal traits contributing less than 16% combined.

Species identity explained 86% of the multivariate variation (PERMANOVA $p < 0.001$), confirming that the eight forage species possess distinct structural–hydraulic syndromes rather than merely differing in isolated traits. Clover occupied the positive extreme of PC1 (scores +4.3 to +5.1), separated from all grasses by more than four standard deviations, reflecting its combination of high hydraulic conductance, dense stomata, and hypostomatous architecture. The grasses clustered at negative PC1 values but diverged substantially along PC2: Tall fescue showed the highest LMA, Cocksfoot and Meadow fescue were intermediate, while the ryegrasses and Timothy exhibited lower leaf construction costs (Figure 10B). All pairwise species contrasts were significant, with the strongest differentiation between Clover and grasses ($R^2 = 0.77–0.90$) and weaker but still significant contrasts among grass species ($R^2 = 0.35–0.80$).

5.5.4 *Linking Anatomical Syndromes to Dynamic Photosynthetic Strategies*

Having established that the species show different structural–hydraulic syndromes, a key question is whether these differences predict dynamic photosynthetic performance. Specifically, whether species with greater hydraulic investment also incur larger carbon costs during stomatal adjustment. To test this, the PCA was expanded to include steady-state water-use efficiency ($iWUE_{ss,HL}$, $iWUE_{ss,LL}$) and forgone assimilation due to stomatal ($\uparrow F_s$, $\downarrow F_s$) and biochemical ($\uparrow F$, $\downarrow F$) limitations during light transitions (Figure 11A).

The expanded efficiency-anatomy analysis confirmed that species differentiation persists when dynamic traits are included, though the strength of separation was reduced (R^2 = 0.69 vs. 0.86 for anatomy alone; Table 6). The same structural–hydraulic traits dominated PC1 (K_{leaf}, +0.93; SD_{tot}, +0.92; NSD, −0.91; GCL, −0.85), but crucially, forgone assimilation due to stomatal limitation on induction ($\uparrow F_s$) also loaded positively on this axis (+0.72). Trait contributions revealed that K_{leaf} (20.0%), SD_{tot} (19.9%), NSD (19.5%), and GCL (16.8%) remained the primary drivers of PC1, with $\uparrow F_s$ contributing 12.2% of axis variance. This co-loading suggests a mechanistic link: species that invest heavily in hydraulic capacity and stomatal density also incur larger transient carbon penalties when stomata open.

PC2 (25.1%) captured an efficiency–cost axis distinct from the hydraulic gradient, defined by steady-state water-use efficiency at both light levels ($iWUE_{ss,LL}$, +0.79; $iWUE_{ss,HL}$, +0.66) alongside forgone assimilation during stomatal de-induction ($\downarrow F_s$, +0.72) and biochemical limitation during induction ($\uparrow F$, +0.66). Contributions to PC2 were dominated by $iWUE_{ss,LL}$ (22.6%), $\downarrow F_s$ (18.6%), $\uparrow F$ (15.9%), and $iWUE_{ss,HL}$ (15.6%), collectively accounting for 73% of the axis variance. Notably, the two biochemical limitation components loaded on different axes: while $\uparrow F$ aligned with efficiency traits on PC2, $\downarrow F$ contributed minimally to PC1–PC2 but dominated PC3 (37.9% contribution, +0.69 loading).

This pattern indicates that variation in $\downarrow F$ occurred primarily within rather than between species, consistent with the univariate finding that species did not differ significantly in $\downarrow F$ after pairwise correction. Furthermore, $\downarrow F$ showed no correlation with either stomatal kinetics or anatomical–hydraulic traits. This indicates that variation in biochemical deactivation during shade transitions is largely independent of the structural and dynamic traits that shape induction behaviour, representing a third, orthogonal dimension contributing to physiological responses to shade.

Species positions in the combined efficiency–anatomical trait space largely mirrored the anatomical analysis (Figure 11A). Clover remained at the positive extreme of PC1 (+4.4 to +5.3), characterised by high hydraulic investment and correspondingly large stomatal induction costs. Among grasses, Hybrid and Italian ryegrass occupied the most negative PC1 positions (−1.4 to −2.1), reflecting low hydraulic investment and minimal transient losses, while Timothy and Cocksfoot clustered near the origin, indicative of balanced carbon–water strategies. The grasses separated more clearly along PC2, with Meadow fescue and Cocksfoot showing higher water-use efficiency and greater de-induction costs than the ryegrasses. Comparisons between Clover and grasses yielded the highest pairwise dissimilarity (R^2 = 0.54–0.66), while contrasts among grasses ranged from 0.28 to 0.58 (Figure 11B).

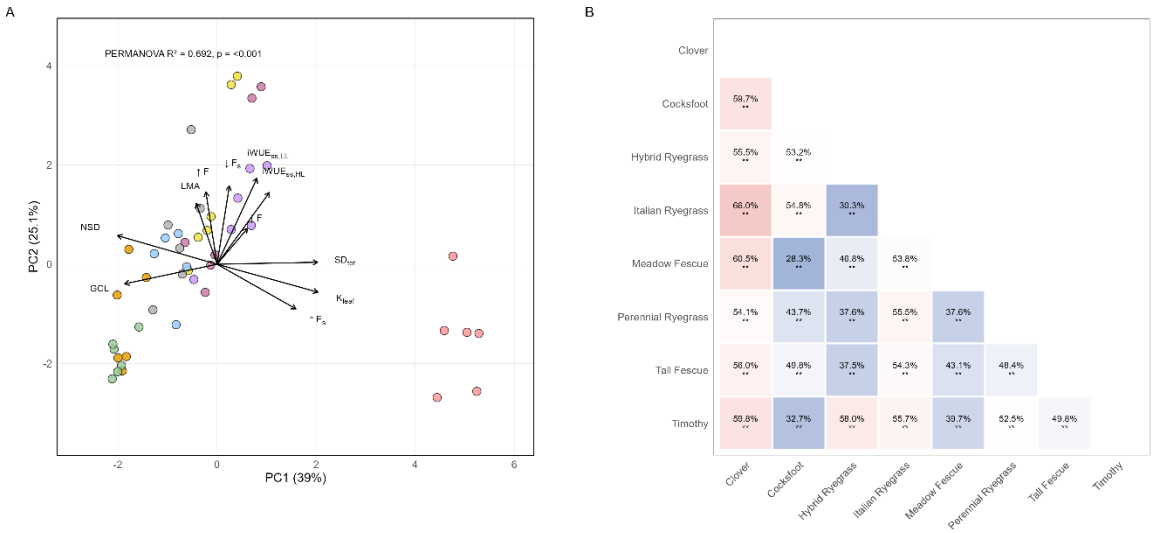

Figure 11. Principal component and pairwise analyses of multivariate strategies in the combined efficiency–anatomical trait space across species. (A) Principal component analysis of eleven traits integrating structural (K_{leaf}, ψ_{leaf}, SD_{tot}, NSD, GCL, LMA), hydraulic, efficiency ($iWUE_{ss,HL}$, $iWUE_{ss,LL}$), and the dynamic cost metrics of forgone assimilation due to stomatal limitations (F_s) and biochemical components (F) associated with induction and de-induction, explaining 69% of the total variance. The positive co-loading of $\uparrow F_s$ with hydraulic traits on PC1 indicates that high anatomical investment incurs large induction costs. (B) Pairwise PERMANOVA heatmap showing significant interspecific separation in the integrated trait space (PERMANOVA $F_{7,39} = 12.53$, $R^2 = 0.69$, $p < 0.001$; PERMDISP $F_{7,39} = 1.82$, $p > 0.05$).

5.6 Greenhouse Trait Strategies Justify Species Selection for Field Trials

To select focal species for field experiments, a separate PCA was performed on structural and productivity traits measurable in both environments (leaf area, leaf and plant biomass, LMA, SD_{tot}, abaxial GCL, $\uparrow g_{,max}$; Figure 12). Sampling adequacy was low (KMO = 0.45), though Bartlett's test confirmed sufficient correlations for analysis ($\chi^2 = 384.26$, df = 28, $p < 0.001$). The low KMO reflects limited correlation among traits spanning different functional domains (productivity, anatomy, physiology). PC1 (39.4% variance) described a guard cell size–stomatal density trade-off: species with larger guard cells (GCL_{ab}, +0.92) and greater leaf size (leaf area, +0.70; leaf biomass, +0.71) possessed lower stomatal densities (SD_{tot}, −0.78). PC2 (23.1% variance) captured a tissue construction axis

contrasting leaf mass per area (LMA, +0.82) with whole-plant biomass allocation (plant biomass, −0.78). Species were strongly differentiated (PERMANOVA $F_{7,39}$ = 25.61, R^2 = 0.82, p < 0.001; PERMDISP $F_{7,39}$ = 1.77, p > 0.05) and pairwise contrasts confirmed consistent multivariate separation (R^2 = 0.44–0.81, all p < 0.01).

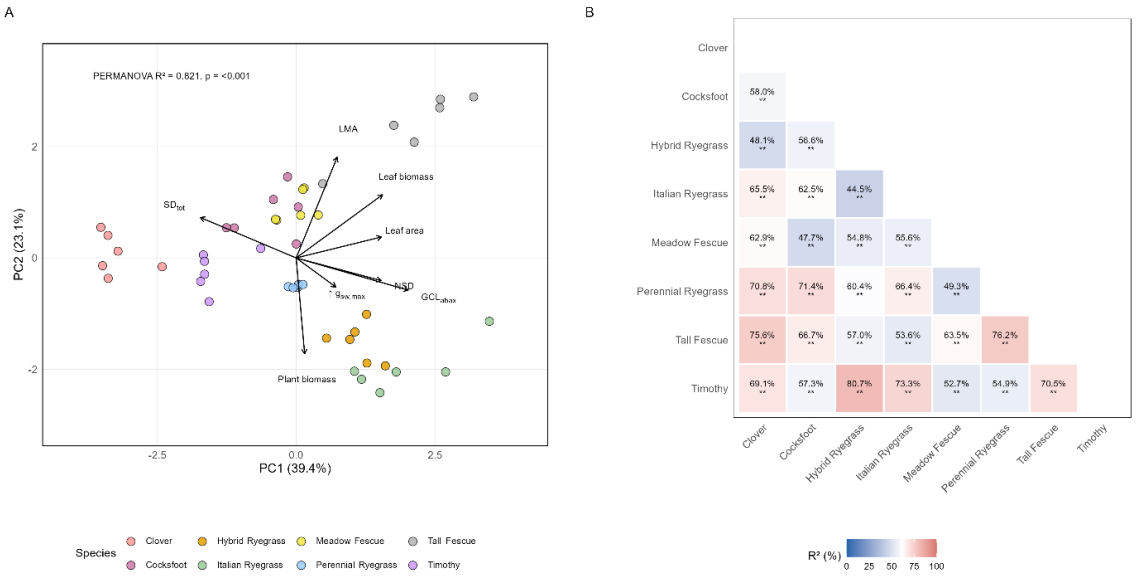

Figure 12. Principal component and pairwise analyses of field-relevant trait space used to select four representative species for field trials. (A) Principal component analysis of structural and productivity traits measurable in both glasshouse and field experiments (leaf area, leaf and plant biomass, LMA, SD_{tot}, abaxial GCL, ↑g_{max}). PC1 (39.4%) captured a guard cell size–stomatal density trade-off, while PC2 (23.1%) reflected tissue construction costs. (B) Pairwise PERMANOVA heatmap showing strong multivariate separation among species ($F_{7,39}$ = 25.61, R^2 = 0.82, p < 0.001; PERMDISP $F_{7,39}$ = 1.77, p > 0.05).

Based on the multivariate ordinations of kinetic and structural traits, four species were selected to represent contrasting functional strategies: Clover (high stomatal investment, slow kinetics, stomata-limited), Timothy (low stomatal investment, fast kinetics, biochemistry-limited), and Italian and Perennial ryegrass (intermediate grass strategies). These species span the functional range identified under controlled conditions. To evaluate whether these differences in trait syndromes translate to differential performance under field-relevant conditions, the four species were subjected to temporally structured shade treatments simulating bifacial agrivoltaic arrays.

6 Field Materials and Methods

6.1 Site Description and Experimental Shade Structures

The field experiment was conducted at the Hazelrigg Field Station, Lancaster, UK (54°01'50" N, 2°46'30" W), during the summer months of July and August 2025. The site experiences a cool-temperate oceanic climate, characterised by a mean annual temperature of 9.3 °C and total annual precipitation of 1307 mm, as recorded by Climate-Data.org (2025). To investigate the ecophysiological consequences of diurnal shading regimes, a key feature of bifacial, agrivoltaic system designs, two custom shade structures were constructed on a north-south alignment. These structures were designed to simulate the dynamic light environment cast by vertically mounted, bifacial solar panels. Each structure was composed of oriented strand board (OSB) panels measuring 1.2 m in height and 2.4 m in length, which were mounted vertically on timber uprights to form a continuous 4.8 m façade. The two primary structures were separated by a distance of 6.0 m, sufficient space for control blocks in full sunlight throughout the day (Figure 12A).

This specific configuration generated three distinct, replicated experimental treatments defined exclusively by the timing of shade incidence. A morning shade (AM) zone was established on the west side of each structure, which was shaded from sunrise until approximately solar noon. An afternoon shade (PM) zone was created on the east side of each structure, which was shaded from solar noon until sunset. A full-sun Control zone was positioned centrally between the two structures; it was therefore shaded for only brief, equal periods in the morning and evening. In addition to these three replicated treatments, a fourth data logger was positioned to the south of the entire experimental array in a consistently unshaded area. While this South logger was not part of the formal replicated design for plant trait analysis, it served as a contextual reference to monitor and confirm baseline environmental conditions outside the experimental infrastructure.

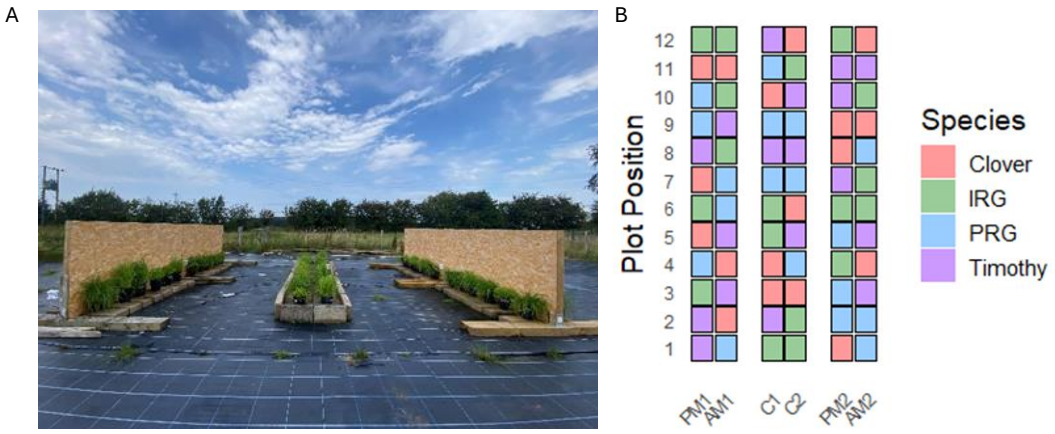

Figure 13. Experimental design and infrastructure for investigating diurnal shade regime effects on forage species. (A) Photograph of the field site showing two shade structures on a north-south alignment, constructed from vertically mounted OSB panels (1.2 m × 2.4 m), creating 4.8 m shaded façades on both eastern and western sides. This configuration generated distinct morning (AM) and afternoon (PM) shade zones, replicating the light environment of a bifacial solar array. (B) Schematic representation of the randomised complete block design showing the layout of a single experimental block containing 12 pot positions. The four species, Clover, Italian ryegrass (IRG), Perennial ryegrass (PRG), and Timothy, were randomly assigned to positions within each block, with three replicate pots per species. This randomisation was repeated in each of six blocks (two blocks per treatment: AM1/AM2, PM1/PM2, C1/C2), spatially aligned with the physical infrastructure: AM blocks west of the structures, PM blocks east, and Control blocks centrally between them. The design provided 72 pots total, yielding six independent replicates per species.

6.2 Plant Material and Experimental Cultivation

To test the hypothesis that forage species with contrasting functional strategies would differ in their phenotypic plasticity to temporal shade regimes, four key species were selected based on multivariate trait divergence observed in the preceding glasshouse experiment. The selected species were White Clover, Timothy, PRG and IRG. These are widely used in temperate improved grassland mixtures, including solar-compatible swards, and are already incorporated into commercial “solar park” and long-term grazing seed mixes because of their compatibility with partial shade and their

contrasting rooting depths and growth forms (Andrew et al., 2021; Mason et al., 2016). They also span a strategic spectrum of leaf economic and stomatal kinetic strategies that typify UK forage systems, providing a functionally and agronomically relevant framework for evaluating phenotypic plasticity to agrivoltaic-style diurnal shading regimes.

Seeds of each species were sown in June 2025 into 4-L cylindrical pots (22 cm deep × 16.5 cm diameter) filled with a nutrient-rich peat-based compost (Petersfield Growing Mediums, Leicester, UK), using agronomically realistic sowing rates (Cotswold Grass Seeds, 2025a) (Section 4.1;Table 1). Germination and initial establishment of seedlings was in a controlled-environment glasshouse with set day/night temperatures of 21/11 °C to ensure uniform seedling vigour and eliminate any emergence bias. After a nine-day establishment period, pots were transferred to their respective field treatments in early July 2025 and maintained for a total of 39 days (5.5 weeks), encompassing the peak summer growing season.

Pots were elevated on bricks atop a geotextile membrane to ensure consistent application of shade treatments across the entire pot canopy and to avoid edge effects from the gap between the shade structure base and the ground. They were spaced 22 cm apart to minimise neighbour shading and thereby maintain reasonably consistent light conditions among individuals and species within each treatment. Throughout the experimental period, plants were watered daily to drip point, to eliminate water stress as a confounding variable.

6.3 Experimental Design and Layout

The experiment was established as a randomised complete block design (Mead et al., 2017). The treatments were spatially aligned to the physical shade structures. Each of the three primary treatments (AM shade, PM shade, Control) comprised two replicate blocks (designated AM1/AM2, PM1/PM2, C1/C2), resulting in a total of six blocks. Each block contained 12 pots, representing the four species with three replicate pots per species (Figure 13B). Within each block, the positional order

of the 12 pots was fully randomised to avoid any systematic spatial biases. Across the entire experiment, the total sample size consisted of 72 pots, providing six experimental replicates for each of the 12 species-by-treatment combinations, providing a balanced design for testing main effects of species and treatment, as well as their interaction.

6.4 Environmental Monitoring and Microclimate Characterisation

To quantitatively characterise the light and microclimatic environment within each treatment zone, conditions were monitored continuously during the 39-day experiment using HOBO Micro Station data loggers (H21-USB; Onset Computer Corporation, Bourne, MA, USA). Each station was equipped with a photosynthetically active radiation (PAR) sensor (S-LIA-M003), and a combined air temperature and relative humidity sensor (S-THB-M002) housed within a solar radiation shield (RS3-B) to protect against radiative heating errors. All PAR sensors were mounted on light brackets (M-LBB) and carefully levelled to ensure accurate measurements. Both PAR, temperature and relative humidity sensors were positioned 0.4 m above the black weed fabric surface, at roughly the same height as grass plant canopies emerged from their pots. Data were logged at 5 min intervals, providing high-resolution temporal data, and were subsequently downloaded via HOBOware Pro software (Onset Computer Corporation, 2024).

Vapour pressure deficit (VPD), a key biophysical determinant of evaporative demand and plant water stress, was calculated from the logged air temperature (T, °C) and relative humidity (RH, %) data following the established FAO-56 Tetens equation (Allen et al., 1998). Saturation vapour pressure (e_s, kPa) was first calculated using Equation 17, VPD was then derived using Equation 18.

Equation 17. Saturation vapour pressure:

$$e_s(T)\ [kPa] = 0.6108 \cdot exp\left(\frac{17.27 \cdot T}{T + 237.3}\right)$$

Equation 18. Vapour pressure deficit:

$$VPD\ [kPa] = e_s(T)\ \cdot \left(1\ -\ \frac{RH}{100}\right)$$

The daily light integral (DLI, mol m^{-2} d^{-1}), representing the total photosynthetically active photon flux received per square metre per day, was calculated for each treatment by time-integration of the logged PAR values (Faust et al., 2005) using Equation 19, where PAR_i is the instantaneous photosynthetic photon flux density (µmol m^{-2} s^{-1}) at time step i, Δt_i is the logging interval in seconds (300 s), and the divisor of 10^6 converts the total from micromoles to moles.

Equation 19. Daily light integral:

$$DLI\ [mol \cdot m^{-2} \cdot d^{-1}] = \frac{\sum(PAR_i \cdot \Delta t_i)}{10^6}$$

The analysis of environmental data followed a structured progression from qualitative verification to quantitative hypothesis testing. Initially, the high-resolution data were visually inspected as full diurnal profiles to confirm that the treatments consistently produced the intended morning and afternoon shade regimes. Next, a precise temporal framework was established for formal analysis. Using the suncalc package (Thieurmel and Elmarhraoui, 2019), daytime was programmatically defined for each date, and the data were subsequently aggregated into two distinct analytical windows: morning (sunrise to solar noon) and afternoon (solar noon to sunset). For each window, instantaneous environmental variables (PAR, temperature, relative humidity, and VPD) were calculated as daily means from the high-resolution (5-min interval) measurements. By contrast, DLI was calculated as the time-integrated sum of photosynthetic photon flux within each window. These aggregated values served as response variables in statistical models used to test for significant treatment effects.

6.5 Trait Measurements for Functional Response Quantification

After six weeks of growth, a comprehensive suite of functional traits was measured to capture leaf-level and stomatal plasticity in response to the shade treatments. For each plant, a single, apical, fully expanded leaf was excised at the ligule and sealed in a humidified plastic bag to prevent desiccation during transport to the laboratory, which was done within 1h. Stomatal impressions and image analysis followed the protocol described in Section 4.7.

The leaf used for stomatal impressions was used for leaf area measurement using a calibrated leaf-area meter (LI-3100C; LI-COR Inc. Lincoln NE, USA). Afterwards, it was oven-dried at 70 °C for at least 72 hours to reach a constant mass. Leaf mass per area (LMA, g m^{-2}) was calculated as the leaf dry mass divided by its leaf area. At the final harvest, 48 days after sowing, the entire above-ground biomass of each plant was harvested by cutting at the soil surface, oven-dried to constant mass, and weighed to determine total plant biomass.

To capture higher-order stomatal traits that integrate multiple anatomical features, two composite indices were calculated. The NSD index was calculated Muir et al. (2014), which quantifies the relative allocation of stomata between adaxial and abaxial leaf surfaces (Equation 16; Section 4.7), and a proxy for maximum stomatal conductance (g_{max} proxy). The g_{max} proxy was formulated to capture the functional coordination between stomatal size and density within multivariate trait space By simplifying the theoretical framework presented in Franks and Beerling (2009), retaining the core scaling relationship in which theoretical maximum pore area scales with SD (mm^{-2}) and the square of GCL (Equation 20). This relationship is based on the biophysics of gas diffusion through stomatal pores and the biomechanics of guard cell function (Dow et al., 2014; Franks and Beerling, 2009; Sack and Buckley, 2016). By combining size and density parameters for both leaf surfaces into a single integrated metric, the composite index provides a functionally meaningful variable for multivariate analysis that can be calculated for all species, complementing the analysis of individual stomatal traits.

While based on established biomechanical principles, this novel, simplified formulation has not been independently validated against direct physiological measurements of stomatal conductance.

Equation 20. Proxy for stomatal conductance (g_{max} proxy):

$$g_{max}\,proxy = (SD_{ad} \times {GCL^2}_{ad}) + (SD_{ab} \times {GCL^2}_{ab}),$$

where SD is stomatal density (mm^{-2}) and GCL is guard cell length (µm), and the resulting proxy is a dimensionless index proportional to theoretical maximum stomatal conductance.

6.6 Statistical Analysis Framework

All statistical analyses were conducted in R version 4.4.1 (R Core Team, 2024) within the RStudio integrated development environment (Posit Team, 2024). Data manipulation and visualisation were performed using the `tidyverse` suite of packages (Wickham et al., 2019). The analysis was structured into three distinct components: environmental data, multivariate, and univariate traits.

6.6.1 Environmental Data Analysis

Linear mixed-effects models were used to test for treatment effects on environmental variables, using the nlme package (Pinheiro et al., 2024). To avoid pseudoreplication from multiple measurements per day, daily aggregated values for each environmental variable (PAR, T, RH, VPD, and DLI) were calculated separately for morning and afternoon windows, obtaining a single observation per treatment, per day, per window (156 observations per window: 39 dates × 4 treatments). Separate models were fitted for morning and afternoon windows for each environmental variable, with the model structure: variable ~ treatment + (1|date). This approach allowed direct assessment of whether AM and PM shade structures created time-specific microclimate effects, while accounting for day-to-day environmental variation by including date as a random intercept.

Model assumptions of normality and homoscedasticity were assessed using Shapiro-Wilk tests and Levene's tests on normalised residuals. While heterogeneous variance structures (varIdent) provided better model fits according to AIC criteria (ΔAIC = -21 to -197), homogeneous variance models were selected to ensure comparable standard errors across treatments for multiple-comparison procedures and to avoid inflated standard errors that can produce misleading compact letter displays (Table S1). Linear mixed models are robust to moderate violations of normality assumptions when sample sizes are adequate (Schielzeth et al., 2020).

Statistical inference for fixed effects used Type III F-tests with denominator degrees of freedom calculated via the containment method (Pinheiro and Bates, 2000). This method accounts for both the fixed-effect structure (4 treatment levels) and the random-effect structure (39 date levels), providing a denominator df ≈ 114 for hypothesis tests. Post-hoc pairwise comparisons between treatments were performed on estimated marginal means using the Šidák correction for multiple comparisons, implemented in the emmeans package (Lenth, 2025). Standard errors and confidence intervals for estimated marginal means were calculated based on the number of random effect levels (df = 38), reflecting the true replication at the daily level. Compact letter displays derived from these comparisons were used to indicate statistical groupings in figures. Equivalent analyses for the full photoperiod (sunrise to sunset) are presented in Figure S1.

6.6.2 Multivariate Trait Analysis

To integrate the suite of leaf and stomatal traits into a cohesive functional framework, a PCA was performed on a correlation matrix using the 'prcomp' function. The trait set comprised leaf area, LMA, plant biomass, leaf biomass, adaxial and abaxial SD, abaxial GCL, the NSD index, and a composite index integrating stomatal size and density (g_{max} proxy). Adaxial GCL was excluded from the PCA because White Clover is hypostomatous and lacks adaxial stomata, precluding direct comparison of this trait across all four species. The composite index (Equation 20) provided an alternative approach

to capture size-density integration for comparative analysis across species with contrasting stomatal distributions. Data were mean-centred and scaled to unit variance prior to ordination. The suitability of the data for PCA was confirmed via the Kaiser-Meyer-Olkin measure of sampling adequacy (KMO = 0.691) and Bartlett's test of sphericity ($p < 0.001$).

Multivariate treatment effects were assessed using a combination of methods. Multivariate normality was assessed on the residuals of a MANOVA model using Mardia's test (Mardia, 1970). The results showed that the normality assumption was not met ($p < 0.001$). Given this violation, a non-parametric PERMANOVA (Anderson, 2001) was conducted on Euclidean distances between individuals using the `adonis2()` function in the `vegan` package (Oksanen et al., 2025), with 9999 permutations to test the significance of species, treatment, and their interaction. Homogeneity of multivariate dispersions was tested using the `betadisper()` function (PERMDISP) in `vegan`. To quantify the magnitude of phenotypic plasticity for each species, the Euclidean distance between shade treatment centroids and their respective control centroid was calculated in the space defined by the first two principal components. The statistical significance of these centroid displacements was assessed using permutation tests (9999 permutations), and the resulting p-values were adjusted for multiple testing using the Benjamini-Hochberg false discovery rate (FDR) procedure (Benjamini and Hochberg, 1995). A supplementary PCA and PERMANOVA were conducted on a dataset containing only the three grass species (Timothy, PRG, IRG) to ascertain whether the inclusion of Clover obscured more subtle patterns of functional differentiation among the grasses (Figure S3 and Figure S4).

6.6.3 Univariate Trait Analysis

Univariate trait responses were analysed using generalised least squares (GLS) models, implemented in the `nlme` package (Pinheiro et al., 2024). Each trait was modelled with `Species`, `Treatment`, and their `interaction` as fixed effects. To handle potential heteroscedasticity among groups, model structures with and without variance weighting functions (e.g., `varIdent`) were

compared using Akaike's Information Criterion (AIC) under maximum likelihood estimation. Variance-weighted models were selected for all eight traits based on better AIC values, consistent with recommendations to apply variance structures consistently rather than selectively (Gelman and Hill, 2006). The best-fitting model was then refitted using restricted maximum likelihood (REML) for final parameter estimation (Zuur et al., 2009). Type II ANOVA tables were obtained from the selected models using the `Anova()` function in the `car` package (Fox and Weisberg, 2019). Estimated marginal means (EMMs) were computed for all species-by-treatment combinations (Lenth, 2025). Post-hoc pairwise comparisons were performed using Šidák's test for all possible contrasts. For key traits, effect sizes were expressed as percentage differences of the raw trait means relative to the control. Model assumptions were checked; the normality of residuals was assessed using the Shapiro-Wilk test, and homogeneity of variances was tested using Levene's test. Using the same variance structures for all traits aligns with statistical practices that favour maintaining complex variance structures when supported by model selection criteria (Gelman and Hill, 2006).

7 Field Results

7.1 Experimental Infrastructure Creates Targeted Diurnal Light Environments

The successful creation of distinct, temporally segregated light environments was a prerequisite for testing the research question. Averaged diurnal profiles for PAR, temperature, relative humidity, and VPD visually demonstrated clear separation between treatments, with AM and PM shade regimes reducing PAR as expected (Figure 14). The South reference sensor, positioned outside the experimental array to capture unshaded conditions independent of structural effects, recorded values intermediate between Control and shaded treatments across most variables, suggesting minor inter-sensor calibration variation rather than positional effects.

To quantitatively validate differences in microclimate conditions between the morning and afternoon periods, analysis was conducted on daily-aggregated values for each time window (Figure 15). Treatment effects on photosynthetically active radiation (PAR; Figure 15A) were highly significant in both morning ($F_{3,114} = 52.02$, $p < 0.001$) and afternoon periods ($F_{3,114} = 95.17$, $p < 0.001$), confirming that the shade structures created the intended diurnal light regimes. During the morning period, the AM shade treatment reduced PAR by 47% relative to the Control (283 ± 35 vs. 535 ± 35 µmol m^{-2} s^{-1}; $p < 0.001$), while PM shade and South reference treatments did not differ significantly from the Control ($p > 0.05$). This pattern reversed in the afternoon: the PM shade treatment reduced PAR by 50% compared to the Control (343 ± 35 vs. 681 ± 35 µmol m^{-2} s^{-1}; $p < 0.001$), whereas the AM shade treatment showed no significant reduction (631 ± 35 µmol m^{-2} s^{-1}; $p > 0.05$). Notably, the PM shade treatment uniquely reversed natural diurnal patterns at the field site, with morning PAR exceeding afternoon levels by 185 µmol m^{-2} s^{-1}.

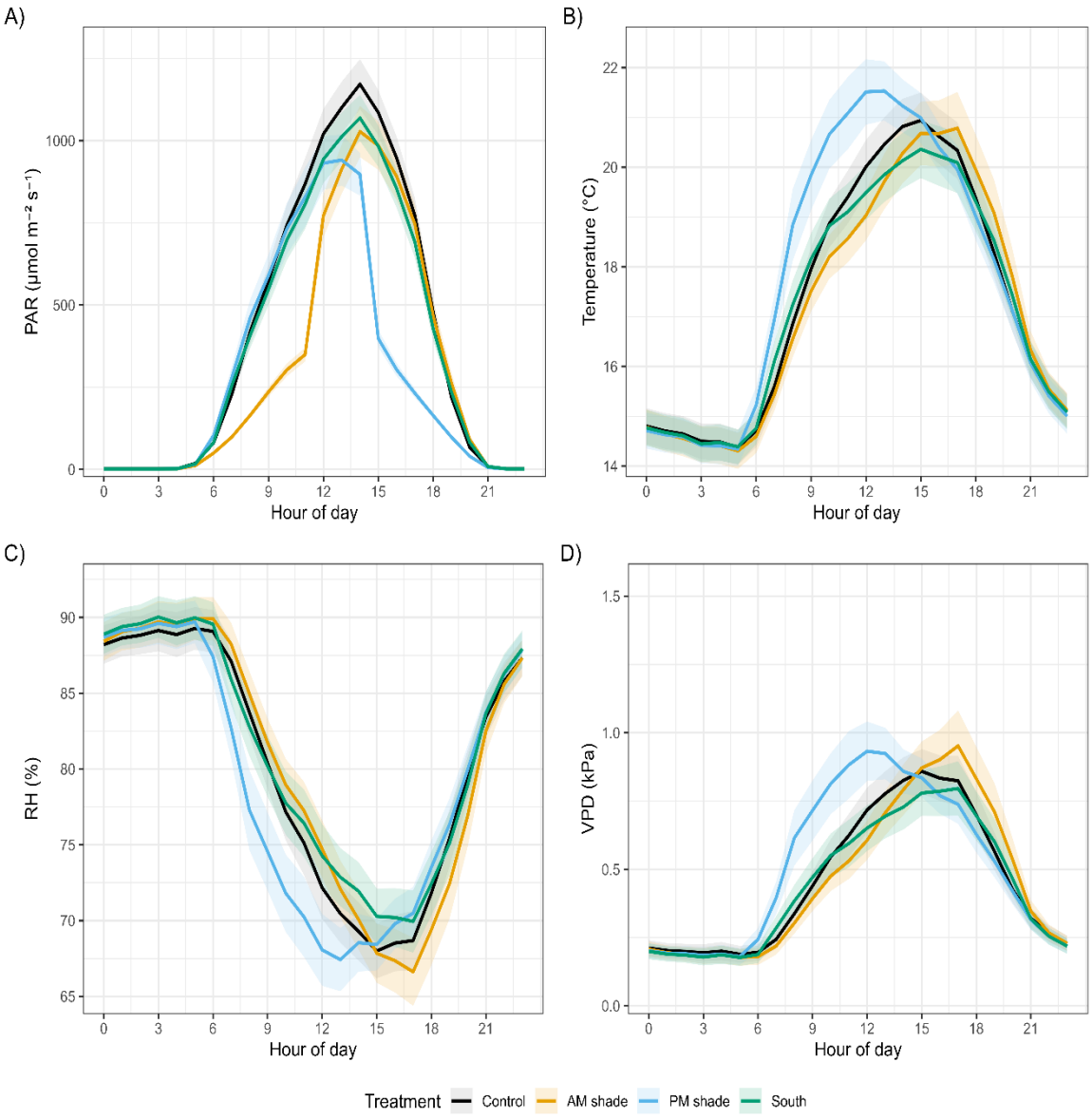

Figure 14. Microclimate conditions under experimental diurnal shading regimes. Continuous (5 min interval) environmental measurements made over the 39-day field experiment are summarised to show diurnal patterns of (A) photosynthetically active radiation (PAR), (B) air temperature (°C), (C) relative humidity (RH%), and (D) vapour pressure deficit (VPD, kPa) within treatment zones. Lines represent hourly means with shaded ribbons indicating ±1 standard error across days (n = 39). Treatment colours: Control (black), AM shade (orange), PM shade (blue), South reference (green).

To complement these instantaneous light measurements, cumulative photon flux was quantified as the DLI for each time window. Treatment effects on morning DLI were highly significant ($F_{3,114} = 50.96$, $p < 0.001$), with the AM shade treatment receiving 47% less light than the Control (8.18 ± 1.03 vs. 15.52 ± 1.03 mol m^{-2}; $p < 0.001$), while PM shade, South reference, and Control treatments formed a statistically indistinguishable group (all $p > 0.05$; Figure 15E). This pattern was mirrored in the afternoon ($F_{3,114} = 90.74$, $p < 0.001$); the PM shade treatment received 50% less cumulative light than the Control (9.95 ± 1.03 vs. 19.77 ± 1.03 mol m^{-2}; $p < 0.001$) while AM shade did not differ from the Control (18.35 ± 1.03 mol m^{-2}; $p > 0.05$). These DLI reductions demonstrate that shade structures created substantial cumulative light deficits during the respective shaded periods. When integrated over the full photoperiod, treatment effects on total daily DLI remained highly significant ($F_{3,114} = 80.23$, $p < 0.001$; Figure S2). Both shade treatments significantly reduced cumulative daily light ($p < 0.001$), by 25% for AM shade (26.5 ± 1.77 mol m^{-2} d^{-1}) and 28% for PM shade (25.3 ± 1.77 mol m^{-2} d^{-1}) compared to the Control (35.3 ± 1.77 mol m^{-2} d^{-1}), while the South reference recorded intermediate values (32.8 ± 1.77 mol m^{-2} d^{-1}; $p < 0.001$ vs Control; Figure S2).

Associated with their impact on PAR, shading regimes generated corresponding time-specific modifications to T, RH, and VPD (Figure 15B-D). Morning T showed a significant treatment effect ($F_{3,114} = 45.45$, $p < 0.001$), with the AM shade treatment creating a cooler microclimate (17.0 ± 0.43 °C) compared to the Control (17.5 ± 0.43 °C; $p < 0.001$), a reduction of 0.5 °C (Figure 15B). The PM shade treatment was significantly warmer than all other treatments during the morning period (18.8 ± 0.43 °C; $p < 0.001$). In the afternoon, temperature differences were smaller, but remained significant ($F_{3,114} = 4.97$, $p = 0.003$), with treatments forming overlapping groups and no clear pattern of shade-induced cooling.

Relative humidity displayed an inverse pattern to temperature (Figure 15C). Morning RH was significantly affected by treatment ($F_{3,114} = 40.75$, $p < 0.001$), with the AM shade increasing humidity

by 1.53 percentage points relative to the Control (82.6 ± 1.65% vs. 81.1 ± 1.65%; $p < 0.001$), while the PM shade treatment showed the lowest morning humidity (76.9 ± 1.65%; $p < 0.001$; Figure 15C). Afternoon RH also showed significant treatment effects ($F_{3,114} = 21.61$, $p < 0.001$), with the AM shade treatment creating the driest afternoon conditions (70.8 ± 1.77%; $p < 0.001$ compared to Control at 72.1 ± 1.77%).

Vapour pressure deficit (VPD), a key determinant of evaporative demand, showed significant treatment effects in both morning ($F_{3,114} = 29.69$, $p < 0.001$) and afternoon periods ($F_{3,114} = 8.98$, $p < 0.001$; Figure 15D). During the morning, VPD was lowest under the AM shade treatment (0.38 ± 0.059 kPa), representing a reduction of 0.05 kPa (12.5%) compared to the Control (0.43 ± 0.059 kPa; $p < 0.001$). The PM shade treatment created significantly higher morning VPD (0.62 ± 0.059 kPa; $p < 0.001$) than all other treatments. In the afternoon, the pattern reversed, with the AM shade treatment generating the highest VPD (0.77 ± 0.078 kPa; $p < 0.001$), an increase of 0.07 kPa (9.4%) compared to the Control (0.7 ± 0.078 kPa). Although absolute VPD values remained low across all treatments (0.38–0.77 kPa), these shifts show that the shade structures consistently and significantly modified atmospheric evaporative demand in a time-of-day-dependent manner.

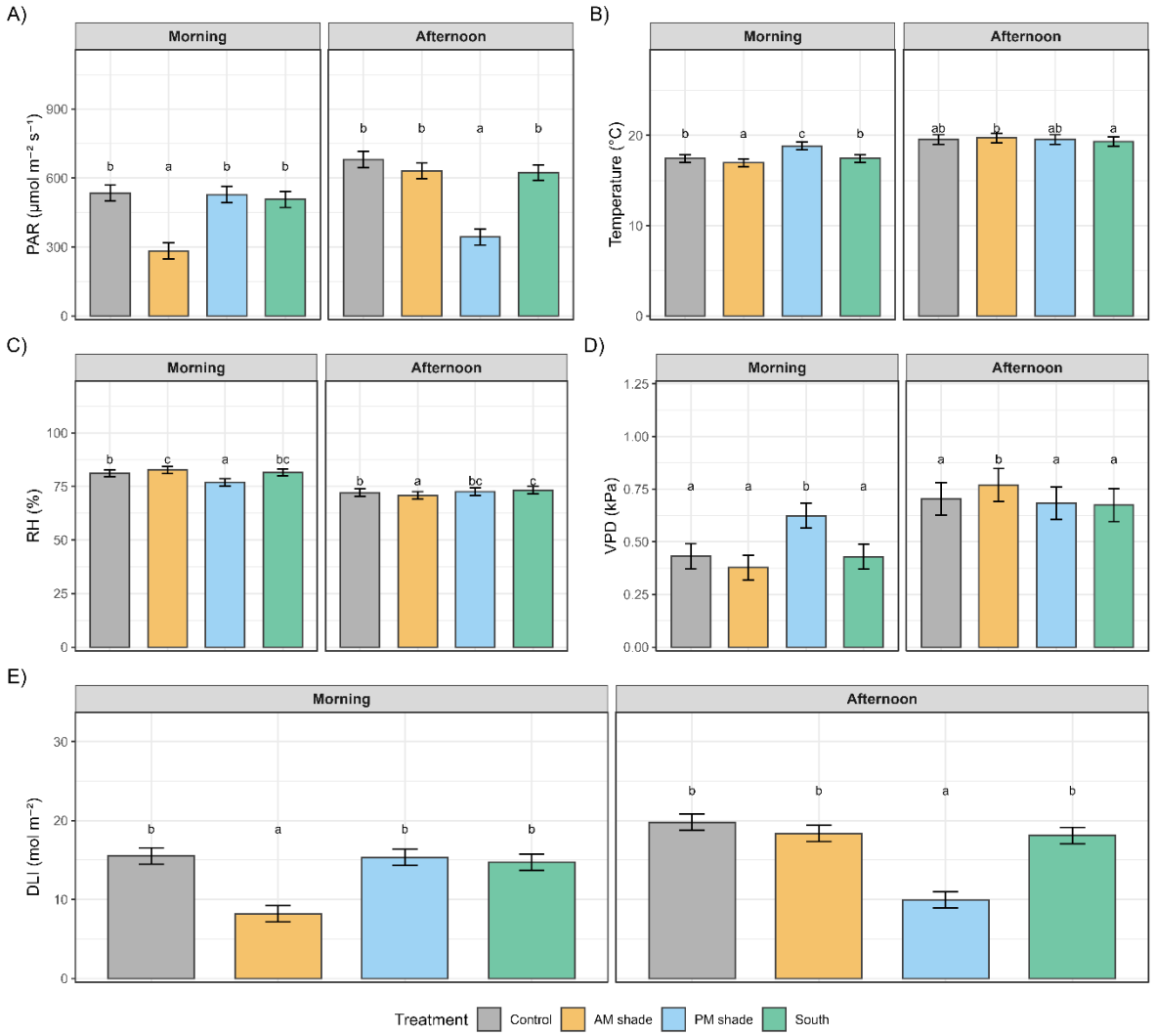

Figure 15. Morning and afternoon microclimatic conditions under temporally distinct shade regimes during a 39-day field experiment at Hazelrigg Experimental Station, Lancaster, UK. Mean values ± SE for (A) photosynthetically active radiation (PAR), (B) air temperature, (C) relative humidity (RH), and (D) vapour pressure deficit (VPD), for morning (sunrise to solar noon) and afternoon (solar noon to sunset) periods. (E) Daily Light Integral (DLI) for each treatment within morning and afternoon windows (n = 39 days). Bar colours denote treatments (grey = Control, orange = AM shade, blue = PM shade, green = South reference). Compact letter displays above bars summarise Šidák-adjusted comparisons of estimated marginal means between treatments within each time window; treatments sharing the same letter within a panel were not significantly different ($p > 0.05$). All treatment effects were highly significant ($p < 0.001$), except afternoon temperature ($p < 0.01$).

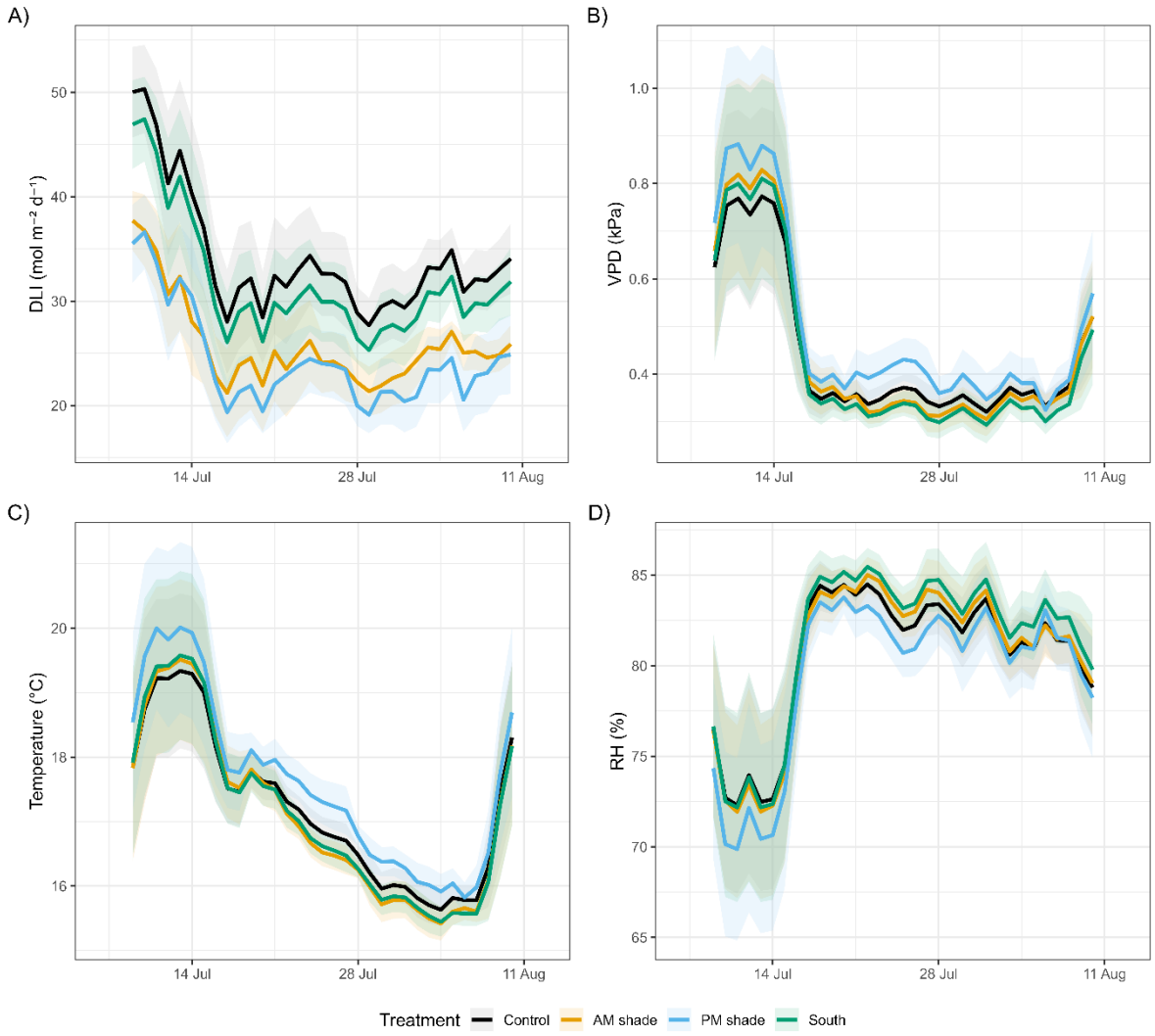

Figure 16. Temporal consistency of treatment effects on environmental variables during the experimental period at Hazelrigg Experimental Station, Lancaster, UK. Seven-day rolling means ± SE of daily aggregated values for (A) daily light integral (DLI, mol m^{-2} d^{-1}), (B) vapour pressure deficit (VPD, kPa), (C) air temperature (°C), and (D) relative humidity (%) across a 39-day field experiment. Each data point represents the rolling average of daily means calculated from high-resolution measurements (5-minute intervals) within each 24-hour period. Lines show rolling averages with shaded ribbons representing standard error, demonstrating maintained separation between treatments despite underlying meteorological variability. Colours denote treatments (black = Control, orange = AM shade, blue = PM shade, green = South reference). Temperature and RH are shown to illustrate their contribution to observed VPD patterns.

To demonstrate the temporal consistency of these treatment effects throughout the experimental period, seven-day rolling averages for DLI, VPD, air temperature and relative humidity (Figure 16). These descriptive time series show that, despite underlying day-to-day meteorological

variability, the treatment separations established by statistical analyses (Figure 14 and Figure 15) were observable consistently throughout the July-August field experimental period.

In summary, the environmental data demonstrate that the experimental infrastructure created diurnal shading regimes with significant differences in microclimate. This provided the foundation for investigating how the timing of shade, distinct from its total quantity, influences phenotypic responses in forage species.

7.2 Multivariate Analysis Reveals Species-Specific Patterns of Integrated Phenotypic Response

Having established the distinct environmental treatments, the study investigated how these regimes shaped the overall phenotypic architecture of the four forage species. A principal component analysis (PCA) performed on seven plant traits identified the primary axes of trait variation across the 72 individual plants, with the first two components (PCs) accounting for 87.9% of the total variance (PC1 = 73.4%, PC2 = 14.5%; Figure 17). Variable loadings indicated that PC1 represented a gradient of plant size and mass investment, with positive loadings from leaf biomass (0.42), abaxial guard cell length (0.42), the g_{max} proxy (0.39), plant biomass (0.38), and leaf area (0.36). By contrast, PC2 represented a gradient in leaf economic strategy, defined by positive loadings from leaf area (0.51) and plant biomass (0.27) and negative loadings from LMA (-0.53) and the normalised stomatal density index (-0.52). The distribution of species within this trait space under control conditions showed clear separation, with Italian ryegrass (IRG) occupying the positive extreme of PC1, characterised by high values for size-related traits, while Clover occupied the negative extreme. Perennial ryegrass (PRG) was separated from the other species along PC2, characterised by higher LMA and NSD.

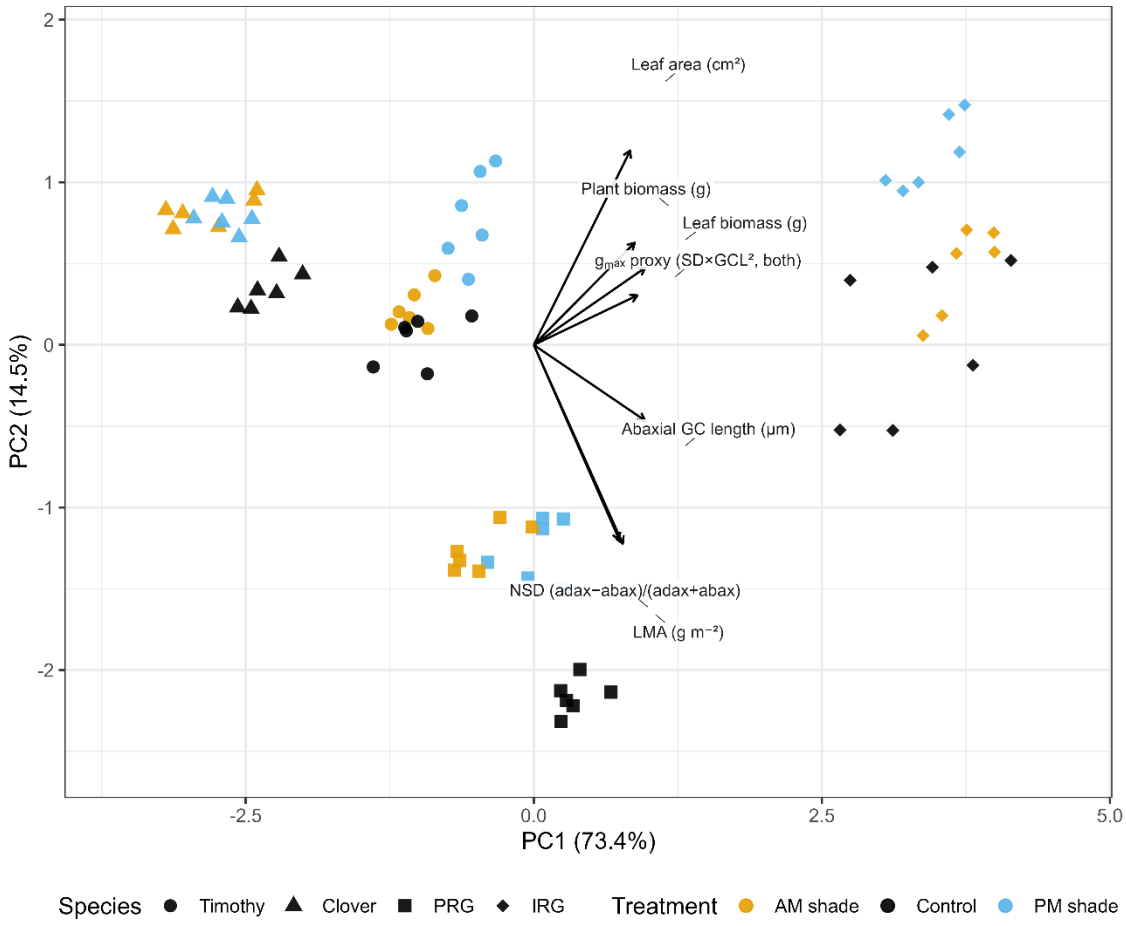

Figure 17. Multivariate principal component analysis (PCA) of four forage species under diurnal shading regimes during a 39-day field experiment. Biplot of the first two principal components (PC1 = 73.40%, PC2 = 14.52%) derived from seven standardised plant traits: plant biomass (g), leaf biomass (g), g_{max} proxy, abaxial guard cell length (µm), normalised stomatal density (NSD) index, leaf mass per area (g m^{-2}) (LMA). Points represent individual plants (n = 72). Species are distinguished by shape (circle = Clover, triangle = Timothy, square = Perennial ryegrass, diamond = Italian ryegrass). Treatments are indicated by colour (grey = Control, blue = PM shade, orange = AM shade). Vectors show trait loadings, with arrow length and direction proportional to the correlation strength of each trait with the principal components.

To statistically validate these visual patterns and the effect of shading, PERMANOVA was utilised, which is robust to violations of parametric assumptions. This analysis confirmed highly significant main effects of species ($F_{3,60}$ = 432.46, R^2 = 0.880, $p < 0.001$) and treatment ($F_{2,60}$ = 31.21, R^2 = 0.042, $p < 0.001$), and a significant species × treatment interaction ($F_{6,60}$ = 8.96, R^2 = 0.0365, $p <$

0.001). The presence of this significant interaction indicated that the species responded differently to the timing of shade, necessitating a species-specific analysis of phenotypic plasticity.

Given this significant interaction, the magnitude of multivariate plasticity for each species was quantified by calculating the Euclidean distance between treatment centroids and their control positions in the PCA space (Figure 18). This analysis revealed species-specific patterns of response. For PRG, both AM shade ($d = 1.22$, 95% CI = 1.116–1.352, FDR-adjusted $p < 0.01$) and PM shade ($d = 0.96$, 95% CI = 0.809–1.108, FDR-adjusted $p < 0.01$) produced significant and substantial displacements. Similarly, Clover shifted significantly under both AM ($d = 0.70$, 95% CI = 0.563–0.900, FDR-adjusted $p < 0.01$) and PM shade ($d = 0.58$, 95% CI = 0.469–0.726, FDR-adjusted $p < 0.01$). By contrast, IRG and Timothy exhibited more selective responses, shifting significantly only under PM shade (IRG: $d = 1.14$, 95% CI = 0.780–1.608, FDR-adjusted $p < 0.01$; Timothy: $d = 0.90$, 95% CI = 0.631–1.179, FDR-adjusted $p < 0.01$), while their shifts under AM shade were not statistically significant (IRG: FDR-adjusted $p > 0.05$; Timothy: FDR-adjusted $p > 0.05$).

Further analysis of multivariate dispersion (PERMDISP) showed significant differences in within-group dispersion among species ($F_{3, 68} = 9.67$, $p < 0.001$), with IRG exhibiting greater phenotypic variation than Clover, Timothy, and PRG. In contrast, dispersion did not differ among treatments ($F_{2, 69} = 0.09$, $p = 0.916$), indicating that shading altered the mean trait values but not the variance around those means. A supplementary PCA restricted to the three grass species further clarified that Timothy occupied a distinct functional phenotype from the two ryegrasses, primarily driven by its higher LMA and divergent stomatal distribution (NSD), patterns that were partially obscured when the distantly related Clover was included in the analysis (Figure S4).

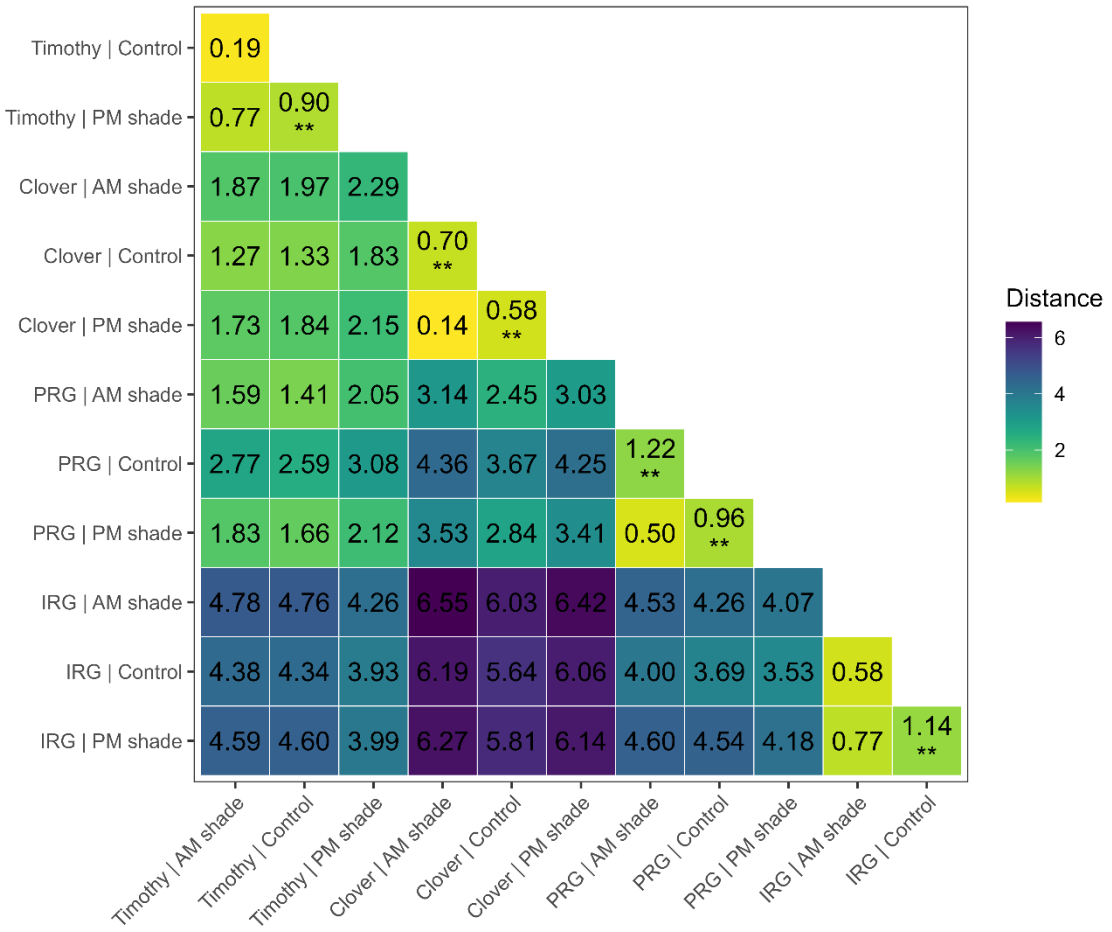

Figure 18. Heatmap of Euclidean distances between species x treatment centroids in the PCA space, calculated from PC1 and PC2 scores. Distances quantify multivariate separation of treatment means; significant centroid shifts from control treatment, tested using permutation tests with Benjamini–Hochberg FDR adjustment, are indicated by an asterisk (**, $p < 0.01$). Colour gradient denotes centroid distance (lighter yellow = smaller functional differences, darker purple = larger differences).

7.3 Univariate Trait Analysis Elucidates Underlying Structural and Stomatal Response Mechanisms

To identify the specific morphological and anatomical adjustments underlying the multivariate responses, a univariate analysis was conducted. This revealed that plasticity was most pronounced in structural and biomass traits, with highly significant species × treatment interactions governing their responses (Figure 19; all $p < 0.001$).

Stomatal morphology exhibited constrained and surface-specific plasticity. Guard cell length on the adaxial surface showed a significant species x treatment interaction (Figure 19D; $F_{4,45} = 168.48$, $p < 0.001$), with PRG showing significant reductions under both shade treatments and IRG under PM shade only. However, adaxial stomatal density, while showing a significant species x treatment interaction (Figure 19E; $F_{4,45} = 27.13$, $p < 0.001$), exhibited no significant pairwise differences within any species. For the abaxial surface, guard cell length showed a significant interaction, but no significant within-species effects were detected (Figure 19F). Abaxial stomatal density was significantly influenced by the species × treatment interaction (Figure 19G; $F_{6,60} = 582.12$, $p < 0.001$), with Clover and Timothy showing significant reductions under shade, while the ryegrasses showed no significant changes.

Individual leaf area, a key determinant of light capture potential, exhibited a strong species x treatment interactive effect ($F_{6,60} = 30.33$, $p < 0.001$), which highlighted fundamental differences between the dicot species (Clover) and the monocot grasses (Figure 19A). The ryegrasses demonstrated notable plasticity, with PRG increasing leaf area most dramatically under afternoon shade (+64.0%, $p < 0.05$) and IRG increasing significantly under both morning (+20.0%, $p < 0.05$) and afternoon shade (+38.0%, $p < 0.01$). By contrast, Clover and Timothy showed no statistically significant changes in leaf area in response to shading, indicating a more conservative leaf deployment strategy.

Analysis of individual leaf biomass, representing direct investment in photosynthetic tissue, revealed a significant species × treatment interaction (Figure 19B; $F_{6,57} = 30.68$, $p < 0.001$) that highlighted divergent allocation strategies under temporal shading. Both ryegrass species significantly increased leaf biomass under shade; however, PRG responded specifically to PM shade (+27.0%, $p < 0.05$), whereas Italian ryegrass leaf biomass increased under both morning (+11.0%, $p < 0.05$) and afternoon shade (+12.0%, $p < 0.05$). By contrast, Timothy and Clover showed no significant differences in leaf biomass across diurnal shading regimes.

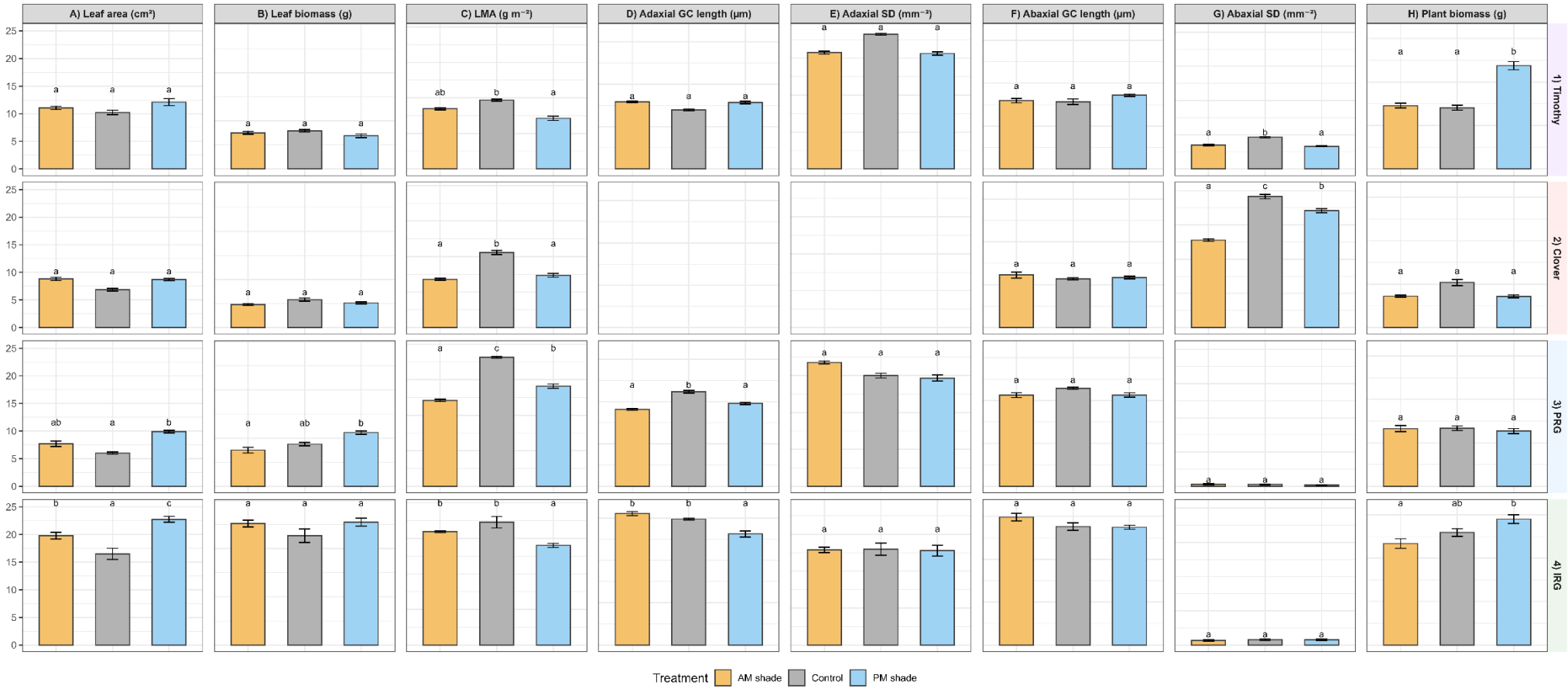

Figure 19. Species-specific trait means under diurnal shading regimes during a 39-day field experiment for (A) leaf area, (B) leaf biomass, (C) leaf mass per area (LMA), (D) adaxial guard cell length, (E) adaxial stomatal density, (F) abaxial guard cell length, (G) abaxial stomatal density, and (H) plant biomass. Rows correspond to species: (1) Timothy, (2) Clover, (3) Perennial ryegrass (PRG), (4) Italian ryegrass (IRG). Bars represent raw means ±1 standard error (n = 6 biological replicates per species per treatment). Bar colours represent treatments (orange = AM shade, grey = Control, blue = PM shade). Compact letter displays above bars summarise Šidák-adjusted comparisons of estimated marginal means from species × treatment linear models. Treatments sharing the same letter within a species and panel were not significantly different ($p > 0.05$). As Clover is hypostomatous it was excluded from the adaxial trait analysis.

Combining leaf biomass with leaf area at the level of individual leaves, the investment of mass per unit leaf area (LMA) was greater in the control than the shaded treatments in all species (Figure 19C). However, the extent of differences varied by species ($F_{6,60} = 89.52$, $p < 0.001$). Clover significantly reduced LMA under both shade treatments (AM: -35.8%, PM: -30.4%) compared to the control, indicating a shift towards thinner leaves in lower light. PRG exhibited the most complex response, with all three treatments differing significantly: AM shade (-33.3%) resulted in the lowest LMA, followed by PM shade (-22.3%), and then the control. Timothy and IRG showed significant reductions only under PM shade, mirroring their multivariate response patterns.

For whole-plant biomass, there were also significant species × treatment interactions (Figure 19H; $F_{6,60} = 109.09$, $p < 0.001$). Timothy demonstrated a remarkable biomass response, producing significantly more biomass under PM shade conditions (68.7%) compared to the control. IRG also produced the most biomass under PM shade, which was significantly greater (24.0%) than plants receiving AM shade. Conversely, Clover and PRG showed no significant treatment effects on final plant biomass, suggesting that their larger LMA responses and clearer multivariate responses to shade were associated with smaller among shade-treatment differences in total biomass accumulation under the conditions and timeframe of this experiment.

8 Discussion

The central finding of this thesis is that the timing of shade exposure, not merely its intensity or duration, determines how forage species perform in agrivoltaic systems, and that species differ significantly in whether they thrive from a lie-in or early bedtime. When four species were grown under a diurnal shade regime, delivering near-identical daily light integrals but differing in whether light reduction occurred in morning or afternoon periods (Figure 15), their biomass responses diverged significantly (Figure 19). Timothy increased biomass by 69% under afternoon shade relative to controls, exploiting the unshaded morning window like an early riser, while Italian ryegrass showed a 24% gain under the same treatment. By contrast, Clover and Perennial ryegrass showed no significant differences in biomass despite exhibiting pronounced morphological plasticity. Clover's slow stomatal kinetics (40 min) imposed carbon penalties during each transition, while Perennial ryegrass's fast kinetics (6.3 min) failed to translate to gains because its water-spending hydraulic strategy imposes costs under shade, continuing to lose water when light limits carbon gain, meaning that an early bedtime and an early start proved no more productive than a lie-in.

These results challenge the general assumptions in agrivoltaic research that shade tolerance can be predicted from responses to uniform reductions in light (Laub et al., 2022). Most studies evaluate shade tolerance through yield responses to uniform light reduction, quantifying how much light plants receive rather than when they receive it (Laub et al., 2022). The present findings demonstrate that performance depends on species-specific capacities to exploit the temporal structure of light availability: capacities rooted in the coordinated stomatal, structural, and hydraulic trait syndromes characterised under controlled glasshouse conditions (Figure 1 - Figure 11). This overlooked temporal dimension may explain why, despite the rapid expansion of agrivoltaics research, the understanding of underlying plant physiological mechanisms remains incomplete.

The difference between morning and afternoon shade responses reflects a fundamental asymmetry in how diurnal light regimes challenge plant carbon gain. The eight-fold variation in stomatal opening times observed across eight species in the glasshouse, ranging from approximately 5 minutes in Timothy to 40 minutes in Clover (Figure 4), translates into differential capacity to exploit temporally structured light environments. Although this range is narrower than the 25-fold range (0.9–23 min) reported by McAusland et al. (2016) and the 18-fold variation (7.4–133 min) documented by Deans et al. (2019a) across broader taxonomic groups, this range is still meaningful and demonstrates the kinetic diversity among the temperate forage species examined here. For Timothy, the fast 5-minute stomatal opening time means near-complete exploitation of morning light windows; for Clover, the 40-minute lag means a considerable part of each high-light period passes before stomata reach full operational conductance. In bifacial agrivoltaics, morning light combines with afternoon shade, replicating the unshaded morning window when leaves must transition from overnight darkness to full photosynthetic capacity, a process requiring coordinated stomatal opening and Rubisco activation (Carmo-Silva and Salvucci, 2013; Kaiser et al., 2015; Pearcy, 1990). Both stomatal responsiveness and photosynthetic capacity exhibit circadian regulation, with the speed and magnitude of stomatal responses declining as the day progresses (Matthews et al., 2017); the morning light/afternoon shade combination, therefore, aligns with leaves being in their most responsive state. By contrast, the pairing of morning shade and afternoon sunlight delays exposure to high light, condensing the window for carbon gain into a period when vapour pressure deficit typically peaks (Figure 15D) and stomatal conductance may be constrained by hydraulic limitations (Grossiord et al., 2020).

This interpretation reframes the concept of shade tolerance for agrivoltaic contexts. Clover reduced leaf mass per area by 36% under morning shade and 30% under afternoon shade (Figure 19C), consistent with classical shade-acclimation responses emphasising morphological plasticity: increased specific leaf area, altered chlorophyll content, and modified leaf angles, as mechanisms for

maintaining carbon balance under reduced irradiance (Valladares et al., 2007; Valladares and Niinemets, 2008). Clover's documented petiole elongation response allows leaves to position at canopy tops (Dennis and Woledge, 1982). However, this morphological flexibility yielded no biomass advantage. Liu et al. (2016) demonstrated across 280 species that specific leaf area (SLA) plasticity was not related to shade tolerance measured as the capacity to maintain biomass production, and that species with greater SLA plasticity showed worse biomass maintenance under shade, a finding replicated in the Clover response observed here. Those species that gained biomass, Timothy and Italian ryegrass, showed minimal structural adjustment but possessed the fastest induction kinetics in glasshouse trials (Figure 4). Ghalambor et al. (2007) differentiated between adaptive plasticity, in which phenotypes move toward new optima, and non-adaptive plasticity, which may move phenotypes further from optima. Clover's extensive structural response aligns with the latter, as an adjustment to diurnal shade that fails to address the key limiting factor, kinetic constraints during light transitions. This suggests performance in temporally heterogeneous light environments depends less on the capacity to modify leaf structure than on the kinetic properties that determine how quickly photosynthesis reaches full capacity following shade-to-sun transitions (Kaiser et al., 2017; Way and Pearcy, 2012).

Considering species differences within the generalists-versus-specialists framework provides additional insight. Clover and Perennial ryegrass behaved as generalists, exhibiting significant plasticity under both shade treatments but achieving no biomass gains, consistent with ecological studies that have shown species with greater plastic responses to light exhibit higher seedling mortality in deep shade (Liu et al., 2016; Valladares et al., 2007). By contrast, Timothy and Italian ryegrass responded selectively to afternoon shade, translating this response into substantial increases in biomass. DeWitt et al. (1998) identified lag-time limits as a fundamental constraint on plasticity: when environments change faster than plastic responses can track, morphological adjustment

provides no benefit. The diurnally structured light environment of fixed bifacial agrivoltaic systems represents a scenario in which kinetic specialisation outperforms morphological generalism.

8.1 Physiological Components Affecting Transient Carbon Gain

8.1.1 Multivariate Separation Reveals Distinct Kinetic Syndromes

Species occupied distinct positions in multivariate kinetic trait space (Figure 7), though species discrimination was weaker than for structural traits (R^2 = 0.53 versus 0.87 for hydraulic-anatomy), and not all pairwise comparisons achieved significance, indicating that kinetic traits exhibit greater within-species variability than anatomical properties. PC1 explained 35.4% of variance and captured a fast-slow kinetic continuum: grasses clustered toward the fast end of this axis, while Clover was isolated at the slow extreme, separated from all grass species by more than two standard deviations. The loadings revealed that stomatal opening time drove this primary axis of separation, with biochemical induction time and response magnitudes contributing secondarily. This multivariate pattern, in which species cluster by kinetic syndrome, indicates that coordination of trait combinations results in categorical differences in photosynthetic performance between functional groups.

As mentioned above, stomatal opening time varied 8-fold across species, from 5 min in Timothy to 40 min in Clover (Figure 4), with species identity explaining 60% of this variance. The grasses could be further separated into fast responders: Timothy, Perennial ryegrass, Cocksfoot, and Meadow fescue (5.0–6.6 min), and intermediate responders, Tall fescue, Italian ryegrass, and Hybrid ryegrass (10.9–12.5 min). This pattern of faster responses in grasses aligns with Vico et al. (2011), who reported that graminoids showed faster stomatal responses (3.9 ± 2.6 min) than forbs or woody species.

Biochemical induction time showed a different ranking among species than stomatal opening time (Figure 4B). While species differed significantly in biochemical induction (Figure 4B), the correlation between timing of stomatal and biochemical effects was only moderate (Figure 4C), and

among grasses, this coordination disappeared entirely. This independence reflects mechanistic differences: the opening of stomata requires changes in guard cell turgor that are governed by ion transport and interactions with subsidiary cells, whereas biochemical induction relies on the activation of Rubisco-by-Rubisco activase and the replenishment of metabolite pools in the Calvin-Benson cycle. (Kaiser et al., 2015). Sassenrath-Cole and Pearcy (1994) demonstrated that these processes unfold over distinct temporal phases: an initial stomatal limitation phase followed by a Rubisco activation phase, and coordination of the two would require selection to act on independent components of leaf molecular machinery. Way and Pearcy (2012) observed that when induction is slow, much of each sunfleck is spent below the potential assimilation rate. For Timothy, stomatal opening completes in 5 minutes while biochemical induction requires 7.3 minutes (Figure 4-Figure 5; Table S2), meaning stomata finish opening before Rubisco activates, inverting the typical limitation hierarchy. For Clover, both processes are slow, but stomatal opening (40 min) significantly exceeds biochemical induction (11.4 min), making stomata the unmistakable bottleneck (Table 3).

A significant finding is the dissociation between the magnitude and speed of coordination during photosynthetic induction. The strong correlation between the change in assimilation and stomatal conductance on induction (Figure 3C) indicates intrinsic linkage between carbon assimilation and water loss that scales across species, linked with how much they respond to light transitions. By contrast, the weak correlation between the time constants for assimilation and stomatal conductance (Figure 4C; Table 2) indicate these responses do not coordinate and suggest distinct regulatory mechanisms operating at different timescales. This timing decoupling suggests different rate-limiting steps: stomatal opening is constrained by guard cell mechanics, turgor dynamics and ion flux rates (Franks and Farquhar, 2007), while biochemical activation depends on Rubisco activase properties (Carmo-Silva and Salvucci, 2013). Taylor et al. (2020) previously demonstrated that the relative importance and timing of these limitations can vary between species.

8.1.2 Stomatal Limitation Dominates Carbon Costs During Induction

On induction, stomatal limitation differed significantly among species (Figure 8A), explaining 68% of among species variance in carbon costs, twice that explained by biochemical limitation (Figure 8C). Forgone assimilation ranged nine-fold across species, and interspecific variation was primarily driven by Clover's slow stomatal kinetics, consistent with Deans et al. (2019b) who found that stomatal opening time, not biochemical activation, dominated dynamic limitations across 15 angiosperm species. The functional link between kinetics and carbon costs emerged from the strong correlation between forgone assimilation and stomatal opening time ($\rho = 0.77$; Figure 8B): slow-opening species sacrifice more carbon because their stomata remain below steady-state conductance while assimilation proceeds sub-optimally (Way and Pearcy, 2012).

Clover's 40-min stomatal opening time (Figure 4A) produced the highest stomatal limitation values among all species tested (Figure 8A), despite Clover possessing the highest K_{leaf} (34.7 mmol m^{-2} s^{-1} MPa^{-1}; Figure 9B). This apparent paradox, highest hydraulic capacity paired with slowest stomatal response, may reflect the fundamental anatomical difference between kidney-shaped and dumbbell-shaped guard cells. Franks and Farquhar (2007) demonstrated that graminoid stomata achieve rapid aperture changes through osmotic see-sawing between guard cells and subsidiary cells, a mechanism they noted enables greatly accelerated stomatal opening and closure that might underlie the success of grasses. This mechanism is not available to dicot stomata lacking this subsidiary cell architecture. Clover's high hydraulic investment supports large steady-state fluxes (↑Δgsw = 0.38 mol m^{-2} s^{-1}; Figure 3B) but the kidney-shaped guard cells may not provide opportunities to accelerate the rate at which those fluxes are achieved. This explains why Clover achieved the highest photosynthetic capacity among all species (21.6 µmol m^{-2} s^{-1}; Figure 2A) yet failed to translate this potential into biomass gains under temporally structured shade; the kinetic penalty accumulated over repeated transitions overwhelmed the steady-state advantage.

The noticeable asymmetry between stomatal opening and closing kinetics observed in Clover (ratio 5.1) versus the grasses (ratios 0.26–0.92; Figure 6B) likely reflects differences in guard cell mechanics. The absence of correlation between opening and closing times across all species (Figure 6A) indicates that these processes are mechanistically decoupled. McAusland et al. (2016) reported that the opening and closing rates for species possessing dumbbell-shaped guard cells were moderately correlated (R^2 = 0.52) but weaker in elliptical species (R^2 = 0.29), suggesting similar mechanisms control grass responses. Unlike grasses, Clover possesses anomocytic stomata, which lack differentiated subsidiary cells (Rashid et al., 2018); therefore, they cannot utilise the rapid ion shuttling mechanism (Franks and Farquhar, 2007). Stomatal opening requires the uptake of potassium ions, whilst closing depends on the release of potassium anions (Lawson and Blatt, 2014). This asymmetry limits both the opening and closing speeds of stomatal responses; for species like Clover, therefore, slow opening cannot be offset by intermediate closing rates, compounding the kinetic penalty under fluctuating light.

Although stomatal limitation dominated interspecific variation in forgone assimilation during induction (Figure 8A), not all species conformed to this pattern. Timothy and Cocksfoot, the fastest stomatal responders, were instead limited by biochemical activation, with their stomata opening more rapidly than photosynthesis could activate (Table 3). Timothy's stomata completely opened in approximately 5 minutes (Figure 4A), paired with biochemical induction over 7.3 minutes (Figure 4B). Sassenrath-Cole and Pearcy (1994) established the canonical temporal hierarchy of limitations: ribulose-1,5-bisphosphate regeneration limits for the first 1-2 minutes, Rubisco activation becomes limiting for 1-10 minutes, and stomatal limitation dominates thereafter. For Timothy, Cocksfoot, and Meadow Fescue, stomata open faster than biochemical capacity activates, meaning the rate-limiting step becomes biochemical rather than stomata. This finding challenges the improvement of dynamic performance through stomatal manipulation alone (Lawson and Vialet-Chabrand, 2019), and supports

the idea that both stomatal and biochemical traits should be considered in dynamic light environments (Taylor et al., 2020).

8.1.3 Partial Coupling Between Stomatal Speed and Capacity

Stomatal response magnitude and opening time showed a moderate positive correlation (ρ = 0.46; Figure 4), explaining approximately 21% of variance and indicating partial coupling between these traits. This relationship reflects a biophysical constraint, whereby larger aperture changes require greater ion flux across guard cell membranes, which takes longer to achieve (Lawson and Blatt, 2014; Lawson and Vialet-Chabrand, 2019). This coupling weakened among grasses alone (ρ = 0.32), possibly due to the mechanical advantages of subsidiary cell osmotic exchange that permit faster ion shuttling regardless of magnitude (Franks and Farquhar, 2007). Species within the intermediate kinetic range (8–15 min) exhibited the full spectrum of response magnitudes (Figure 3B), indicating that factors beyond aperture size modulate opening speed.

The functional consequence of this coupling is extended asynchrony between stomatal conductance and photosynthetic demand. Lawson and Vialet-Chabrand (2019) noted that sluggish stomata cause non-synchronous behaviour between assimilation and conductance, reducing intrinsic water-use efficiency under dynamic conditions. However, the incomplete nature of this relationship; with 79–90% of variance unexplained, indicates that other factors modulate opening speed independently of magnitude.

8.1.4 Biochemical Limitation Dominates During De-induction

The transition from high to low light revealed a reversal in the hierarchy of limitations. While stomatal limitation dominated during induction (Figure 8A), biochemical limitation ($\downarrow F$) was greater in magnitude than stomatal limitation ($\downarrow F_s$) during de-induction for all species (Figure 8 E-F). Species differed significantly in both stomatal closing time (Figure 5A) and biochemical relaxation time (Figure

5B), but critically, these two processes were not coordinated with respect to their duration (Figure 5C). As for induction processes, this independence indicates that stomatal closure and Calvin-Benson cycle down-regulation operate on different timescales controlled by distinct mechanisms (Kaiser et al., 2017).

Biochemical costs during de-induction were remarkably conserved across species, ranging only from 411 to 653 μmol m^{-2} (1.6-fold; Figure 8E) despite the large variation in stomatal properties (9-fold range in ↑Fs). This conservation, compared to the 9-fold range in stomatal-limited forgone assimilation during induction, suggests that Rubisco deactivation kinetics are constrained by fundamental enzyme properties shared across species. Mott and Woodrow (2000) modelled the time constant for Rubisco activation as typically 1-5 minutes, depending on species, reflecting constraints on Rubisco activase concentration and activity, while Carmo-Silva and Salvucci (2013) demonstrated that Rubisco activation state decreased from approximately 90% to 50-70% upon high-to-low light transition. This independence was confirmed by multivariate analysis, where ↓*F* loaded onto a separate axis from stomatal and hydraulic traits (Figure 11). For species selection, this decoupling means that stomatal architecture does not constrain de-induction costs, making induction kinetics, not de-induction, the primary axis along which species differentiate for fluctuating light performance.

8.1.5 Steady-State Capacity Does Not Predict Dynamic Performance

Steady-state photosynthetic capacity varied 1.4-fold across species, from Timothy (15.4 μmol m^{-2} s^{-1}) to Clover (21.6 μmol m^{-2} s^{-1}), with grasses forming a continuous gradient and Clover positioned only marginally above the highest-performing grass, Tall Fescue (20.8 μmol m^{-2} s^{-1}; Figure 2A). Under low light, however, this hierarchy collapsed: interspecific differences diminished and statistical separation disappeared (Figure 2B), indicating that differentiation of species under fluctuating conditions depended more on the capacity to exploit periods of high-light than on low-light efficiency. The high-light hierarchy reflects species positioning along the leaf economics spectrum, where quick-

return species with high nitrogen content achieve high photosynthetic rates (Wright et al., 2004). Rubisco's low catalytic efficiency requires 20–30% of leaf nitrogen investment (Irving, 2015), establishing the strong correlation between photosynthetic capacity and leaf nitrogen concentration characteristic of C_3 species (Evans, 1989). Clover's position at the top of this hierarchy is consistent with the legume nitrogen advantage: symbiotic nitrogen fixation typically enables legumes to maintain higher leaf nitrogen concentrations than grasses, dependent on soil nitrogen availability (Adams et al., 2016). However, this steady-state advantage translated to no field benefit under temporally structured shade; Clover's kinetic constraints overwhelmed its capacity advantage (Figure 19).

The integration of hydraulic traits with carbon economics along the fast-slow continuum described by (Reich, 2014) and the constraint of global plant trait space into a two-dimensional plane identified by Diaz et al. (2016) provides additional context: species with acquisitive trait syndromes achieve rapid carbon gain under favourable conditions. However, they may lack the kinetic responsiveness required for fluctuating environments. Mott and Woodrow (2000) demonstrated through modelling that optimal nitrogen allocation between Rubisco and Rubisco activase depends on the light environment, favouring greater investment. Similarly, Kaiser et al. (2015) identified Rubisco activase and stomatal conductance as targets for improvement of photosynthesis of plants in fluctuating irradiance, suggesting that selection for high steady-state capacity may have traded off against dynamic responsiveness.

Timothy, despite possessing the lowest steady-state assimilation among the species tested (15.4 µmol m^{-2} s^{-1}; Figure 2A), exhibited the fastest induction kinetics (5 min; Figure 4A). Conversely, Clover's high photosynthetic ceiling (21.6 µmol m^{-2} s^{-1}) was undermined by the slowest stomatal responses (40 min), creating a mismatch between potential and realised carbon gain under fluctuating conditions. The strong correlation between steady-state high-light assimilation and induction magnitude (Table 5) confirms that species with higher photosynthetic capacity achieve larger absolute

responses during induction, but says nothing about the rate at which they approach this capacity. Soleh et al. (2017) found no significant correlation between maximum photosynthetic rate and cumulative CO_2 fixation during induction in soybean genotypes, while Acevedo-Siaca et al. (2020) showed that steady-state capacity does not predict the speed of convergence to that capacity. Because most studies report steady-state values and miss dynamic behaviour (Lawson and Blatt, 2014), screening based solely on maximum photosynthetic rates would favour Clover over Timothy, yet field performance under temporally structured shade reversed this ranking.

8.2 Structure-Kinetics Relationships Are Functional-Group Specific

8.2.1 Structural Traits Define Multivariate Positions

Species separation was strongest in structural-hydraulic trait space (Figure 9), with PC1 and PC2 together explaining 80.6% of variance; substantially more than the kinetic PCA (57.1%; Figure 7). Clover separated from all grasses by more than four standard deviations along PC1, a categorical rather than continuous distinction. This pattern indicates that anatomy and hydraulics, which are fixed mainly during development, generate greater interspecific differentiation than dynamic traits, which show more within-species variation due to environmental plasticity (Siefert et al., 2015). For species selection, anatomy provides reliable markers of functional type, while kinetic measurements require careful standardisation.

PC1 (61.3% of variance) integrated leaf hydraulic conductance (loading 0.96), total stomatal density (0.92), normalised stomatal distribution index (−0.91), and guard cell length (−0.85) into a coherent functional syndrome. One proposed explanation for this coordination is the unified cell size hypothesis, in which developmental constraints link guard cell dimensions to vein density and other cellular infrastructure (Brodribb et al., 2013). The exceptional explanatory power of this axis, the highest among all principal component analyses performed, indicates that species identity is encoded more strongly in anatomical coordination than in any single trait.

PC2 (19.3% of variance) captured leaf construction strategy, with leaf mass per area loading positively (0.85) and leaf water potential loading negatively (−0.51). Clover combined the least negative water potential (−0.18 MPa) with the lowest LMA, positioning it at the acquisitive extreme. At the same time, high-LMA grasses, such as Tall Fescue, operated at more negative water potentials. This separation aligns with the leaf economics spectrum, where conservative species with thicker leaves show lower mass-based photosynthetic rates and longer leaf lifespans (Wright et al., 2004). Among grasses, this axis distinguished resource-acquisition strategies independent of the hydraulic-stomatal syndrome captured by PC1.

Clover occupied the extreme of PC1, combining the highest leaf hydraulic conductance (34.7 mmol m^{-2} s^{-1} MPa^{-1}; Figure 9B) with the smallest guard cells (21.9 µm; Figure 9E) and exclusive hypostomaty (NSD = −1.00; Figure 9F). This structural combination, high hydraulic capacity with small, abaxially-restricted stomata, represents a fundamentally different functional type from the grasses. Hypostomaty predominates in broad-leaved dicots, while amphistomy characterises high-light herbaceous growth forms (Muir, 2018). Clover's hypostomatous arrangement may optimise gas exchange for its horizontal leaf display, but appears maladaptive in the diurnal shade regime of fixed bifacial agrivoltaic environments.

Grasses exhibited the inverse structural combination (Figure 9): lower leaf hydraulic conductance (6.7–18.2 mmol m^{-2} s^{-1} MPa^{-1}), larger guard cells (31.3–51.0 µm), and consistent amphistomaty (NSD = +0.26 to +0.87). This coordination reflects the fundamental link between hydraulic supply and stomatal demand: maximum stomatal conductance and leaf hydraulic conductance are strongly correlated (r^2 = 0.80) across species (Brodribb and Jordan, 2008), while leaf hydraulic conductance varies more than 65-fold globally and coordinates with maximum gas exchange rates within life forms (Sack and Holbrook, 2006). Among the grasses examined here, this supply-

demand coordination operated within the dumbbell guard cell architecture that enables rapid aperture adjustment.

Stomatal distribution varied substantially among grasses, from Timothy's relatively even allocation across leaf surfaces (NSD = +0.26) to Perennial Ryegrass's strong adaxial bias (NSD = +0.87). In wheat, the adaxial surface makes substantial contributions to gas exchange under high light, where it receives direct illumination, with each surface operating semi-independently (Wall et al., 2022). However, higher adaxial stomatal density is associated with lower grain yield in spring wheat, indicating that extreme adaxial bias may incur water costs that offset kinetic advantages (Samantara et al., 2025). Timothy's intermediate position, maintaining substantial stomatal densities on both surfaces, may represent a favourable balance between rapid light responsiveness and distributed water loss under the directional shade of agrivoltaic systems.

8.2.2 Excluding Clover Reveals Correlations Between Stomatal and Hydraulic Traits Among Grasses

Across all species, no correlation was observed between GCL and stomatal opening time, whereas among grasses alone, larger guard cells opened significantly slower (Table 5). This obscured pattern arose because Clover combined the smallest guard cells (21.9 µm) with the slowest kinetics (40 min), a combination opposite to the grass trend, effectively flattening the overall trend. Kardiman and Ræbild (2018) demonstrated a similar size-speed relationship in tropical hardwood trees, Tectona, where smaller stomata opened faster, while Elliott-Kingston et al. (2016) found no correlation between stomatal size and closing rate across species with mixed guard cell types. The distinction is critical: within a single guard cell type (dumbbell), the mechanical relationship between pore geometry and aperture change rate produces predictable size-speed correlations; across guard cell types, these relationships are obscured by fundamentally different operating mechanisms (McAusland et al., 2016). Lawson and Blatt (2014) attributed faster kinetics to higher stomatal density and smaller

guard cell size, noting that the greater surface-area-to-volume ratio presumably facilitates solute exchange with neighbouring cells. For Timothy (GCL = 31.7 µm) and Cocksfoot (GCL = 31.3 µm), small guard cells contribute to their fast kinetics; for Clover (GCL = 21.9 µm), even smaller guard cells cannot overcome the fundamental constraint imposed by kidney-shaped architecture.

K_{leaf} showed a similar pattern. Across all species, K_{leaf} showed no relationship with stomatal opening time (Table 5); another relationship obscured by Clover's anomalous position. Among grasses alone, higher K_{leaf} was associated with faster stomatal opening (Table 5), suggesting that hydraulic supply capacity facilitates kinetic performance when guard cell architecture is held constant. Species with high K_{leaf} can sustain the water flux required for rapid guard cell swelling without declines in leaf water potential (Buckley, 2005). Furthermore, Sack and Holbrook (2006) documented that K_{leaf} varies more than 65-fold across species and co-ordinates with maximum gas exchange rates. Brodribb and Jordan (2008) quantified this coordination (R^2 = 0.80) across eight species, while Brodribb et al. (2005) reported R^2 = 0.87 across 20 species. Brodribb et al. (2017) demonstrated that K_{leaf} directly limits stomatal kinetics in species where hydraulic delivery to guard cells constrains the rate of turgor change, and it has further been shown that K_{leaf} is coordinated with both stomatal and mesophyll conductance (Xiong and Nadal, 2020), suggesting that hydraulic architecture constrains the entire gas exchange pathway.

The kinetic differences observed among the grasses studied here align with previous studies investigating hydraulic regulation strategies in forage species. Holloway-Phillips and Brodribb (2011a) showed that Italian ryegrass maintains more conservative stomatal regulation than Tall Fescue, with smaller safety margins (+0.11 to −0.21 MPa versus −0.90 to −0.95 MPa). In this study, species-level differences were evident in contrasting closing kinetics: Italian Ryegrass closed its stomata fastest among all species (t_{63} = 13.3 min), whereas Tall Fescue was among the slowest (t_{63} = 34.4 min). Tall Fescue also exhibited the lowest K_{leaf} (6.7 mmol m^{-2} s^{-1} MPa^{-1}) and most negative ψ_{leaf} (−0.57 MPa),

consistent with Holloway-Phillips and Brodribb's (2011a) finding that this species operates closer to hydraulic limits with less sensitive stomatal regulation.

The relationship between GCL, K_{leaf} and dynamic performance can be explained by guard cell architecture. Among the grasses, dumbbell-shaped guard cells with subsidiary cells enable the rapid exchange of ions that accelerate turgor changes beyond what water supply alone permits (Franks and Farquhar, 2007). Clover had the highest K_{leaf} of all species studied (34.7 mmol m^{-2} s^{-1} MPa^{-1}; Figure 9), placing it within the upper ranges observed within angiosperms (3.9–36 mmol m^{-2} s^{-1} MPa^{-1}; Brodribb et al., 2005); however, it exhibited the slowest kinetics ($t_{63}(g_{sw})$ ~ 40 min). This demonstrates that hydraulic potential cannot compensate for the structural constraints that govern ion flux at the guard cell level (Franks and Farquhar, 2007).

Adaxial stomatal density was the only correlation robust to Clover's inclusion. Across all species, higher adaxial stomatal density was associated with faster opening (Table 5), and this relationship remained significant, though weakened, among grasses alone. This correlation connects to the variation in the distribution of stomata between the leaf surfaces among grasses (NSD index): Timothy, with the most even stomatal distribution (+0.26), maintains substantial populations on both surfaces, while Perennial ryegrass concentrates stomata adaxially (+0.87). Sakoda et al. (2020) demonstrated that higher stomatal densities led to faster photosynthetic induction due to higher initial stomatal conductance, with moderate increases in stomatal density yielding 25.6% greater biomass under fluctuating light. The robust adaxial density-kinetics correlation may reflect a spatial hydraulic constraint: stomata distributed across both leaf surfaces (higher adaxial stomatal density and thus amphistomaty) experience more uniform access to mesophyll water pools and shorter hydraulic path lengths to the epidermis. Drake et al. (2019) demonstrated that amphistomatous leaves achieved 50% higher maximum stomatal conductance than hypostomatous leaves at equivalent total stomatal density, attributing this advantage to shorter carbon dioxide diffusion paths. In wheat, Wall

et al. (2022) found that adaxial stomata opened faster in response to light increases than abaxial stomata; meanwhile, Hõrak (2025) noted that adaxial and abaxial stomata differ in their ion channel composition (AKT1 and KAT1, respectively), contributing to their functional differentiation. This finding supports the adaxial stomatal density-kinetics correlation observed here: species with more adaxial stomata may benefit from faster-responding stomatal populations on this surface. The evenness of stomatal distribution between leaf surfaces in the fast-responding Timothy means that roughly half its stomata are these faster adaxial types. A higher proportion of stomata on adaxial surfaces is not, however, the whole story. Perennial ryegrass's strong adaxial bias (hyperstomy) would suggest most of its stomata are the faster type, but Timothy achieved the fastest opening times overall, indicating that guard cell architecture and other traits interact with stomatal distribution to determine kinetic performance. Timothy's kinetic advantage over Perennial ryegrass may be contributed to be the smaller size of its guard cells (Kardiman and Ræbild, 2018), which is thought to enable faster ion flux (Lawson and Blatt, 2014).

8.2.3 Integrating Dimensions of Variation

The three principal component analyses performed across the glasshouse dataset reveal complementary dimensions of interspecific variation that together characterise the functional strategies available within this assemblage of forage species. The hydraulic-anatomy analysis (Figure 10) achieved the highest species discrimination ($R^2 = 0.86$), reflecting the stability of structural traits, while the kinetics analysis (Figure 7) showed lower explanatory power ($R^2 = 0.52$), indicating greater within-species variability in dynamic responses. The efficiency-anatomy integration (Figure 11; $R^2 = 0.69$) bridged these dimensions by demonstrating how structural investment translates into carbon costs during light transitions. De Bello et al. (2009) found that within-community functional diversity was lower than expected at random, with much of the total leaf economy variation occurring among coexisting species, the finding that species differentiate more strongly in structural than kinetic traits align with this pattern.

The efficiency-anatomy PCA (Figure 11) integrated eleven traits combining structure, hydraulics, and dynamic cost metrics, which identified three distinct dimensions of species differentiation. The majority of variance was associated with stomatal-hydraulic syndromes, with high leaf hydraulic conductance and stomatal density (0.92) aligning with greater forgone assimilation due to stomatal limitation during induction ($\uparrow F_s$). This suggests that investments in hydraulic capacity and stomatal density incur correspondingly larger transient carbon penalties when stomata lag behind biochemistry during light transitions. Orthogonal to this was an efficiency-cost axis that suggested an association between intrinsic water-use efficiency and forgone CO_2 attributed to biochemical factors during induction and stomatal factors during de-induction. This reflects the well-documented asynchrony between stomatal and photosynthetic kinetics: Lawson and Vialet-Chabrand (2019) demonstrated that slower stomatal responses relative to biochemistry cause at least a 20% reduction in iWUE, which also incurs transition costs during transitions. Notably, LMA was positively associated with higher iWUE and greater biochemical limitation during both induction and de-induction, consistent with the role of LMA in integrating multiple dimensions of leaf economics.

Timothy achieved the highest water-use efficiency among all species, despite moderate hydraulic capacity, whilst Clover exhibited the opposite pattern: the highest hydraulic capacity, paired with the lowest water-use efficiency (Figure 11), which reflects the kinetic asynchrony during de-induction. When light decreased, Clover's assimilation dropped rapidly, but its stomata remained open (Figure 6), a mismatch that wastes water without carbon gain. By contrast, Timothy's biochemical and stomatal responses were more coordinated, minimising water loss during light transitions. Perennial Ryegrass exhibited an intermediate strategy: fast stomatal opening (t_{63} = 6.3 min) but a water-spending strategy that maintains conductance despite declining water status (Holloway-Phillips and Brodribb, 2011b), rather than optimising for specific temporal light regimes.

The grasses studied here exhibit anisohydric (water-spending) hydraulic behaviour. Anisohydric species keep their stomata open even as leaf water status declines, prioritising carbon gain over hydraulic safety. Holloway-Phillips and Brodribb (2011a) demonstrated this in Perennial ryegrass: stomata remained open until leaf water potential reached −2.35 MPa, well below the −1 MPa threshold at which the leaf's water transport system begins to fail (P_{50}), accepting hydraulic damage to maintain gaseous exchange. Holloway-Phillips and Brodribb (2011b) demonstrated this further, finding that this risky strategy maximised water-use efficiency in forage grasses. Sperry (2000) established the foundational framework linking hydraulic conductance to gas exchange: stomatal conductance and transpiration are positively correlated with soil-to-leaf hydraulic conductance, with stomatal responses to experimental reductions in hydraulic conductance occurring within 15 minutes. Additionally, Grossiord et al. (2020) identified leaf water potential and K_{leaf} as major controls of stomatal response to vapour pressure deficit.

Collectively, the multivariate analyses support a framework distinguishing generalist from specialist strategies with respect to shade. Generalists, exemplified by Clover and to a lesser extent Perennial ryegrass, maintain the capacity to respond morphologically and physiologically to diverse environmental conditions but pay costs in terms of slow kinetic responses and delayed adjustment to diurnal light regimes. Specialists, exemplified by Timothy, possess fast kinetics suited to exploiting specific temporal patterns but show limited morphological plasticity when conditions change. This distinction echoes the broader ecological literature on specialist-generalist trade-offs (Valladares et al., 2007) and the recognition that low plasticity associated with a conservative resource-use strategy may be adaptive (Valladares and Niinemets, 2008). The consistency between laboratory and field phenotypes, while significant, remains modest, Poorter et al. (2016) reported a median R^2 of 0.26 for lab-field correlations, reinforcing the importance of field validation.

8.3 Field Validation: Temporal Shade Timing Determines Performance Outcomes

8.3.1 Microclimate: Shade Treatments Achieved Intended Light Regimes

The 39-day field experiment at Hazelrigg provided the critical test of whether glasshouse-characterised kinetic traits predict performance under realistic agrivoltaic conditions. The shade treatments successfully created the intended temporal light regimes (Figure 14 - Figure 16). Morning shade reduced morning PAR by 47%, while afternoon PAR was unaffected; conversely, afternoon shade reduced afternoon PAR by 50% without affecting morning PAR. Afternoon shade thus reversed the natural diurnal light pattern, creating conditions where morning PAR exceeded that in the afternoon by 185 µmol m^{-2} s^{-1}, in a context where average diurnal maxima were c. 1000 µmol m^{-2} s^{-1} and where afternoon PAR exceeded morning PAR in the control treatment. Total daily light integral reductions were comparable across treatments: −25% for morning shade versus −28% for afternoon shade (Figure 15 and supplementary), indicating that differential biomass responses reflected the timing rather than the total quantity of light reduction. The findings of Poorter et al. (2019), whose meta-analysis of 70 traits ranging from molecules to whole plant performance established dose-response relationships against daily light integral, helps frame these results: most structural and allocation traits show non-linear responses to daily light integral, with the steepest responses occurring below approximately 10 mol m^{-2} d^{-1}. The daily light integral reductions imposed in the present study occurred within the range where trait responses to light quantity alone should be modest.

VPD differed significantly between treatments and interacted with the morning-afternoon asymmetry (Figure 15D). Morning shade reduced VPD during the morning period, while the morning sun-afternoon shade combination increased morning VPD to the highest values recorded (0.62 kPa). Morning light when the VPD is low enables rapid stomatal opening without hydraulic constraint (Sturchio et al., 2022). Sturchio et al. (2024a) confirmed this advantage within agrivoltaic systems and

semiarid environments: plants exposed primarily to morning light maintained higher stomatal conductance and less negative leaf water potential, resulting in +33% aboveground net primary productivity. Barron-Gafford et al. (2019) documented VPD reductions of 0.52 kPa under agrivoltaic panels, emphasising the potential of these systems to modify the microclimate. For Timothy, afternoon shade may have preserved the low-VPD morning window when its fast kinetics could be fully exploited; for Clover, slow kinetics meant the favourable VPD conditions may have passed before stomata reached operational conductance. However, the VPD differences observed in this study (0.05–0.25 kPa between treatments) were considerably smaller (4–10×) than those reported by Barron-Gafford et al. (2019), and occurred within a temperate UK environment where VPD is already low. Further research is needed to establish whether biomass responses observed in this study were driven primarily by the diurnal timing of light availability and plant circadian rhythms (Resco de Dios, 2017; Sellaro et al., 2012), rather than VPD-mediated effects on water use, which should have been relatively marginal.

8.3.2 Multivariate Field Patterns Confirm Species Dominance

The field experiment confirmed the dominance of species identity over treatment effects (Figure 17). Variance partitioning assigned approximately 88% of the variation to species identity, compared with only 4% to treatment effects. This is consistent with the meta-analytic finding of Siefert et al. (2015) that approximately 75% of trait variation occurs among rather than within species, with the findings of Funk et al. (2017), who reported approximately 70% interspecific versus 30% intraspecific variation across functional trait datasets, and with results from Poorter et al. (2012) that demonstrated environmental variables explain only 10–30% of biomass allocation variation, with species identity dominating variance structure.

8.3.3 Species Biomass Responses Align With Speeds of Leaf Gas Exchange Responses to Shade

Timothy increased biomass by 69% under afternoon shade (Figure 19H) despite showing minimal structural plasticity across treatments. Timothy's 5-minute stomatal opening time (Figure 4) enabled near-complete exploitation of the unshaded morning window. Each dawn presented a high-light window that Timothy could access within minutes, while slower species remained kinetically limited as the light opportunity passed. Over the 6-week growth period, it appears these daily kinetic advantages compounded into the substantial biomass differential observed. Sakoda et al. (2020) demonstrated that higher stomatal density resulted in faster photosynthetic induction owing to the higher initial stomatal conductance and that the Arabidopsis epf1 mutant, with a moderate increase in stomatal density, achieved 25.6% greater biomass production than wild type under fluctuating light. Timothy's relatively high stomatal density on the adaxial surface (Figure 9), combined with fast guard cell responses, is analogous. The absence of structural adjustment in Timothy may reflect there being little to drive morphological plasticity when physiological responses are capable of matching environmental challenges.

Like Timothy, Italian ryegrass showed a positive, though smaller, biomass response (+24%) under afternoon shade relative to morning shade (Figure 19H). placing it among the slower-responding grasses rather than the fast group. However, Italian ryegrass's stomatal carbon cost during induction (↑Fs ≈ 800 µmol m^{-2}) was approximately four-fold lower than Clover's (↑Fs ≈ 3238 µmol m^{-2}; Figure 8A), indicating that intermediate kinetics need not impose prohibitive carbon penalties. Italian ryegrass also exhibited a selective multivariate response, shifting significantly only under afternoon shade ($d = 1.14$, $p < 0.01$) while showing no significant shift under morning shade (Figure 18). This selectivity contrasts with Perennial ryegrass, which shifted under both treatments yet gained no biomass. Holloway-Phillips and Brodribb (2011a) demonstrated that L. multiflorum exhibits conservative stomatal regulation with a near-zero safety margin (+0.11 to −0.21 MPa), in marked

contrast to Perennial ryegrass's water-spending strategy (−1.35 MPa). This conservative regulation may explain why Italian ryegrass converted its selective response into biomass gain, while Perennial ryegrass's generalist response yielded no benefit. Italian ryegrass showed pronounced leaf area plasticity (+38% under afternoon shade; Figure 19A), which may also have contributed to these responses. Marrou et al. (2013b) demonstrated that lettuce maintained yield under moderate shade through increased total leaf area despite reduced leaf number, a morphological compensation strategy that Italian ryegrass appears to share.

Perennial ryegrass showed no significant biomass response to either shade treatment (Figure 19H), despite exhibiting moderate structural plasticity (−28% LMA under morning shade, −20% under afternoon shade; Figure 19C). Yet in PCA space, Perennial ryegrass exhibited the clearest multivariate response to shade treatments (Figure 17). Ehret et al. (2015) documented that White Clover proportion increased under shade relative to Perennial ryegrass, with Perennial ryegrass showing greater reduction in photosynthetic rate under shade than White Clover. Perennial ryegrass's fast stomatal opening (6.3 min), while comparable to Timothy (5 min), did not translate to biomass gains, likely because its water-spending hydraulic strategy (described above) imposes costs under shade, continuing to lose water when light limits carbon gain. Poorter et al. (2012) noted that species groups explain more variation than environment for biomass allocation; the multivariate trait response without biomass consequence suggests that Perennial ryegrass adjusted its trait integration strategy without affecting the net outcome for growth. Perennial ryegrass's water-spending hydraulic strategy may impose costs under the combined water and light stress of shade treatments, offsetting any benefit from its moderate opening speed. Furthermore, Perennial ryegrass's extreme adaxial stomatal concentration (NSD = +0.87) may amplify these hydraulic costs by concentrating evaporative demand on a single leaf surface rather than distributing water loss across both surfaces as in Timothy (NSD = +0.26); Samantara et al. (2025) demonstrated that higher adaxial stomatal density was associated with

lower grain yield in spring wheat, with the penalty greater under high vapour pressure deficit conditions

Clover's failure to convert high plasticity into biomass gain under either treatment represents the study's most instructive negative result. Despite exhibiting the largest specific leaf area plasticity (−35% under morning shade, −30% under afternoon shade; Figure 19C) and the highest leaf hydraulic conductance (K_{leaf} = 34.7 mmol m^{-2} s^{-1} MPa^{-1}; Figure 9B), Clover showed no significant biomass response to temporal shade manipulation (Figure 19H). Its 40-min stomatal opening time may have imposed carbon penalties during each shade-to-sun transition that accumulated over the growth period, overwhelming any benefits derived from structural adjustment.

In contrast to the pronounced plasticity in leaf structural and biomass traits, stomatal morphology exhibited more constrained and surface-specific responses to shade treatments (Figure 19D–G). Although species × treatment interactions were significant for both guard cell length and stomatal density, pairwise comparisons revealed minimal within-species adjustment. Adaxial stomatal density showed no significant differences within any species despite the significant overall interaction (Figure 19E), and abaxial guard cell length likewise showed no significant within-species effects (Figure 19F). Only Clover and Timothy showed significant reductions in abaxial stomatal density under shade, while the ryegrasses remained unchanged (Figure 19G). This pattern aligns with the plasticity indices reported by Poorter et al. (2019) who found stomatal density has relatively low plasticity (PI = 1.8) compared to structural traits such as specific leaf area (PI = 2.6) and tillering (PI = 5.0). The constrained plasticity of stomatal anatomy carries a critical functional consequence: the guard cell architecture that determines opening kinetics, and thus the carbon costs quantified in the glasshouse experiment, remains largely fixed regardless of shade treatment. DeWitt et al. (1998) identified developmental range limits as a fundamental constraint on plasticity; stomatal anatomy, established during early leaf development, may represent such a limit. This explains why Clover's extensive structural plasticity

failed to translate into biomass gains; while specific leaf area can adjust within weeks, the slow stomatal kinetics imposed by the kidney-shaped guard cells of Clover persisted throughout the experiment, compounding carbon losses with each shade-to-sun transition.

8.4 Plasticity-Performance Paradox: Why Structural Adjustment Failed to Compensate

Clover exhibited the most significant structural plasticity among species across treatments but gained no biomass advantage. Ghalambor et al. (2007) provide a theoretical context for understanding this, arguing that only adaptive plasticity that places populations close to a new phenotypic optimum predictably enhances fitness. Non-adaptive plasticity, plasticity that shifts phenotypes further from the optimum or fails to address the actual limiting factor, provides no fitness benefit regardless of its magnitude. Liu et al. (2016) extended the Ghalambor et al. (2007) framework using biomass as a measure of plant performance in a meta-analysis of 280 species. They found that species with greater SLA were less, not more, able to maintain biomass under shade. Clover's 35% increase in specific leaf area under morning shade (Figure 19C) did not translate into any biomass benefits, which aligns with this framework.

Clover's plasticity appears non-adaptive in this framework. Its specific leaf area increases under shade, representing a classic shade-acclimation response, thinner leaves with greater light capture area per unit mass investment, but failed to address kinetic constraints during light transitions. Under temporally fluctuating light, morphological adjustment to steady-state shade is maladaptive (DeWitt et al., 1998) because the environment repeatedly alternates between conditions for which the phenotype is optimised (shade) and conditions for which it is suboptimal (sun). There are costs in terms of forgone assimilation associated with each transition because of Clover's slow kinetics, that adjustment to specific leaf area does not offset. Poorter et al. (2019) conducted a meta-analysis of plant responses to light intensity for 70 traits across 500 experiments and 760 species, finding that plasticity differences among species groups were generally small compared with the

overall responses to daily light integral. The magnitude of plasticity observed here falls within normal ranges and cannot be considered unusually high or low.

8.5 Integrating Outcomes from the Glasshouse and Field

While field validation focused on four species (Timothy, Italian ryegrass, Perennial ryegrass, and Clover), the glasshouse experiment characterised eight species spanning the full kinetic and structural spectrum. The four additional species, Cocksfoot, Meadow fescue, Tall fescue, and Hybrid ryegrass, provide context for interpreting both the mechanisms underlying field responses and the generalisability of structure-kinetics relationships.

Cocksfoot exhibited the second-fastest stomatal opening time (6.6 min; Figure 4A), approaching Timothy's rapid kinetics. Its structural profile, moderate K_{leaf} (12.4 mmol m^{-2} s^{-1} MPa^{-1}; Figure 9B), intermediate guard cell length (31.3 µm; Figure 9E), and amphistomaty, positioned it within the fast-kinetic grass cluster in multivariate space (Figure 7). Based on the glasshouse-derived kinetic ranking, Cocksfoot would be predicted to respond positively to afternoon shade treatment in field conditions, a prediction that remains untested but follows directly from Timothy's response. Peri et al. (2002b) reported that the rate of change of stomatal conductance in Cocksfoot was slower than for photosynthesis both when entering shade and during subsequent induction, but described the species as shade-tolerant from a physiological perspective, a classification that may reflect steady-state tolerance rather than dynamic performance.

Tall fescue showed the lowest K_{leaf} among grasses (6.7 mmol m^{-2} s^{-1} MPa^{-1}; Figure 9B) and occupied a distinct position in structural-hydraulic PCA space, separated from other grasses along both PC1 and PC2 (Figure 10). Its 15-min stomatal opening time placed it among the slower grasses (Figure 4A), but its low K_{leaf} violated the grass-specific correlation between higher K_{leaf} and faster opening (Table 5). Tall fescue thus represents a potential outlier within the grass functional group, a species whose hydraulic-kinetic coordination deviates from the general grass pattern. This outlier status has

implications for trait-based screening: LMA or stomatal density alone would fail to predict Tall fescue's kinetic performance because its hydraulic architecture imposes constraints not captured by surface traits.

Meadow fescue and Hybrid ryegrass (Lolium × hybridum) occupied intermediate positions across all measured traits. Their moderate kinetics (10–12 min opening; Figure 4A), moderate hydraulic conductance, and intermediate stomatal dimensions placed them as intermediate in both kinetic and structural PCAs (Figure 7Figure 10Figure 11). This makes them useful reference species for standardising structure-kinetics relationships; they conform to grass-typical patterns without exhibiting the extreme values of Timothy (fastest), Tall fescue (lowest K_{leaf}), or Italian ryegrass (largest guard cells). For breeding programs seeking to shift kinetic performance within a grass species, Meadow fescue and Hybrid ryegrass represent starting points from which selection could proceed in either direction along the fast-slow continuum.

8.6 Implications for Agrivoltaic Species Selection

The results of this research establish a trait-based framework for predicting species performance under temporally structured shade regimes. For grasses, stomatal anatomy (guard cell length, adaxial stomatal density), leaf construction (leaf mass per area), and hydraulics (leaf hydraulic conductance) predict dynamic performance through structure-kinetics relationships that explain 25–30% of variance in opening time (Table 5). Species with smaller guard cells, higher adaxial stomatal density, lower leaf mass per area, and higher leaf hydraulic conductance tend toward faster stomatal kinetics and thus lower amounts of forgone carbon assimilation during induction. These structural traits can serve as screening criteria for species selection or breeding targets for kinetic improvement within grass germplasm.

Among the grasses, species with higher LMA required longer to achieve full photosynthetic capacity following a light increase (ρ = 0.49; Table 5). established that high LMA reflects a

conservative, slow-return strategy within the leaf economics spectrum. The correlation with slower biochemical induction and greater LMA observed here suggests this slow signature may extend to dynamic performance. Because LMA can be measured rapidly and non-destructively, it may offer potential as a screening tool for identifying species with lower LMA (or high SLA) as fast responding genotypes for agrivoltaic environments. However, the moderate effect size and restriction to grasses limit its predictive reliability, and the mechanistic basis remains unclear. Poorter et al. (2016) reported that lab-grown plants have, on average, a 60% higher specific leaf area than field-grown plants. LMA measurements should therefore be standardised to field conditions for maximum predictive validity. Future work should test LMA screening across broader species ranges, including additional dicots, to determine whether the grass-specific relationship observed here extends to other functional groups or whether distinct screening criteria are needed for each.

Yiotis et al. (2021) found approximately 7-fold intraspecific variation in aboveground biomass productivity among 40 ryegrass genotypes, with tiller count being the strongest predictor of dry weight. Future work should examine whether kinetic traits show similar phenotypic correlations and genotypic variation within species. Poorter et al. (2019) reported that tillering showed the highest plasticity index (5.0) among allocation traits, suggesting this whole-plant response may be more important than leaf-level kinetics for field outcomes. Pang et al. (2017) documented that grasses maintained relative feed value better under shade (relative distance plasticity index = 0.035–0.039) while legumes were more resilient in crude protein content, adding a nutritional quality dimension to species selection considerations. These forage quality responses may interact with kinetic performance to determine the overall suitability of species for agrivoltaic systems.

Laub et al. (2022) classified forages as shade-tolerant based on constant shade (103% yield at 20% light reduction). However, Clover's failure to benefit from shade treatments despite meeting these criteria demonstrates that steady-state shade tolerance does not predict performance when

light fluctuates; kinetic constraints become limiting under dynamic conditions. For agrivoltaic system design, this distinction matters: fixed arrays produce temporal light patterns regardless of average shade intensity, meaning that species selection based on shade tolerance alone will miss kinetic limitations that determine performance. Sturchio and Knapp (2023) proposed an ecovoltaics framework that co-prioritises ecosystem services and energy production, noting that panel design determines microclimate patterns and species suitability, a design principle directly supported by the kinetics-dependent responses observed here.

Weselek et al. (2021) documented that Clover proportion increased relative to grasses under agrivoltaic shade, a shift conventionally interpreted as Clover's superior shade tolerance. Results here suggest an alternative interpretation: Clover may persist under shade not because it performs well but because grasses decline more when light is reduced uniformly. Under temporally structured shade where light concentrates during windows that favour fast kinetics, this competitive balance could reverse. Timothy's 69% biomass gain under afternoon shade suggests that array configurations shifting the diurnal pattern of light availability could shift grass-Clover balance in favour of fast-kinetic grasses, potentially improving forage quality (higher grass:legume ratio) and reducing nitrogen leaching risk associated with legume decomposition Pang et al. (2017).

8.7 Limitations and Future Directions

Inclusion of only one dicot species (Clover) in this study prevented assessment of whether structure-kinetics relationships masked by Clover reflect legume-specific, dicot-general, or species-specific patterns. Resolving this uncertainty requires testing additional dicot species across multiple families.

Leaf nitrogen content was not measured, preventing direct assessment of allocation patterns underlying kinetic differences. The leaf mass per area–biochemical induction relationship observed

among grasses (Table 5) may reflect nitrogen allocation to Rubisco and Rubisco activase (Wright et al., 2004; Yamori et al., 2011), but this remains untested.

Mesophyll conductance (g_m) was not separated from the biochemical limitation component. The differential method employed (Deans et al., 2019b) partitions limitations into stomatal and non-stomatal components, but the latter encompasses both true biochemical constraints and g_m limitations. Given that g_m varies among functional groups and responds dynamically to environmental conditions (Flexas et al., 2008), biochemical limitation values reported here likely include a mesophyll conductance component. However, this does not affect primary conclusions regarding stomatal kinetics, which were directly measured through conductance dynamics.

The field experiment used pot-grown plants rather than ground-planted swards, which may have limited the expression of species-specific responses. Root restriction in containers limits soil volume exploration and can modify biomass allocation patterns (Poorter et al., 2016). Additionally, Sperry (2000) demonstrated that the soil-to-root pathway represents a major component of whole-plant hydraulic conductance, and that this component declines substantially as soil dries; a dynamic that may differ between pot and field trials. Poorter et al. (2016) found that phenotypic correlations between controlled and field environments are often modest, advising that pot-based trials may not fully predict responses of established swards. Furthermore, the single-site, single-season experiment limits confidence in the treatment effects generally; multi-year replication would strengthen predictions across environmental variation. Finally, step-change light transitions differ from natural sunfleck dynamics (Pearcy, 1990), and induction kinetics were not directly measured in the field.

McAusland et al. (2016) noted that the rapidity of stomatal conductance in dumbbell-shaped guard cells could be attributed to size, whilst in elliptical-shaped guard cells features other than anatomy were more important for kinetics. The present study provides additional support for this pattern: among grasses with dumbbell-shaped guard cells, stomatal size (GCL) and density predicted

kinetic performance (Table 5), whereas Clover, with kidney-shaped guard cells, showed no such structure-function relationships, despite exhibiting the slowest kinetics of all species tested. Guard cell architecture may therefore be the primary screening criterion when comparing across functional groups, with anatomical predictors valid within grasses but not transferable to dicots. Testing this prediction across additional dicot species, genotypes, and environments represents a clear direction for future research. The practical implication for agrivoltaic system design is that forage species selection should be informed by panel orientation and tracking systems that determine the temporal pattern of shading, not merely by expectations of overall shade tolerance. Where morning light is preserved and afternoon light reduced, fast-inducing species like Timothy may substantially outperform conventionally shade-tolerant alternatives.

8.8 Conclusions

This study establishes stomatal kinetics as a critical determinant of species performance under temporally structured light environments characteristic of agrivoltaic systems. The 8-fold variation in stomatal opening time across temperate forage species (5–40 min; Figure 4A) translated to approximately a 2-fold variation in carbon costs during induction (Figure 8A), with forgone assimilation strongly predicted by opening speed (Figure 8B). Field experiments confirmed these kinetic differences determine biomass outcomes: Timothy's 5-min opening time enabled +69% biomass gain under afternoon shade by exploiting concentrated morning light, while Clover's 40-min opening time prevented biomass response despite high structural plasticity. However, kinetic speed alone was not deterministic: Perennial ryegrass's fast opening (6.3 min) yielded no biomass gain, likely because its water-spending hydraulic strategy imposes costs under shade, whereas Italian ryegrass achieved +24% gain despite intermediate kinetics (11.5 min), suggesting that the coordination of stomatal kinetics with hydraulic regulation determines outcomes.

Structure-kinetics relationships operated within, but not across, functional groups within this study. Among grasses, stomatal anatomy, leaf construction, and hydraulic conductance predict kinetic performance (Table 5), enabling trait-based screening for dynamic performance. These relationships are obscured when Clover is included, likely reflecting fundamental differences between graminoid and dicot leaves. Whether dicots exhibit their own structure-kinetics relationships, or whether Clover's position reflects legume-specific or species-specific outlier behaviour, requires further study.

For agrivoltaic system design, these results indicate that species selection should consider kinetic traits alongside traditional shade tolerance criteria. Array configurations that concentrate light temporally, whether through tracking systems or fixed north-south orientations that create diurnal shade patterns, create conditions favouring fast-kinetic species capable of exploiting concentrated light windows. Leaf mass per area emerges as a potential screening tool: among grasses, lower leaf mass per area predicts faster biochemical induction (Table 5), offering a rapid, non-destructive proxy for dynamic performance that should be tested across broader species ranges including additional dicots. Ultimately, the study demonstrates that understanding plant performance under novel light environments such as presented by photovoltaic arrays requires moving beyond steady-state measurements to characterise the kinetics of response, a shift with implications extending beyond agrivoltaics to any agricultural context where light varies on timescales comparable to stomatal response times.

9 References

A&D Company Ltd (2024) *WinCT (RsKey) Software User Manual.* Tokyo, Japan: A&D Company.

Acevedo-Siaca, L. G., Coe, R., Wang, Y., Kromdijk, J., Quick, W. P. & Long, S. P. (2020) Variation in photosynthetic induction between rice accessions and its potential for improving productivity. *New Phytologist,* 227(4)**,** 1097-1108. 10.1111/nph.16454.

Adams, M. A., Turnbull, T. L., Sprent, J. I. & Buchmann, N. (2016) Legumes are different: Leaf nitrogen, photosynthesis, and water use efficiency. *Proceedings of the National Academy of Sciences,* 113(15)**,** 4098-103. 10.1073/pnas.1523936113.

Akaike, H. (1974) A new look at the statistical model identification. *IEEE Transactions on Automatic Control,* 19**,** 716-723.

Akbar, A., Mahmood, F. I., Alam, H., Aziz, F., Bashir, K. & Zafar Butt, N. (2024) Field Assessment of Vertical Bifacial Agrivoltaics with Vegetable Production: A Case Study in Lahore, Pakistan. *Renewable Energy,* 227. 10.1016/j.renene.2024.120513.

Allen, R., Pereira, L., Raes, D. & Smith, M. (1998) Crop evapotranspiration - Guidelines for computing crop water requirements. *FAO Irrigation and drainage paper 56.* Available at: https://www.researchgate.net/publication/235704197_Crop_evapotranspiration-Guidelines_for_computing_crop_water_requirements-FAO_Irrigation_and_drainage_paper_56 [Accessed 08th October 2025].

Anderson, M. J. (2001) A new method for non-parametric multivariate analysis of variance. *Austral Ecology,* 26(1)**,** 32-46.

Anderson, M. J. (2006) Distance-based tests for homogeneity of multivariate dispersions. *Biometrics,* 62**,** 245-253.

Andrew, A. C., Higgins, C. W., Smallman, M. A., Graham, M. & Ates, S. (2021) Herbage Yield, Lamb Growth and Foraging Behavior in Agrivoltaic Production System. *Frontiers in Sustainable Food Systems,* 5. 10.3389/fsufs.2021.659175.

Armstrong, A., Ostle, N. J. & Whitaker, J. (2016) Solar park microclimate and vegetation management effects on grassland carbon cycling. *Environmental Research Letters,* 11(7). 10.1088/1748-9326/11/7/074016.

Barron-Gafford, G. A., Pavao-Zuckerman, M. A., Minor, R. L., Sutter, L. F., Barnett-Moreno, I., Blackett, D. T., Thompson, M., Dimond, K., Gerlak, A. K., Nabhan, G. P. & Macknick, J. E. (2019) Agrivoltaics provide mutual benefits across the food–energy–water nexus in drylands. *Nature Sustainability,* 2(9)**,** 848-855. 10.1038/s41893-019-0364-5.

Bartlett, M. S. (1954) A note on the multiplying factors for various χ^2 approximations. *Journal of the Royal Statistical Society Series B,* 16**,** 296-298.

Bengtsson, J., Bullock, J. M., Egoh, B., Everson, C., Everson, T., O'connor, T., O'farrell, P. J., Smith, H. G. & Lindborg, R. (2019) Grasslands—more important for ecosystem services than you might think. *Ecosphere,* 10(2). 10.1002/ecs2.2582.

Benjamini, Y. & Hochberg, Y. (1995) Controlling the false discovery rate: a practical and powerful approach to multiple testing. *Journal of the Royal Statistical Society: Series B (Methodological),* 57(1)**,** 289-300.

Bertolino, L. T., Caine, R. S. & Gray, J. E. (2019) Impact of Stomatal Density and Morphology on Water-Use Efficiency in a Changing World. *Frontiers in Plant Science,* 10**,** 225. 10.3389/fpls.2019.00225.

Bradshaw, A. D. (1965) Evolutionary Significance of Phenotypic Plasticity in Plants. In: Caspari, E. W. & Thoday, J. M. (eds.) *Advances in Genetics.* Academic Press.

Brien, C. J., Berger, B., Rabie, H. & Tester, M. (2013) Accounting for variation in designing greenhouse experiments with special reference to greenhouses containing plants on conveyor systems. *Plant Methods,* 9(5)**,** 1-21.

Brodribb, T. J., Feild, T. S. & Jordan, G. J. (2007) Leaf maximum photosynthetic rate and venation are linked by hydraulics. *Plant Physiology,* 144(4)**,** 1890-8. 10.1104/pp.107.101352.

Brodribb, T. J., Holbrook, N. M., Zwieniecki, M. A. & Palma, B. (2005) Leaf hydraulic capacity in ferns, conifers and angiosperms: impacts on photosynthetic maxima. *New Phytologist,* 165(3)**,** 839-46. 10.1111/j.1469-8137.2004.01259.x.

Brodribb, T. J. & Jordan, G. J. (2008) Internal coordination between hydraulics and stomatal control in leaves. *Plant Cell & Environment,* 31(11)**,** 1557-64. 10.1111/j.1365-3040.2008.01865.x.

Brodribb, T. J., Jordan, G. J. & Carpenter, R. J. (2013) Unified changes in cell size permit coordinated leaf evolution. *New Phytologist,* 199(2)**,** 559-570. 10.1111/nph.12300.

Brodribb, T. J., Mcadam, S. A. & Carins Murphy, M. R. (2017) Xylem and stomata, coordinated through time and space. *Plant Cell & Environment,* 40(6)**,** 872-880. 10.1111/pce.12817.

Buckley, T. N. (2005) The control of stomata by water balance. *New Phytologist,* 168(2)**,** 275-92. 10.1111/j.1469-8137.2005.01543.x.

Burnham, K. P. & Anderson, D. R. (2002) *Model Selection and Multimodel Inference: A Practical Information-Theoretic Approach.* New York: Springer.

Busch, F. A. (2018) Photosynthetic Gas Exchange in Land Plants at the Leaf Level. In: Covshoff, S. (ed.) *Photoynthesis Methods and Protocols.* New York: Humana Press.

Carins Murphy, M. R., Jordan, G. J. & Brodribb, T. J. (2014) Acclimation to humidity modifies the link between leaf size and the density of veins and stomata. *Plant Cell & Environment,* 37(1)**,** 124-31. 10.1111/pce.12136.

Carmo-Silva, A. E. & Salvucci, M. E. (2013) The regulatory properties of Rubisco activase differ among species and affect photosynthetic induction during light transitions. *Plant Physiology,* 161(4)**,** 1645-55. 10.1104/pp.112.213348.

Casson, S. & Gray, J. E. (2008) Influence of environmental factors on stomatal development. *New Phytologist,* 178(1)**,** 9-23. 10.1111/j.1469-8137.2007.02351.x.

Chai, T. & Draxler, R. R. (2014) Root mean square error (RMSE) or mean absolute error (MAE)? – Arguments against avoiding RMSE in the literature. *Geoscientific Model Development,* 7**,** 1247-1250.

Chazdon, R. L. & Pearcy, R. W. (1986) Photosynthetic responses to light variation in rainforest species II. Carbon gain and photosynthetic efficiency during lightflecks. *Oecologia,* 69(4)**,** 524-531.

Climate-Data.Org (2025) *Climate: Lancaster.* Available at: https://en.climate-data.org/europe/united-kingdom/england/lancaster-367/ [Accessed 02nd October 2025].

Conant, R. T., Paustian, K. & Elliott, E. T. (2001) Grassland management and conversion into grassland: effects on soil carbon. *Ecological Applications,* 11(2)**,** 343-355. 10.1890/1051-0761(2001)011[0343:GMACIG]2.0.CO;2.

Conover, W. J. & Iman, R. L. (1979) On multiple-comparisons procedures Technical Report LA-7677-MS. Los Alamos, NM: Los Alamos Scientific Laboratory.

Cotswold Grass Seeds (2025a) *Grass straights*. Moreton-in-Marsh, UK: Cotswold Grass Seeds Ltd. Available at: https://www.cotswoldseeds.com/seeds/20/grass [Accessed 08th October 2024].

Cotswold Grass Seeds (2025b) *Solarpark seed mixtures*. Available at: https://www.cotswoldseeds.com/seeds/18/solar-park [Accessed 13th November 2025].

De Bello, F., Thuiller, W., Lepš, J., Choler, P., Clément, J. C., Macek, P., Sebastià, M. T. & Lavorel, S. (2009) Partitioning of functional diversity reveals the scale and extent of trait convergence and divergence. *Journal of Vegetation Science,* 20(3)**,** 475-486. 10.1111/j.1654-1103.2009.01042.x.

Deans, R. M., Brodribb, T. J., Busch, F. A. & Farquhar, G. D. (2019a) Plant water-use strategy mediates stomatal effects on the light induction of photosynthesis. *New Phytologist,* 222(1)**,** 382-395. 10.1111/nph.15572.

Deans, R. M., Farquhar, G. D. & Busch, F. A. (2019b) Estimating stomatal and biochemical limitations during photosynthetic induction. *Plant Cell & Environment,* 42(12)**,** 3227-3240. 10.1111/pce.13622.

Dennis, W. D. & Woledge, J. (1982) Photosynthesis by White Clover leaves in mixed Clover/ryegrass swards. *Annals of Botany,* 49(5)**,** 627-635.

Dewitt, T. J., Sih, A. & Wilson, D. S. (1998) Costs and limits of phenotypic plasticity. *Trends in Ecology & Evolution,* 13(2)**,** 77-81.

Dhlamini, M. S. & Brent, A. C. (2025) Assessing the impact of solar PV on vegetation growth through ground sunlight distribution at a solar farm in Aotearoa New Zealand. *Aotearoa Solar Energy Society Journal,* 1. 10.26686/ases.v1.9912.

Diaz, S., Kattge, J., Cornelissen, J. H., Wright, I. J., Lavorel, S., Dray, S., Reu, B., Kleyer, M., Wirth, C., Prentice, I. C., Garnier, E., Bonisch, G., Westoby, M., Poorter, H., Reich, P. B., Moles, A. T., Dickie, J., Gillison, A. N., Zanne, A. E., Chave, J., Wright, S. J., Sheremet'ev, S. N., Jactel, H., Baraloto, C., Cerabolini, B., Pierce, S., Shipley, B., Kirkup, D., Casanoves, F., Joswig, J. S., Gunther, A., Falczuk, V., Ruger, N., Mahecha, M. D. & Gorne, L. D. (2016) The global spectrum of plant form and function. *Nature,* 529(7585)**,** 167-71. 10.1038/nature16489.

Dodd, A. N., Salathia, N., Hall, A., Kevei, E., Tóth, R., Nagy, F., Hibberd, J. M., Millar, A. J. & Webb, A. a. R. (2005) Plant circadian clocks increase photosynthesis, growth, survival, and competitive advantage. *Science,* 309**,** 630–633. 10.1126/science.1115581.

Dow, G. J., Berry, J. A. & Bergmann, D. C. (2014) The physiological importance of developmental mechanisms that enforce proper stomatal spacing in Arabidopsis thaliana. *New Phytologist,* 201(4)**,** 1205-1217. 10.1111/nph.12586.

Drake, P. L., De Boer, H. J., Schymanski, S. J. & Veneklaas, E. J. (2019) Two sides to every leaf: water and CO_2 transport in hypostomatous and amphistomatous leaves. *New Phytologist,* 222(3)**,** 1179-1187.

Dupraz, C., Marrou, H., Talbot, G., Dufour, L., Nogier, A. & Ferard, Y. (2011) Combining solar photovoltaic panels and food crops for optimising land use: Towards new agrivoltaic schemes. *Renewable Energy,* 36(10)**,** 2725-2732. 10.1016/j.renene.2011.03.005.

Ehret, M., Graß, R. & Wachendorf, M. (2015) The effect of shade and shade material on White Clover/perennial ryegrass mixtures for temperate agroforestry systems. *Agroforestry Systems,* 89(3)**,** 557-570. 10.1007/s10457-015-9791-0.

Elliott-Kingston, C., Haworth, M., Yearsley, J. M., Batke, S. P., Lawson, T. & Mcelwain, J. C. (2016) Does Size Matter? Atmospheric CO2 May Be a Stronger Driver of Stomatal Closing Rate Than Stomatal Size in Taxa That Diversified under Low CO2. *Front Plant Science,* 7**,** 1253. 10.3389/fpls.2016.01253.

Evans, J. R. (1989) Photosynthesis and nitrogen relationships in leaves of C_3 plants. *Oecologia,* 78(1)**,** 9-19.

Faust, J. E., Holcombe, V., Rajapakse, N. C. & Layne, D. R. (2005) The effect of daily light integral on bedding plant growth and flowering. *Horticultural Science,* 40(3)**,** 645-649.

Fox, J. & Weisberg, S. (2019) *An R Companion to Applied Regression.* 3rd ed. Thousand Oaks, CA: Sage.

Franks, P. J. & Beerling, D. J. (2009) Maximum leaf conductance driven by CO_2 effects on stomatal size and density over geologic time. *Proceedings of the National Academy of Sciences USA,* 106(25)**,** 10343–10347.

Franks, P. J. & Farquhar, G. D. (2007) The mechanical diversity of stomata and its significance in gas-exchange control. *Plant Physiology,* 143(1)**,** 78-87. 10.1104/pp.106.089367.

Fritz, C. O., Morris, P. E. & Richler, J. J. (2012) Effect size estimates: Current use, calculations, and interpretation. *Journal of Experimental Psychology: General,* 141(1)**,** 2-18.

Funk, J. L., Larson, J. E., Ames, G. M., Butterfield, B. J., Cavender-Bares, J., Firn, J., Laughlin, D. C., Sutton-Grier, A. E., Williams, L. & Wright, J. (2017) Revisiting the Holy Grail: using plant functional traits to understand ecological processes. *Biological Reviews Cambridge Philosophical Society,* 92(2)**,** 1156-1173. 10.1111/brv.12275.

Gelman, A. & Hill, J. (2006) Multilevel linear models: the basics. In: *Data Analysis Using Regression and Multilevel/Hierarchical Models.* Cambridge: Cambridge University Press.

Ghalambor, C. K., Mckay, J. K., Carroll, S. P. & Reznick, D. N. (2007) Adaptive versus non‐adaptive phenotypic plasticity and the potential for contemporary adaptation in new environments. *Functional Ecology,* 21(3)**,** 394-407. 10.1111/j.1365-2435.2007.01283.x.

Goetzberger, A. & Zastrow, A. (1982) On the Coexistence of Solar-Energy Conversion and Plant Cultivation. *International Journal of Solar Energy,* 1(1)**,** 55-69. 10.1080/01425918208909875.

Grossiord, C., Buckley, T. N., Cernusak, L. A., Novick, K. A., Poulter, B., Siegwolf, R. T. W., Sperry, J. S. & Mcdowell, N. G. (2020) Plant responses to rising vapor pressure deficit. *New Phytologist,* 226(6)**,** 1550-1566. 10.1111/nph.16485.

Grunwald, Y., Yaaran, A. & Moshelion, M. (2024) Illuminating plant water dynamics: the role of light in leaf hydraulic regulation. *New Phytologist,* 241(4)**,** 1404-1414. 10.1111/nph.19497.

Hartung, J., Wagener, J., Ruser, R. & Piepho, H. P. (2019) Blocking and re-arrangement of pots in greenhouse experiments: which approach is more effective? *Plant Methods,* 15**,** 143. 10.1186/s13007-019-0527-4.

Haworth, M., Marino, G., Loreto, F. & Centritto, M. (2021) Integrating stomatal physiology and morphology: evolution of stomatal control and development of future crops. *Oecologia*(4)**,** 867-883. 10.1007/s00442-021-04857-3.

Holloway-Phillips, M. M. & Brodribb, T. J. (2011a) Contrasting hydraulic regulation in closely related forage grasses: implications for plant water use. *Functional Plant Biology,* 38(7)**,** 594-605. 10.1071/FP11029.

Holloway-Phillips, M. M. & Brodribb, T. J. (2011b) Minimum hydraulic safety leads to maximum water-use efficiency in a forage grass. *Plant, Cell & Environment,* 34(2)**,** 302-13. 10.1111/j.1365-3040.2010.02244.x.

Hopkins, A. & Wilkins, R. J. (2006) Temperate grassland: key developments in the last century and future perspectives. *The Journal of Agricultural Science,* 144(6)**,** 503-523. 10.1017/S0021859606006496.

Hõrak, H. (2025) Functional and developmental differences between adaxial and abaxial stomata in amphistomatous leaves. *New Phytologist*. 10.1111/nph.70762.

Hurvich, C. M. & Tsai, C. L. (1989) Regression and time series model selection in small samples. *Biometrika,* 76**,** 297-307.

Irving, L. (2015) Carbon Assimilation, Biomass Partitioning and Productivity in Grasses. *Agriculture,* 5(4)**,** 1116-1134. 10.3390/agriculture5041116.

Jaikumar, N. S., Stutz, S. S., Fernandes, S. B., Leakey, A. D. B., Bernacchi, C. J., Brown, P. J. & Long, S. P. (2021) Can improved canopy light transmission ameliorate loss of photosynthetic efficiency in the shade? An investigation of natural variation in Sorghum bicolor. *Journal of Experimental Botany,* 72(13)**,** 4965-4980. 10.1093/jxb/erab176.

Jolliffe, I. T. (2002) *Principal Component Analysis.* New York: Springer.

Kaiser, E., Kromdijk, J., Harbinson, J., Heuvelink, E. & Marcelis, L. F. (2017) Photosynthetic induction and its diffusional, carboxylation and electron transport processes as affected by CO2 partial pressure, temperature, air humidity and blue irradiance. *Ann Bot,* 119(1)**,** 191-205. 10.1093/aob/mcw226.

Kaiser, E., Morales, A. & Harbinson, J. (2018) Fluctuating light takes crop photosynthesis on a rollercoaster. *Plant Physiology,* 176(2)**,** 977-989. 10.1104/pp.17.01250.

Kaiser, E., Morales, A., Harbinson, J., Heuvelink, E., Prinzenberg, A. E. & Marcelis, L. F. (2016) Metabolic and diffusional limitations of photosynthesis in fluctuating irradiance in Arabidopsis thaliana. *Scientific Reports,* 6**,** 31252. 10.1038/srep31252.

Kaiser, E., Morales, A., Harbinson, J., Kromdijk, J., Heuvelink, E. & Marcelis, L. F. (2015) Dynamic photosynthesis in different environmental conditions. *Journal of Experimental Botany,* 66(9)**,** 2415-26. 10.1093/jxb/eru406.

Kaiser, H. F. (1974) An index of factorial simplicity. *Psychometrika,* 39**,** 31-36.

Kardiman, R. & Ræbild, A. (2018) Relationship between stomatal density, size and speed of opening in Sumatran rainforest species. *Tree Physiology,* 38(5)**,** 696-705. 10.1093/treephys/tpx149.

Kromdijk, J., Głowacka, K., Leonelli, L., Gabilly, S. T., Iwai, M., Niyogi, K. K. & Long, S. P. (2016) Improving photosynthesis and crop productivity by accelerating recovery from photoprotection. *Science,* 18(354(6314))**,** 857-861. 10.1126/science.aai8878.

Kruitwagen, L., Story, K. T., Friedrich, J., Byers, L., Skillman, S. & Hepburn, C. (2021) A global inventory of photovoltaic solar energy generating units. *Nature,* 598(7882)**,** 604-610. 10.1038/s41586-021-03957-7.

Kruskal, W. H. & Wallis, W. A. (1952) Use of ranks in one-criterion variance analysis. *Journal of the American Statistical Association,* 47**,** 583-621.

Kumpanalaisatit, M., Setthapun, W., Sintuya, H., Pattiya, A. & Jansri, S. N. (2022) Current status of agrivoltaic systems and their benefits to energy, food, environment, economy, and society. *Sustainable Production and Consumption,* 33**,** 952-963. 10.1016/j.spc.2022.08.013.

Laub, M., Pataczek, L., Feuerbacher, A., Zikeli, S. & Högy, P. (2022) Contrasting yield responses at varying levels of shade suggest different suitability of crops for dual land-use systems: a meta-analysis. *Agronomy for Sustainable Development,* 42(51). 10.1007/s13593-022-00783-7.

Lawson, T. & Blatt, M. R. (2014) Stomatal size, speed, and responsiveness impact on photosynthesis and water use efficiency. *Plant Physiology,* 164(4)**,** 1556-70. 10.1104/pp.114.237107.

Lawson, T. & Vialet-Chabrand, S. (2019) Speedy stomata, photosynthesis and plant water use efficiency. *New Phytologist,* 221(1)**,** 93-98. 10.1111/nph.15330.

Lê, S., Josse, J. & Husson, F. (2008) FactoMineR: an R package for multivariate analysis. *Journal of Statistical Software,* 25**,** 1-18.

Lenth, R. V. (2025) emmeans: Estimated Marginal Means, aka Least-Squares Means. R package version 1.11.1. Available at: https://CRAN.R-project.org/package=emmeans. [Accessed 01st October 2025].

Levene, H. (1960) Robust Tests for Equality of Variances. In: *Contributions to Probability and Statistics: Essays in Honor of Harold Hotelling.* Stanford, CA: Stanford University Press.

Li-Cor Biosciences (1998) *LI-6400XT Portable Photosynthesis System Instruction Manual.* Lincoln, NE, USA: LI-COR Inc.

Li-Cor Biosciences (2021) *LI-3100C Area Meter Instruction Manual.* Lincoln, NE, USA: LI-COR Inc.

Lin, C. H., Mcgraw, R. L., George, M. F. & Garrett, H. E. (1999) Shade effects on forage crops with potential in temperate agroforestry practices. *Agroforestry Systems,* 44**,** 109–119. 10.1023/A:1006205116354.

Liu, K., Wang, Y., Magney, T. S. & Frankenberg, C. (2024) Non-steady-state stomatal conductance modeling and its implications: from leaf to ecosystem. *Biogeosciences,* 21(6)**,** 1501-1516. 10.5194/bg-21-1501-2024.

Liu, L., Sayer, E. J., Deng, M., Li, P., Liu, W., Wang, X., Yang, S., Huang, J., Luo, J., Su, Y., Grunzweig, J. M., Jiang, L., Hu, S. & Piao, S. (2023) The grassland carbon cycle: Mechanisms, responses to global changes, and potential contribution to carbon neutrality. *Fundamental Research,* 3(2)**,** 209-218. 10.1016/j.fmre.2022.09.028.

Liu, Y., Dawson, W., Prati, D., Haeuser, E., Feng, Y. & Van Kleunen, M. (2016) Does greater specific leaf area plasticity help plants to maintain a high performance when shaded? *Annals of Botany,* 118(7)**,** 1329-1336. 10.1093/aob/mcw180.

Long, S. P. & Bernacchi, C. J. (2003) Gas exchange measurements, what can they tell us about the underlying limitations to photosynthesis? Procedures and sources of error. *Journal of Experimental Botany,* 54**,** 2393–2401. 10.1093/jxb/erg262.

Long, S. P., Taylor, S. H., Burgess, S. J., Carmo-Silva, E., Lawson, T., De Souza, A. P., Leonelli, L. & Wang, Y. (2022) Into the Shadows and Back into Sunlight: Photosynthesis in Fluctuating Light. *Annual Review Plant Biology,* 73**,** 617-648. 10.1146/annurev-arplant-070221-024745.

Mardia, K. V. (1970) Measures of multivariate skewness and kurtosis with applications. *Biometrika,* 57(3)**,** 519-530.

Marrou, H., Dufour, L. & Wery, J. (2013a) How does a shelter of solar panels influence water flows in a soil–crop system? *European Journal of Agronomy,* 50**,** 38-51. 10.1016/j.eja.2013.05.004.

Marrou, H., Guilioni, L., Dufour, L., Dupraz, C. & Wery, J. (2013b) Microclimate under agrivoltaic systems: Is crop growth rate affected in the partial shade of solar panels? *Agricultural and Forest Meteorology,* 177**,** 117-132. 10.1016/j.agrformet.2013.04.012.

Marrou, H., Wery, J., Dufour, L. & Dupraz, C. (2013c) Productivity and radiation use efficiency of lettuces grown in the partial shade of photovoltaic panels. *European Journal of Agronomy,* 44**,** 54-66. 10.1016/j.eja.2012.08.003.

Mason, N. W., Orwin, K., Lambie, S., Woodward, S. L., Mccready, T. & Mudge, P. (2016) Leaf economics spectrum-productivity relationships in intensively grazed pastures depend on dominant species identity. *Ecol Evol,* 6(10)**,** 3079-91. 10.1002/ece3.1964.

Matthews, J. S. A., Vialet-Chabrand, S. R. M. & Lawson, T. (2017) Diurnal Variation in Gas Exchange: The Balance between Carbon Fixation and Water Loss. *Plant Physiol,* 174(2)**,** 614-623. 10.1104/pp.17.00152.

Mcausland, L., Vialet-Chabrand, S., Davey, P., Baker, N. R., Brendel, O. & Lawson, T. (2016) Effects of kinetics of light-induced stomatal responses on photosynthesis and water-use efficiency. *New Phytologist,* 211(4)**,** 1209-20. 10.1111/nph.14000.

Mead, R., Curnow, R. N. & Hasted, A. M. (2017) *Statistical Methods in Agriculture and Experimental Biology*. [New York: Chapman and Hall/CRC. Available at: https://doi.org/10.1201/9780203738559.

Meinzer, F. C., Smith, D. D., Woodruff, D. R., Marias, D. E., Mcculloh, K. A., Howard, A. R. & Magedman, A. L. (2017) Stomatal kinetics and photosynthetic gas exchange along a continuum of isohydric to anisohydric regulation of plant water status. *Plant Cell Environ,* 40(8)**,** 1618-1628. 10.1111/pce.12970.

Morales, A. & Kaiser, E. (2020) Photosynthetic Acclimation to Fluctuating Irradiance in Plants. *Front Plant Sci,* 11**,** 268. 10.3389/fpls.2020.00268.

Moré, J. J. The Levenberg-Marquardt algorithm: Implementation and theory. Berlin, Heidelberg. Springer Berlin Heidelberg, 105-116.

Mott, K. A. & Woodrow, I. E. (2000) Modelling the role of Rubisco activase in limiting non-steady-state photosynthesis. *Journal of Experimental Botany,* 51(suppl_1)**,** 399-406. 10.1093/jexbot/51.suppl_1.399.

Muir, C. D. (2015) Making pore choices: repeated regime shifts in stomatal ratio. *Proc Biol Sci,* 282(1813)**,** 20151498. 10.1098/rspb.2015.1498.

Muir, C. D. (2018) Light and growth form interact to shape stomatal ratio among British angiosperms. *New Phytologist,* 218(1)**,** 242-252. 10.1111/nph.14956.

Muir, C. D., Hangarter, R. P., Moyle, L. C. & Davis, P. A. (2014) Morphological and anatomical determinants of mesophyll conductance in wild relatives of tomato (Solanum sect. Lycopersicon, sect. Lycopersicoides; Solanaceae). *Plant Cell Environ,* 37(6)**,** 1415-26. 10.1111/pce.12245.

Neesham-Mctiernan, T. H., Randle-Boggis, R. J., Buckley, A. R. & Hartley, S. E. (2025) The spatial potential for agrivoltaics to address energy-agriculture land use conflicts in Great Britain. *Applied Energy,* 385. 10.1016/j.apenergy.2025.125527.

Nicotra, A. B., Atkin, O. K., Bonser, S. P., Davidson, A. M., Finnegan, E. J., Mathesius, U., Poot, P., Purugganan, M. D., Richards, C. L., Valladares, F. & Van Kleunen, M. (2010) Plant phenotypic plasticity in a changing climate. *Trends in Plant Science,* 15(12)**,** 684-92. 10.1016/j.tplants.2010.09.008.

Niinemets, Ü. (2001) Global-Scale Climatic Controls of Leaf Dry Mass Per Area, Density, and Thickness in Trees and Shrubs. *Ecology,* 82(2)**,** 453-469. 10.1890/0012-9658(2001)082[0453:Gsccol]2.0.Co;2.

Niinemets, Ü. (2002) Stomatal conductance alone does not explain the decline in foliar photosynthetic rates with increasing tree age and size in Picea abies and Pinus sylvestris. *Tree Physiology,* 22(8)**,** 515-535.

Oksanen, J., Simpson, G., Blanchet, F., Kindt, R., Legendre, P., Minchin, P., O'hara, R., Solymos, P., Stevens, M., Szoecs, E., Wagner, H., Barbour, M., Bedward, M., Bolker, B., Borcard, D., Carvalho, G., Chirico, M., De Caceres, M., Durand, S., Evangelista, H., Fitzjohn, R., Friendly, M., Furneaux, B., Hannigan, G., Hill, M., Lahti, L., Mcglinn, D., Ouellette, M., Ribeiro Cunha, E., Smith, T., Stier, A., Ter Braak, C., Weedon, J. & Borman, T. (2025) *vegan: Community Ecology Package. R package version 2.6-10.* Available at: https://CRAN.R-project.org/package=vegan. [Accessed 25th June 2025].

Onset Computer Corporation (2024) *HOBOware Pro Software*. Available at: https://www.onsetcomp.com/products/software/hoboware [Accessed 15th August 2025].

Pang, K., Van Sambeek, J. W., Navarrete-Tindall, N. E., Lin, C.-H., Jose, S. & Garrett, H. E. (2017) Responses of legumes and grasses to non-, moderate, and dense shade in Missouri, USA. II. Forage quality and its species-level plasticity. *Agroforestry Systems,* 93(1)**,** 25-38. 10.1007/s10457-017-0068-7.

Pantin, F., Simonneau, T., Rolland, G., Dauzat, M. & Muller, B. (2011) Control of leaf expansion: a developmental switch from metabolics to hydraulics. *Plant Physiology,* 156(2)**,** 803-15. 10.1104/pp.111.176289.

Pearcy, R. W. (1990) Sunflecks and photosynthesis in plant canopies. *Annual Review of Plant Physiology and Plant Molecular Biology,* 41(1)**,** 421-453.

Peri, P. L., Mcneil, D. L., Moot, D. J., Varella, A. C. & Lucas, R. J. (2002a) Net photosynthetic rate of cocksfoot leaves under continuous and fluctuating shade conditions in the field. *Grass and Forage Science,* 57(2)**,** 157-170. 10.1046/j.1365-2494.2002.00312.x.

Peri, P. L., Moot, D. J., Mcneil, D. L., Varella, A. C. & Lucas, R. J. (2002b) Modelling net photosynthetic rate of field‐grown cocksfoot leaves under different nitrogen, water and temperature regimes. *Grass and Forage Science,* 57(1)**,** 61-71. 10.1046/j.1365-2494.2002.00302.x.

Piepho, H. P. (2004) An algorithm for a letter-based representation of all-pairwise comparisons. *Journal of Computational and Graphical Statistics,* 13**,** 456-466.

Pinheiro, J., Bates, D., Debroy, S., Sarkar, D. & R Core Team (2024) nlme: Linear and Nonlinear Mixed Effects Models. R package version 3.1-166. Available at: https://CRAN.R-project.org/package=nlme [Accessed 25th August 2025].

Pinheiro, J. C. & Bates, D. M. (2000) Theory and Computational Methods for Linear Mixed-Effects Models. In: *Mixed-effects models in S and S-PLUS.* New York: Springer.

Pons, T. L. & Poorter, H. (2014) The effect of irradiance on the carbon balance and tissue characteristics of five herbaceous species differing in shade-tolerance. *Front Plant Science,* 5**,** 12. 10.3389/fpls.2014.00012.

Poorter, H., Fiorani, F., Pieruschka, R., Wojciechowski, T., Van Der Putten, W. H., Kleyer, M., Schurr, U. & Postma, J. (2016) Pampered inside, pestered outside? Differences and similarities between plants growing in controlled conditions and in the field. *New Phytologist,* 212(4)**,** 838-855. 10.1111/nph.14243.

Poorter, H., Niinemets, U., Ntagkas, N., Siebenkas, A., Maenpaa, M., Matsubara, S. & Pons, T. (2019) A meta-analysis of plant responses to light intensity for 70 traits ranging from molecules to whole plant performance. *New Phytol,* 223(3)**,** 1073-1105. 10.1111/nph.15754.

Poorter, H., Niklas, K. J., Reich, P. B., Oleksyn, J., Poot, P. & Mommer, L. (2012) Biomass allocation to leaves, stems and roots: meta-analyses of interspecific variation and environmental control. *New Phytol,* 193(1)**,** 30-50. 10.1111/j.1469-8137.2011.03952.x.

Posit Team (2024) *RStudio: Integrated Development Environment for R (Version 2024.09.0+375) [Computer software].* Boston, MA: Posit Software, PBC. Available at: http://www.posit.co/ [Accessed 15th August 2025].

R Core Team (2024) *R: A Language and Environment for Statistical Computing (Version 4.4.1) [Computer Software].* [Vienna, Austria: R Foundation for Statistical Computing. Available at: https://www.R-project.org/ [Accessed 09th October 2025].

Rashid, N., Zafar, M., Ahmad, M., Khan, M. A., Malik, K., Sultana, S. & Shah, S. N. (2018) Taxonomic significance of leaf epidermis in tribeTrifolieaeL. (Leguminosae; Papilionoideae) in Pakistan. *Plant Biosystems - An International Journal Dealing with all Aspects of Plant Biology,* 153(3)**,** 406-416. 10.1080/11263504.2018.1492995.

Ratzmann, G., Meinzer, F. C. & Tietjen, B. (2019) Iso/Anisohydry: Still a Useful Concept. *Trends in Plant Science,* 24(3)**,** 191-194. 10.1016/j.tplants.2019.01.001.

Reich, P. B. (2014) The world‐wide 'fast‐slow' plant economics spectrum: a traits manifesto. *Journal of Ecology,* 102(2)**,** 275-301. 10.1111/1365-2745.12211.

Resco De Dios, V. (2017) Circadian Regulation and Diurnal Variation in Gas Exchange. *Plant Physiology,* 175(1)**,** 3-4. 10.1104/pp.17.00984.

Sack, L. & Buckley, T. N. (2016) The Developmental Basis of Stomatal Density and Flux. *Plant Physiology,* 171(4)**,** 2358-63. 10.1104/pp.16.00476.

Sack, L. & Holbrook, N. M. (2006) Leaf hydraulics. *Annual Review of Plant Physiology and Plant Molecular Biology,* 57**,** 361-381. 10.1146/annurev.arplant.56.032604.144141.

Sack, L. & Scoffoni, C. (2012) Measurement of leaf hydraulic conductance and stomatal conductance and their responses to irradiance and dehydration using the Evaporative Flux Method (EFM). *Journal of Visualized Experiments*(70). 10.3791/4179.

Sack, L. & Scoffoni, C. (2013) Leaf venation: structure, function, development, evolution, ecology and applications in the past, present and future. *New Phytologist,* 198(4)**,** 983-1000. 10.1111/nph.12253.

Sakoda, K., Yamori, W., Shimada, T., Sugano, S. S., Hara-Nishimura, I. & Tanaka, Y. (2020) Higher Stomatal Density Improves Photosynthetic Induction and Biomass Production in Arabidopsis Under Fluctuating Light. *Front Plant Sci,* 11**,** 589603. 10.3389/fpls.2020.589603.

Samantara, K., Ivandi, E., Tulva, I., Jalakas, P., Khalegh Doust, B., Ingver, A., Karp, M., Brazauskas, G., Bleidere, M., Tamm, I., Horak, H. & Merilo, E. (2025) Higher adaxial stomatal density is associated with lower grain yield in spring wheat. *New Phytol,* 248(2)**,** 454-460. 10.1111/nph.70416.

Sassenrath-Cole, G. F. & Pearcy, R. W. (1994) Regulation of photosynthetic induction state by the magnitude and duration of low light exposure. *Plant Physiology,* 105(4)**,** 1115-1123.

Schielzeth, H., Dingemanse, N. J., Nakagawa, S., Westneat, D. F., Allegue, H., Teplitsky, C., Réale, D., Dochtermann, N. A., Garamszegi, L. Z. & Araya-Ajoy, Y. G. (2020) Robustness of linear mixed-effects models to violations of distributional assumptions. *Methods in Ecology and Evolution,* 11(9)**,** 1141-1152. 10.1111/2041-210X.13434.

Schneider, C. A., Rasband, W. S. & Eliceiri, K. W. (2012) NIH Image to ImageJ: 25 years of image analysis. *Nature Methods,* 9(7)**,** 671-675.

Sekiyama, T. & Nagashima, A. (2019) Solar Sharing for Both Food and Clean Energy Production: Performance of Agrivoltaic Systems for Corn, A Typical Shade-Intolerant Crop. *Environments,* 6(6). 10.3390/environments6060065.

Sellaro, R., Pacin, M. & Casal, J. J. (2012) Diurnal dependence of growth responses to shade in Arabidopsis: role of hormone, clock, and light signaling. *Molecular Plant,* 5(3)**,** 619-28. 10.1093/mp/ssr122.

Shapiro, S. S. & Wilk, M. B. (1965) An analysis of variance test for normality (complete samples). *Biometrika,* 52**,** 591-611.

Siefert, A., Violle, C., Chalmandrier, L., Albert, C. H., Taudiere, A., Fajardo, A., Aarssen, L. W., Baraloto, C., Carlucci, M. B., Cianciaruso, M. V., De, L. D. V., De Bello, F., Duarte, L. D., Fonseca, C. R., Freschet, G. T., Gaucherand, S., Gross, N., Hikosaka, K., Jackson, B., Jung, V., Kamiyama, C., Katabuchi, M., Kembel, S. W., Kichenin, E., Kraft, N. J., Lagerstrom, A., Bagousse-Pinguet, Y. L., Li, Y., Mason, N., Messier, J., Nakashizuka, T., Overton, J. M., Peltzer, D. A., Perez-Ramos, I. M., Pillar, V. D., Prentice, H. C., Richardson, S., Sasaki, T., Schamp, B. S., Schob, C., Shipley, B., Sundqvist, M., Sykes, M. T., Vandewalle, M. & Wardle, D. A. (2015) A global meta-analysis of the relative extent of intraspecific trait variation in plant communities. *Ecol Lett,* 18(12)**,** 1406-19. 10.1111/ele.12508.

Soleh, M. A., Tanaka, Y., Kim, S. Y., Huber, S. C., Sakoda, K. & Shiraiwa, T. (2017) Identification of large variation in the photosynthetic induction response among 37 soybean [Glycine max (L.) Merr.] genotypes that is not correlated with steady-state photosynthetic capacity. *Photosynth Res,* 131(3)**,** 305-315. 10.1007/s11120-016-0323-1.

Soleh, M. A., Tanaka, Y., Nomoto, Y., Iwahashi, Y., Nakashima, K., Fukuda, Y., Long, S. P. & Shiraiwa, T. (2016) Factors underlying genotypic differences in the induction of photosynthesis in soybean [Glycine max (L.) Merr.]. *Plant Cell & Environment,* 39(3)**,** 685-693. 10.1111/pce.12674.

Sperry, J. S. (2000) Hydraulic constraints on plant gas exchange. *Agricultural and Forest Meteorology,* 104(1)**,** 13-23. 10.1016/S0168-1923.

Stearns, S. C. (1989) The Evolutionary Significance of Phenotypic Plasticity. *BioScience,* 39(7)**,** 436-445. 10.2307/1311135.

Sturchio, M. A., Kannenberg, S. A. & Knapp, A. K. (2024a) Agrivoltaic arrays can maintain semi-arid grassland productivity and extend the seasonality of forage quality. *Applied Energy,* 356**,** 122418. 10.1016/j.apenergy.2023.122418.

Sturchio, M. A., Kannenberg, S. A., Pinkowitz, T. A. & Knapp, A. K. (2024b) Solar arrays create novel environments that uniquely alter plant responses. *Plants, People, Planet,* 6(6)**,** 1522-1533. 10.1002/ppp3.10554.

Sturchio, M. A. & Knapp, A. K. (2023) Ecovoltaic principles for a more sustainable, ecologically informed solar energy future. *Nature, Ecology & Evolution,* 7(11)**,** 1746-1749. 10.1038/s41559-023-02174-x.

Sturchio, M. A., Macknick, J. E., Barron-Gafford, G. A., Chen, A., Alderfer, C., Condon, K., Hajek, O. L., Miller, B., Pauletto, B., Siggers, J. A., Slette, I. J. & Knapp, A. K. (2022) Grassland Productivity Responds Unexpectedly To Dynamic Light and Soil Water Environments Induced by Photovoltaic Arrays. *Ecosphere,* 13(12)**,** e4334. 10.1002/ecs2.4334.

Suwannarut, W., Vialet-Chabrand, S. & Kaiser, E. (2023) Diurnal decline in photosynthesis and stomatal conductance in several tropical species. *Frontiers in Plant Science,* 14**,** 1273802. 10.3389/fpls.2023.1273802.

Tanaka, Y., Adachi, S. & Yamori, W. (2019) Natural genetic variation of the photosynthetic induction response to fluctuating light environment. *Current Opinion in Plant Biology,* 49**,** 52-59. 10.1016/j.pbi.2019.04.010.

Taylor, S. H. (2024) Unpublished data from bifacial agrivoltaic shade trial. Lancaster, UK: Lancaster University.

Taylor, S. H. & Long, S. P. (2017) Slow induction of photosynthesis on shade to sun transitions in wheat may cost at least 21% of productivity. *Philosophical Transactions of the Royal Society B,* 372(1730). 10.1098/rstb.2016.0543.

Taylor, S. H., Orr, D. J., Carmo-Silva, E. & Long, S. P. (2020) During photosynthetic induction, biochemical and stomatal limitations differ between Brassica crops. *Plant, Cell & Environment,* 43(11)**,** 2623-2636. 10.1111/pce.13862.

Thieurmel, B. & Elmarhraoui, A. (2019) *suncalc: Compute Sun Position, Sunlight Phases, Moon Position and Lunar Phase*. Available at: https://cran.r-project.org/web/packages/suncalc/index.html [Accessed 08th October 2025].

Tomimatsu, H. & Tang, Y. (2012) Elevated CO2 differentially affects photosynthetic induction response in two Populus species with different stomatal behavior. *Oecologia,* 169(4)**,** 869-78. 10.1007/s00442-012-2256-5.

Valladares, F., Gianoli, E. & Gómez, J. M. (2007) Ecological limits to plant phenotypic plasticity. *New Phytologist,* 176(4)**,** 749-763. 10.1111/j.1469-8137.2007.02275.x.

Valladares, F. & Niinemets, Ü. (2008) Shade tolerance, a key plant feature of complex nature and consequences. *Annual Review of Ecology, Evolution, and Systematics,* 39**,** 237-257. 10.1146/annurev.ecolsys.39.110707.173506.

Vialet-Chabrand, S. R. M., Matthews, J. S. A., Mcausland, L., Blatt, M. R., Griffiths, H. & Lawson, T. (2017) Temporal Dynamics of Stomatal Behavior: Modeling and Implications for Photosynthesis and Water Use. *Plant Physiology,* 174(2)**,** 603-613. 10.1104/pp.17.00125.

Vico, G., Manzoni, S., Palmroth, S. & Katul, G. (2011) Effects of stomatal delays on the economics of leaf gas exchange under intermittent light regimes. *New Phytologist,* 192(3)**,** 640-652. 10.1111/j.1469-8137.2011.03847.x.

Wall, S., Vialet-Chabrand, S., Davey, P., Van Rie, J., Galle, A., Cockram, J. & Lawson, T. (2022) Stomata on the abaxial and adaxial leaf surfaces contribute differently to leaf gas exchange and photosynthesis in wheat. *New Phytologist,* 235(5)**,** 1743-1756. 10.1111/nph.18257.

Way, D. A. & Pearcy, R. W. (2012) Sunflecks in trees and forests: from photosynthetic physiology to global change biology. *Tree Physiology,* 32(9)**,** 1066-1081. 10.1093/treephys/tps064.

Weselek, A., Bauerle, A., Hartung, J., Zikeli, S., Lewandowski, I. & Högy, P. (2021) Agrivoltaic system impacts on microclimate and yield of different crops within an organic crop rotation in a temperate climate. *Agronomy for Sustainable Development,* 41(5). 10.1007/s13593-021-00714-y.

Wickham, H., Averick, M., Bryan, J., Chang, W., D'agostino Mcgowan, L., Fracois, R., Grolemund, G., Hayes, A., Henry, L., Hester, J., Kuhn, M., Perderson Lin, T., Miller, E., Bache Milton, S., Muller, K., Ooms, J., Robinson, D., Seidel, D. P., Spinu, V., Takahashi, K., Vaughan, D., Wilke, C., Woo, K. & Yutani, H. (2019) Welcome to the tidyverse. *Journal of Open Source Software*, 4(43), 1686. Available at: https://joss.theoj.org/papers/10.21105/joss.01686 [Accessed 15th August 2025].

Wright, I. J., Reich, P. B., Westoby, M., Ackerly, D. D., Baruch, Z., Bongers, F., Cavender-Bares, J., Chapin, T., Cornelissen, J. H. C., Diemer, M., Flexas, J., Garnier, E. & Villar, R. (2004) The worldwide leaf economics spectrum. *Nature,* 428(6985)**,** 821–827. 10.1038/nature02403.

Xiong, D. & Nadal, M. (2020) Linking water relations and hydraulics with photosynthesis. *The Plant Journal,* 101(4)**,** 800-815. 10.1111/tpj.14595.

Xiong, Z., Xiong, D., Cai, D., Wang, W., Cui, K., Peng, S. & Huang, J. (2022) Effect of stomatal morphology on leaf photosynthetic induction under fluctuating light across diploid and tetraploid rice. *Environmental and Experimental Botany,* 194. 10.1016/j.envexpbot.2021.104757.

Yiotis, C., Mcelwain, J. C. & Osborne, B. A. (2021) Enhancing the productivity of ryegrass at elevated CO2 is dependent on tillering and leaf area development rather than leaf-level photosynthesis. *J Exp Bot,* 72(5)**,** 1962-1977. 10.1093/jxb/eraa584.

Zhang, N., Berman, S. R., Joubert, D., Vialet-Chabrand, S., Marcelis, L. F. M. & Kaiser, E. (2022) Variation of Photosynthetic Induction in Major Horticultural Crops Is Mostly Driven by Differences in Stomatal Traits. *Front Plant Sci,* 13**,** 860229. 10.3389/fpls.2022.860229.

Zhu, X. G., Ort, D. R., Whitmarsh, J. & Long, S. P. (2004) The slow reversibility of photosystem II thermal energy dissipation on transfer from high to low light may cause large losses in carbon gain by crop canopies: a theoretical analysis. *J Exp Bot,* 55(400)**,** 1167-75. 10.1093/jxb/erh141.

Zuur, A. F., Leno, E. N., Walker, N. J., Saveliev, A. A. & Smith, G. M. (2009) *Mixed Effects Models and Extensions in Ecology with R.* New York: Springer.

10 Supplementary Results

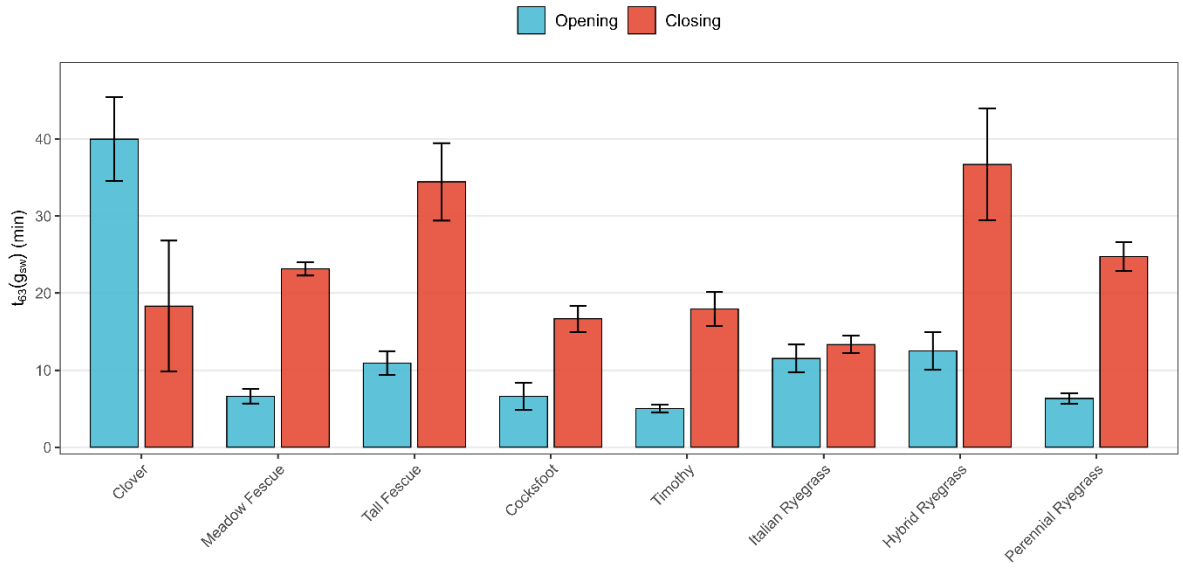

Figure S1. Side-by-side comparison of mean stomatal opening and closing time constants (t_{63}) on induction and de-induction for eight forage species. Bars represent mean +/- standard error.

Table S1. Model comparison of heterogeneous versus homogeneous variance structures for microclimate variables. Models were fitted using linear mixed-effects models with treatment as a fixed effect and date as a random intercept (1|date). Heterogeneous variance models allowed treatment-specific variances using the varIdent structure in nlme. ΔAIC is calculated as AIC(heterogeneous) - AIC(homogeneous); negative values indicate better fit for the heterogeneous variance model. Despite substantially better AIC fit for heterogeneous variance structures (ΔAIC ranging from -21 to -197), homogeneous variance models were selected for final analyses to ensure comparable standard errors across treatments for multiple comparison procedures and to avoid inflated standard errors that can produce misleading compact letter displays in post-hoc comparisons

Variable	Hetero AIC	Homog AIC	ΔAIC
PAR Morning	1775.98	1972.84	−196.86
T Morning	411.45	516.71	−105.26
T Afternoon	392.76	426.44	−33.69
RH Afternoon	744.30	765.99	−21.69
VPD Morning	−170.13	−43.99	−126.14
VPD Afternoon	−164.01	−94.07	−69.94
DLI window Morning	704.39	901.16	−196.77
Mean PAR	1719.91	1828.85	−108.94
Mean T	325.51	374.47	−48.96
Mean RH	707.72	748.69	−40.98
Mean VPD	−256.29	−203.75	−52.54
DLI	861.59	967.93	−106.34

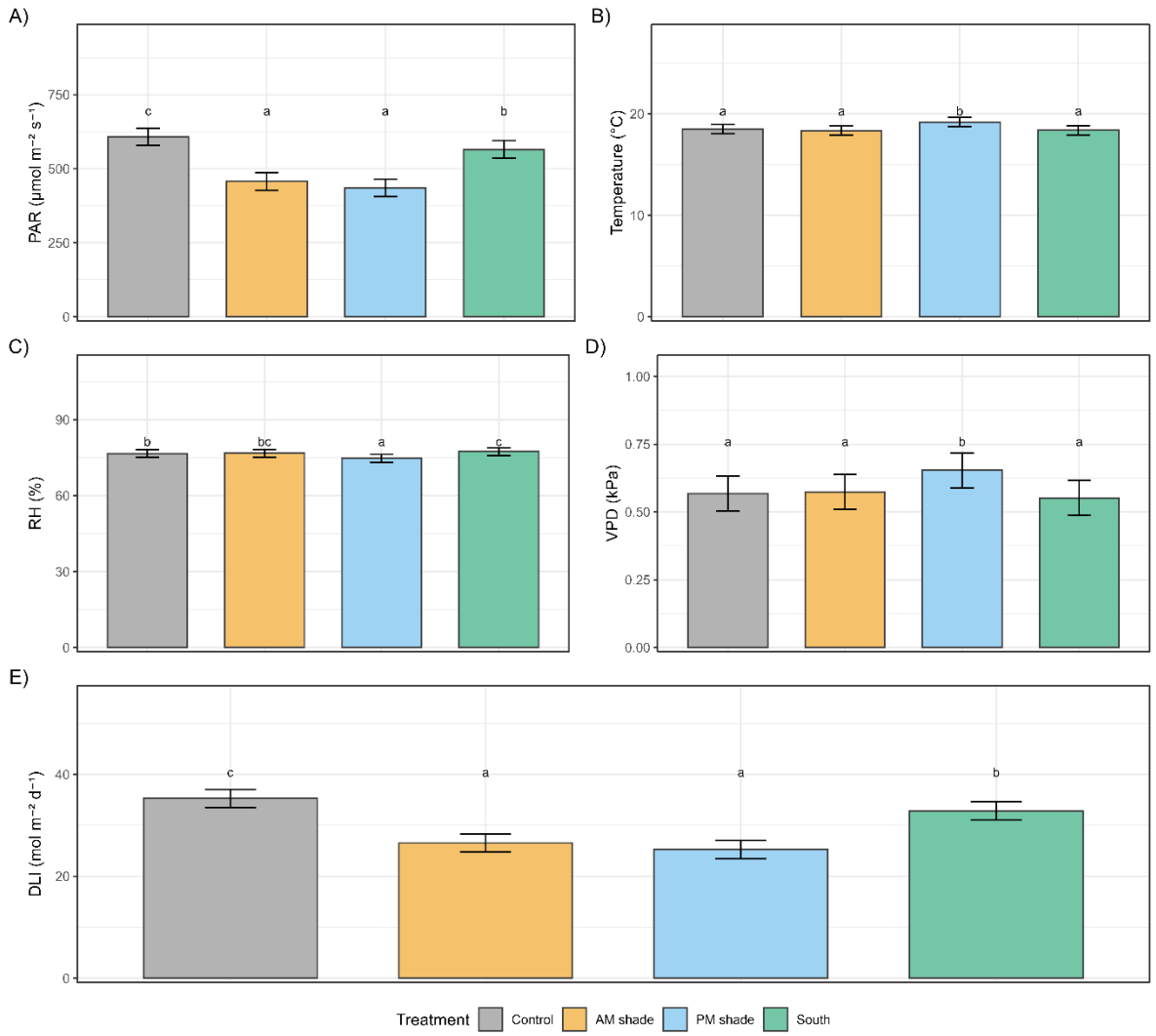

Figure S2. Full photoperiod microclimatic conditions across treatments during a 39-day shade experiment at Hazelrigg Experimental Station, Lancaster, UK. Mean values ± SE for (A) photosynthetically active radiation (PAR), (B) air temperature, (C) relative humidity (RH), and (D) vapour pressure deficit (VPD), aggregated over the entire photoperiod (sunrise to sunset). (E) Daily light integral (DLI) representing total photosynthetically active photon flux received per day (n = 39 days). Bar colours denote treatments (grey = Control, orange = AM shade, blue = PM shade, green = South reference). Compact letter displays above bars summarise Šidák-adjusted comparisons of estimated marginal means between treatments; treatments sharing the same letter were not significantly different ($p > 0.05$). All treatment effects were highly significant ($p < 0.001$). These full-day aggregations complement the time-window-specific analyses (morning and afternoon) presented in the main text (Figure 15) and demonstrate that shade structures substantially modified microclimate conditions throughout the photoperiod.

Field experiment - Multivariate Phenotypic Analysis of Grass Species

A principal component analysis (PCA) on eight traits for the three grass species confirmed the data's suitability for analysis (KMO = 0.715, Bartlett's $p < 0.001$). The first two PCs accounted for 90.40% of the total variance (PC1: 68.04%, PC2: 22.36%). PC1 represented a size and stomatal morphology gradient (high loadings: adaxial GCL, leaf biomass, g_{max} proxy), while PC2 represented a leaf economics gradient (positive: leaf area; negative: LMA, NSD). Under control conditions, species occupied distinct positions: Italian ryegrass (IRG) high on PC1, Perennial ryegrass (PRG) low on PC2, and Timothy intermediate (Figure S2). Analysis of multivariate dispersion (PERMDISP) indicated greater within-species variation in IRG compared to Timothy ($p < 0.001$) and PRG ($p < 0.05$), but no difference in dispersion among treatments ($p > 0.05$).

A PERMANOVA revealed significant main effects of species ($F_{2,45} = 378.42$, $R^2 = 0.853$, $p < 0.001$) and treatment ($F_{2,45} = 23.19$, $R^2 = 0.052$, $p < 0.001$), and a significant species × treatment interaction ($F_{4,45} = 9.83$, $R^2 = 0.044$, $p < 0.001$).

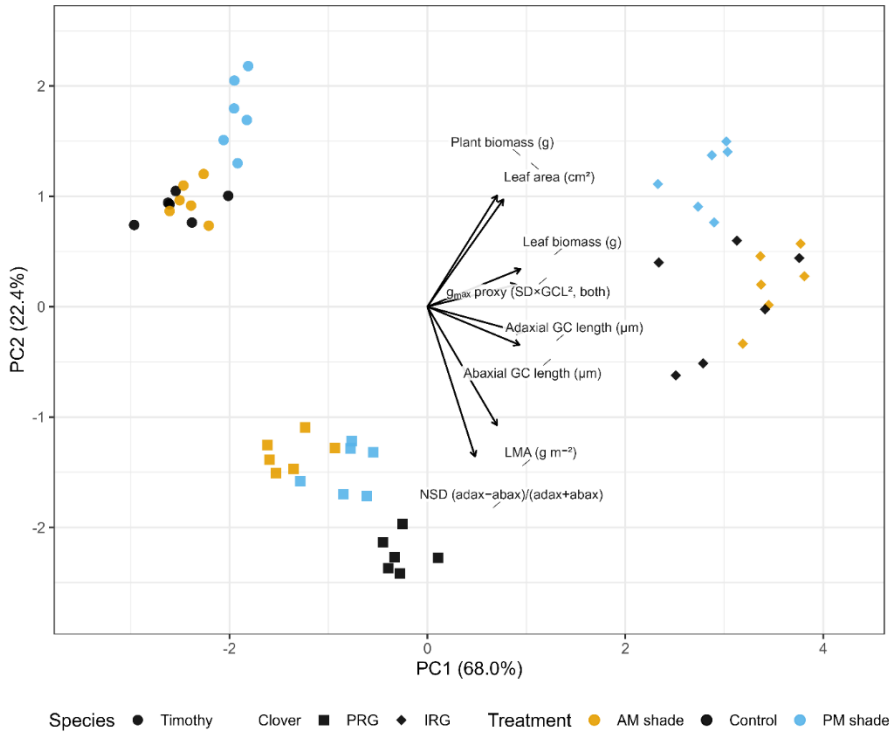

Figure S3. Multivariate principal component analysis (PCA) of three grass species under diurnal shading regimes during a 39-day field experiment. Biplot of the first two principal components (PC1 = 68.04%, PC2 = 22.36%) derived from eight standardised plant traits: leaf area (cm^2), leaf biomass (g), plant biomass (g), LMA ($g\ m^{-2}$), NSD, gmax proxy, adaxial guard cell length (µm), abaxial guard cell length (µm). Points represent individual plants (n = 54). Species are distinguished by shape (circle = Timothy, square = Perennial ryegrass, diamond = Italian ryegrass), while treatments are indicated by colour (black = Control, blue = PM shade, orange = AM shade). Vectors show trait loadings, with arrow length and direction proportional to the correlation strength of each trait with the principal components.

Centroid displacement analysis showed species-specific plasticity (Figure S3). PRG shifted significantly under both AM (d = 1.434, $p < 0.01$) and PM shade (d = 0.940, $p < 0.01$). In contrast, IRG and Timothy shifted significantly only under PM shade (IRG: d = 1.143; Timothy: d = 1.041; both $p < 0.01$), but not under AM shade ($p > 0.05$).

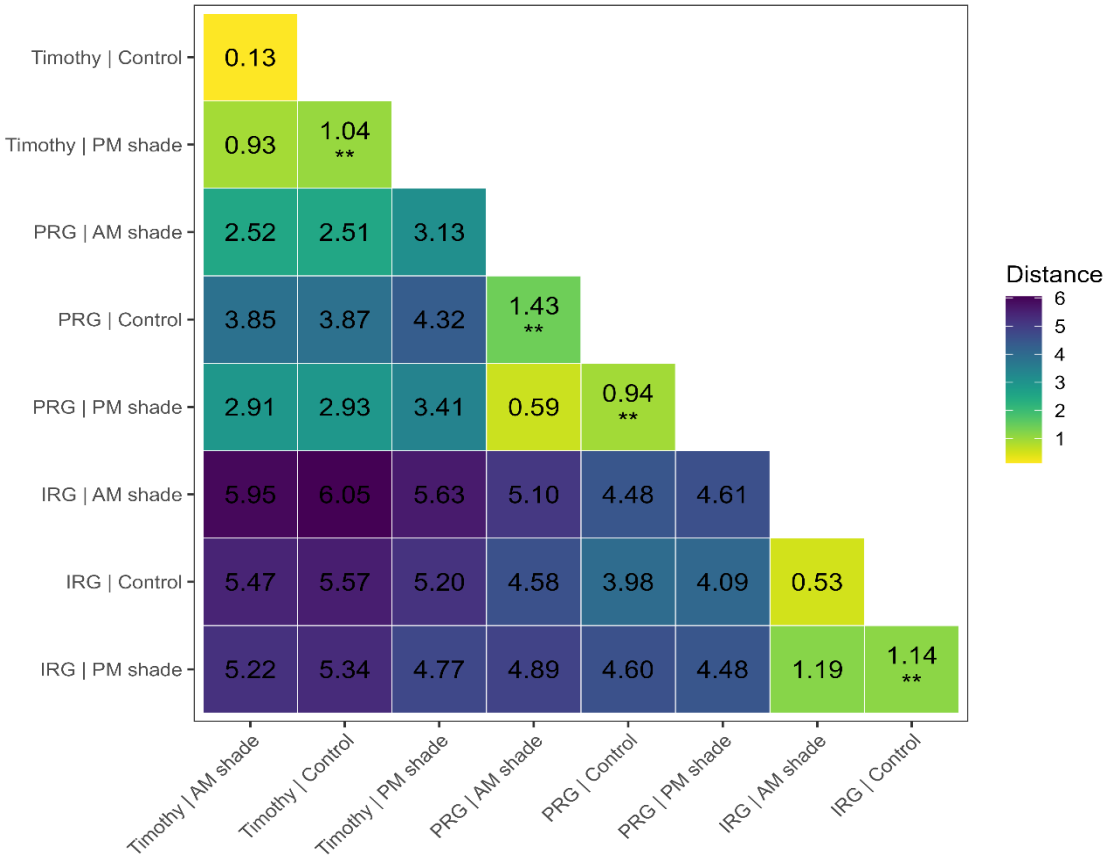

Figure S4. Heatmap of Euclidean distances between species × treatment centroids in the grass-only PCA space. Calculated from PC1 and PC2 scores. Distances quantify multivariate separation of treatment means; significant centroid shifts from control treatment, tested using permutation tests with Benjamini-Hochberg FDR adjustment, are indicated by an asterisk (** $p < 0.01$). Colour gradient denotes centroid distance (lighter yellow = smaller functional differences, darker purple = larger differences). The analysis shows Perennial ryegrass shifted under both shade treatments, while Italian ryegrass and Timothy responded significantly only to PM shade.

Table S2. Kinetic bottleneck analysis comparing stomatal opening time ($\uparrow t_{63}(g_{sw})$) and biochemical induction time ($\uparrow t_{90}(A)$) across species. The difference column (Stomatal − Biochem) indicates which process completes first; negative values indicate stomata finish before biochemistry, identifying Rubisco activation as the bottleneck. Values are mean ± SE (n = 5–6).

Species	$\uparrow t_{63}(g_{sw})$ (min)	$\uparrow t_{90}(A)$ (min)	Difference (min)	Bottleneck
Timothy	5.0 ± 0.5	7.3 ± 0.4	−2.3	Biochemical
Cocksfoot	6.6 ± 1.8	6.5 ± 0.6	+0.1	Balanced
PRG	6.3 ± 0.7	6.0 ± 0.2	+0.3	Balanced
Meadow fescue	6.6 ± 0.9	6.9 ± 0.5	−0.3	Balanced
Tall fescue	10.9 ± 1.6	8.9 ± 0.7	+2.0	Stomatal
IRG	11.5 ± 1.8	4.9 ± 0.4	+6.6	Stomatal
Hybrid RG	12.5 ± 2.5	6.2 ± 0.9	+6.3	Stomatal
Clover	40.0 ± 5.4	11.4 ± 0.7	+28.6	Stomatal